The neural basis of brain-body communication

Thesis by

Tongtong Wang

In Partial Fulfillment of the Requirements for the degree of

Doctor of Philosophy

CALIFORNIA INSTITUTE OF TECHNOLOGY

Pasadena, California

2026

(Defended March 12th, 2026)

Tongtong Wang
ORCID: 0000-0002-0408-2571

ACKNOWLEDGEMENTS

This thesis reflects not only scientific inquiry, but also years of mentorship, collaboration, friendship, and personal growth. When I began graduate school, I had passion and confidence – perhaps only those. Over time, I learned that pursuing a PhD requires far more: resilience, humility and patience. I have been fortunate to be surrounded by people who guided and supported me throughout this journey and ultimately made it possible.

First and foremost, I thank my advisor, Yuki Oka, for his guidance, scientific rigor, and trust. Yuki fostered an environment that encouraged independence while upholding high scientific standards. His ability to frame fundamental biological questions and pursue them with precision has profoundly shaped the way I think about research. His enthusiasm for science is infectious, and his vision continues to inspire me. As a leader, he appreciates the broad landscape of science with unique wisdom, and he saw potential beyond my early naivety. He consistently set high expectations, challenging me to grow beyond what I initially believed possible. I am especially grateful for the freedom to explore ambitious ideas. Through this independence, I gained invaluable experience establishing new experimental platforms, building collaborations, writing grants, reviewing manuscripts, and mentoring junior lab members besides leading scientific projects. I could not have asked for a more formative and productive graduate school experience for scientific career development.

Early in my graduate journey, I was extremely fortunate to have Allan-Hermann Pool and Takako Ichiki as my mentors. Allan was the first to show me what thoughtful mentorship means. His patience, generosity, and scientific rigor left a lasting imprint on me. He demonstrated that intellectual excellence and kindness can – and should – coexist. I hope to carry forward the mentorship spirit he exemplifies. Takako introduced me to the field of the peripheral nervous system, which became a central focus of this thesis. Her surgical mastery and meticulous experimental execution deeply impressed me. Equally inspiring is her intuitive understanding of physiological regulation. Both Allan and Takako played essential roles in my development as a scientist and continue to influence how I approach research.

I sincerely thank my thesis committee members for their thoughtful feedback and insightful questions. Professor Henry Lester provided both scientific guidance and generous support. His dedication to connecting the neuroscience community and supporting students spreads warmth throughout the campus. From him I learned the importance of accuracy in scientific language and communication. His appreciation for students continually encouraged me and broadened my perspective, and I hope to emulate his generosity in supporting future generations of scientists. Professor David Anderson's breadth and depth of understanding in neuroscience, as well as the clarity and rigor with which he communicates ideas, have been deeply inspiring. I admire his uncompromising scientific standards and logical precision. In him, I witnessed the sustained and unrelenting curiosity and passion. Professor Sarkis Mazmanian broadened my understanding of physiology beyond the nervous system, reminding me of the interaction of biological systems. Professor Long Cai's precision and quantitative mindset consistently challenged me to think more rigorously. I am grateful for the collective wisdom and encouragement they offered throughout this process.

I am profoundly thankful for my undergraduate training at Nankai University, which laid the foundation for everything that followed. The seeds planted there nearly a decade ago made this thesis possible. My undergraduate experience instilled in me both discipline and curiosity. I vividly remember the field trips during my freshman year, when we explored natural landscapes and developed an appreciation for biological diversity. Those memories shaped not only my scientific interests but also my worldview. Professors Zhengmao Zhu and Qingqiu Gong exemplified intellectual courage and youthful curiosity, encouraging exploration and openness to new experiences.

One of the greatest gifts I received at Caltech has been the friends whom I dearly cherish, learn from and collaborate with. Yameng Zhang has been a pillar of support during my years here. Her presence, kindness and encouragement made daily life brighter, and her companionship is what I will miss most. I am constantly inspired by her creativity, openness, and generosity. I have also been fortunate to work alongside talented colleagues and mentees in the Oka lab, including Bochuan Teng, Brittany Ho, Sangjun Lee, Vineet Augustine, Yuan

Zhao, Haruka Ebisu, Zhe Yang, Mari Oka, Elin Kang, Wongyo Jung, Ukjin Choi, Avedis Tufenkjian and Tara Gao. Working with each of you enriched both my science and life.

To my colleagues, thank you for the stimulating discussions and shared excitement about science. Caltech fosters a culture where close collaboration is natural and accessible. I am grateful to my collaborators – Richard Yao, Wei Gao, Jonathan Hoang, Viviana Gradinaru, Shichen Liu, Matt Thomson, Bei Zhang, Kirsten Frieda, Youstina Labib and Olujimi Ajijola – for their contribution to the published work included in this thesis.

I would like to acknowledge those whose contributions are less visible but essential to my work and life here. Tomomi Karigo, Xinhong Chen and Jineun Kim have always been responsive and generous. I am grateful as well to Yujing Yang, Brian Williams, Manxuan Zhou, Yi-Ting Cheng, Brian Williams, Jiahui Peng, Carlos Lois, Nicole Schweers, James Linton, Felix Horns, Michael Elowitz, Elisha Mackey, Michael Dickinson, Kathy Cheung, Amit Vinograd, Jieyu Zheng, Daniel Pollak, Karen Lencioni and the OLAR team. Administrative leaders Lauren Breeyear and Emma Schuyler played important roles in hosting social events and connecting the community. Serving as a student host during graduate recruitment gave me the opportunity to connect closely with junior cohorts.

To my best friends along the life – Jie Yan, Qiaochu Zhang and Shan Hu, thank you for your presence during both moments of doubt and moments of triumph. I am always amazed at how our friendship transcends distance and time. Even when years pass with minimal contact, meeting again feels as though time has stood still. That continuity is rare and precious. I am also deeply grateful to many friends who have supported me from afar, including Sheng Guo, Jiachun Xu, Henan Wei, Yuhui Wang, Lin Luan, Danqing Tong, Senhao Kou, Zixin Zhao.

Last but most importantly, my sincere gratitude to my parents - Yafei Wang and Hongbo Huang, and to Yijie Zhang, for showing me what love means. Their unconditional support has always been my greatest strength. They did everything to ensure my happiness and independent will. My parents have been my role models in embracing life and pursuing personal interests with courage and joy. For every major decision in my life, they share their

opinions but never try to influence my mind. Through their actions, they taught me openness, courage, and reverence for time and health. As I grow older, I have come to realize how rare and precious such support is. There are many times during this thesis I asked myself whether I was spending my life meaningfully. The answer lies in the values they taught me without words, to explore bravely, to live fully in the present, and to move forward without regret. Words are insufficient to express my gratitude.

This thesis is for all of you.

ABSTRACT

Understanding how the nervous system orchestrates physiology across the body has long been a central question in neuroscience. While neural mechanisms underlying behavior have been extensively characterized, the cellular and circuit principles that mediate brain-body communication remain underexplored. In this thesis, I investigate how internal physiological signals are detected and translated into coordinated regulation of organ functions through specialized sensory and autonomic pathways.

Using molecular, behavioral, and genetic perturbation approaches, I first examine how changes in body fluid balance are detected by central sensory neurons. I identify distinct neuronal populations within forebrain circumventricular regions that detect hyperosmotic and hypovolemic challenges and drive modality-specific fluid consumption behaviors. Then I show how water signals in the gut are encoded by a dedicated vagal afferent population, providing feed-forward inputs that contribute to thirst satiation. These studies demonstrate that internal states are monitored through specialized channels spanning central and peripheral circuits.

Next, I investigate the circuit logic of sympathetic regulation in the abdomen, identifying molecularly defined neuronal populations that project selectively to visceral organs and differentially regulate gastrointestinal transit and digestive processes. These results demonstrate that sympathetic outputs are organized into discrete pathways that enable precise and independent control of physiology. I then synthesize current knowledge of autonomic organization, highlighting its molecular diversity and modular architecture as key features enabling selective regulation of organ function.

Together, these findings reveal that brain-body communication is mediated by structured sensory pathways and modular autonomic circuits to achieve precise yet flexible control of physiology. This work provides a framework for understanding how neural systems coordinate internal stability and offers insight into how disruptions of these processes may contribute to diseases.

PUBLISHED CONTENT AND CONTRIBUTIONS

Wang, T., Teng, B., Yao, D. R., Gao, W., & Oka, Y. (2025). Organ-specific sympathetic innervation defines visceral functions. *Nature*, *637*(8047), 895–902. https://doi.org/10.1038/s41586-024-08269-0

T.W. conceived the research program, designed and carried out experiments, analyzed data, made figures, and wrote the manuscript.

Wang, T., Tufenkjian, A., Ajijola, O. A., & Oka, Y. (2025). Molecular and functional diversity of the autonomic nervous system. *Nature reviews. Neuroscience*, *26*(10), 607–622. https://doi.org/10.1038/s41583-025-00941-2

T.W. conceived the review outline, researched data, designed figures, and wrote the article.

Ichiki, T., **Wang, T.**, Kennedy, A., Pool, A. H., Ebisu, H., Anderson, D. J., & Oka, Y. (2022). Sensory representation and detection mechanisms of gut osmolality change. *Nature*, *602*(7897), 468–474. https://doi.org/10.1038/s41586-021-04359-5

T.W. participated in performing *in vivo* calcium imaging, data analysis and figure making.

Zhang, Y., Pool, A. H.#, **Wang, T.#**, Liu, L., Kang, E., Zhang, B., Ding, L., Frieda, K., Palmiter, R., & Oka, Y. (2023). Parallel neural pathways control sodium consumption and taste valence. *Cell*, *186*(26), 5751–5765.e16. https://doi.org/10.1016/j.cell.2023.10.020

T.W. performed spatial transcriptomics experiments as well as data analysis.

Wang, T., Pool, A. H., & Oka, Y. (2022). Serotonergic fast lane from taste detection to preparatory digestive actions. *Neuron*, *110*(6), 907–909. https://doi.org/10.1016/j.neuron.2022.02.023

T.W. designed figures and wrote the preview article.

Pool, A. H., **Wang, T.**, Stafford, D. A., Chance, R. K., Lee, S., Ngai, J., & Oka, Y. (2020). The cellular basis of distinct thirst modalities. *Nature*, 588(7836), 112–117. https://doi.org/10.1038/s41586-020-2821-8

T.W. participated in conceiving the research program, designing and carrying out experiments, analyzing data, making figures, and writing the manuscript.

Chen, X., Ravindra Kumar, S., Adams, C. D., Yang, D., **Wang, T.**, Wolfe, D. A., Arokiaraj, C. M., Ngo, V., Campos, L. J., Griffiths, J. A., Ichiki, T., Mazmanian, S. K., Osborne, P. B., Keast, J. R., Miller, C. T., Fox, A. S., Chiu, I. M., & Gradinaru, V. (2022). Engineered AAVs for non-invasive gene delivery to rodent and non-human primate nervous systems. *Neuron*, 110(14), 2242–2257.e6. https://doi.org/10.1016/j.neuron.2022.05.003

T.W. performed *in vivo* vagal neuron calcium imaging and analyzed data.

Ge, X., Wekselblatt, J. B., Elmore, S., Wang, B., **Wang, T.**, Dai, R., Zhang, T., Dave, H., Ghaderi, M., Anilkumar, A. R., Wang, B., Sirsi, S. R., Ahn, J. M., Shapiro, M. G., Oka, Y., Lois, C., & Qin, Z. (2025). In Vivo Cytosolic Delivery of Biomolecules into Neurons for Super-Resolution Imaging and Genome Modification. *Advanced science* (Weinheim, Baden-Wurttemberg, Germany), 12(25), e2501033. https://doi.org/10.1002/advs.202501033

T.W. participated in experiments.

Yang, Z., **Wang, T.**, & Oka, Y. (2021). Predicting changes in osmolality. *eLife*, 10, e74551. https://doi.org/10.7554/eLife.74551

T.W. designed figures.

TABLE OF CONTENTS

PROLOGUE

A central question motivating my work is how the nervous system orchestrates physiology across the body to meet both internal needs and external demands. Organisms continuously integrate information about the environment, such as resource availability or threat, with signals reflecting internal conditions including hydration and metabolic status, and translate these inputs into coordinated adjustments of behavior and organ function. While substantial progress has been made in understanding neural circuits underlying action, mechanistic insights into how the brain regulates physiological processes have lagged behind, in part because quantifying organ function *in vivo* has been technically challenging. As a result, the principles by which the brain communicates with peripheral organs remain underexplored.

This thesis approaches brain-body communication from the perspective that physiological regulation arises from the activity of defined neural populations organized into structured pathways. By examining how internal signals are detected, how information flows through neuronal circuits, and how descending pathways causally modulate organ function, this work seeks to uncover how coordinated physiological responses emerge from cellular- and circuit-level mechanisms.

Together, the studies presented here advance the view that physiological regulation is an emergent property from structured neural networks that coordinate the body as an integrated system. By establishing a circuit-level framework for brain-body axis, this work clarifies how neural activity supports stability in changing environments and offers insight into how disruptions of these mechanisms may lead to disease.

Chapter 1

INTRODUCTION

SUMMARY

This chapter frames brain-body communication as a central problem in systems neuroscience by contrasting advances in linking molecularly defined neural activity to behavior with the limited understanding of how neural circuits regulate physiology. It examines how physiological regulation is organized through specialized sensory pathways that monitor internal states and through autonomic circuits that coordinate selective control across organ systems. By outlining the anatomical and conceptual context of these processes, this chapter establishes the foundation for the themes explored in the following chapters.

LINKING NEURAL CIRCUITS TO PHYSIOLOGICAL REGULATION

The nervous system has been primarily analyzed through the study of perception and action, focusing on how external stimuli are transformed into decisions, movements, and learned behaviors[1–4]. Equally fundamental, yet much less explored, is the role of neural circuits in regulating body physiology[5,6]. Whether confronting a threat or anticipating a feast, organisms coordinate cardiovascular tone[7,8], energy and fluid balance[9,10], endocrine signaling[11], and immune activity[12–14] in response to both external circumstances and internal demands. Physiological regulation is not simply a corrective process restoring equilibrium after perturbation[15,16]. In many cases, neural systems initiate anticipatory adjustments before measurable deviations occur in the internal milieu, enabling rapid adaptation[17–19]. The central objective of this thesis is to understand how neural systems implement such regulatory control of bodily function at the cellular and circuit level.

Over the past several decades, studies in systems neuroscience have achieved substantial progress in linking brain neuron type to behavior[20–23]. Advances in neural activity recording and genetic perturbation tools have enabled precise quantification of actions and alignment of behavioral events with neural dynamics at millisecond resolution[24,25], allowing causal relationships between molecularly defined neuronal populations and behavioral outputs to be established. In contrast, mechanistic understanding of how neural circuits regulate physiological processes remains comparatively limited.

Behavioral outputs can be quantified as discrete events with defined temporal and categorical structures[26]. Physiological variables, in contrast, evolve continuously across multiple organ systems[27–30], including cardiovascular regulation, metabolic control, gastrointestinal function, and immune responses. These processes are governed by interacting feedback loops that operate over diverse timescales[5]. Changes in physiological variables frequently occur without overt behavioral differences, and their functional significance depends strongly on context. A given shift in blood pressure, gastrointestinal motility, or hormone release may be adaptive under one physiological state and maladaptive under another.

The continuous and distributed nature of physiological regulation complicates efforts to establish direct relationships between neural activity and organismal outcomes. Physiological measurements are typically confined to individual organs or specific pharmacological signaling[31,32], providing limited insight into how neural circuits coordinate integrated physiological states. Moreover, physiological readouts are rarely causally mapped to defined neuronal subpopulations or temporally aligned with neural dynamics in vivo[33,34], restricting the ability to draw causal inferences. As a result, the organizational principles through which neural circuits communicate with peripheral organs remain largely undefined.

This disparity reflects a broader gap between behavioral neuroscience and the study of physiological regulation. While neural mechanisms underlying decision-making and action have been dissected with increasing precision, the neural circuits coordinate organ function across the body remain underexplored. Bridging this gap requires conceptual and experimental frameworks that integrate cell-type-resolved analysis with quantitative measurements of physiological processes.

Brain-body communication encompasses both the sensing of internal conditions and the regulation of physiological processes through descending pathways. These processes operate across multiple spatial and temporal scales, from rapid synaptic signaling to slower hormonal and metabolic adjustments. Elucidating how neural systems coordinate these layers with cellular and circuit resolution is essential for understanding how organisms maintain stability while adapting to dynamic environments.

NEURAL MECHANISMS OF INTEROCEPTION

Physiological regulation centers on variables that are maintained within constrained ranges, including such as the level of blood osmolality and glucose, blood pressure, and core body temperature[35]. These variables reflect coordinated activity across multiple organ systems and

evolve continuously over time. Unlike external sensory inputs, which originate from discrete environmental stimuli, internal signals arise from distributed physiological processes and encode the collective state of the organism.

A useful entry point is the regulation of internal variables that must be tightly controlled to sustain cellular and organ function. Body fluid balance provides an informative example. The balance between water and solutes in the circulation[36,37], commonly measured as osmolality, is maintained within a narrow range. Deviations rapidly compromise cardiovascular stability and cellular function. However, even within this domain, distinct disturbances engage different regulatory strategies. Increases in blood osmolality induce osmotic thirst that drives consumption of water, whereas reductions in circulating volume produce hypovolemic thirst that motivates ingestion of both water and salts to restore blood volume[38]. These observations indicate that the nervous system distinguishes different internal states rather than responding to a generic signal of imbalance.

Similar principles extend beyond fluid balance. Feeding, thermoregulation and immune responses involve distributed neural pathways to sense and regulate internal variables. Coordination between behavior and physiology is a recurring theme. Drinking behavior interacts with mechanisms controlling renal function and vascular tone[39,40], while feeding behavior engages neural circuits that regulate nutrient metabolism and storage[41,42]. Immune challenges alter neural activity to influence sickness behavior and energy allocation[43–45]. These examples highlight the need to understand how neural systems represent internal conditions and guide both behavioral and physiological responses.

Monitoring internal variables (interoception) poses an anatomical challenge for brain neurons which are isolated from peripheral signals by the blood-brain barrier. Signals reflecting osmotic balance, tissue state, or mechanical stimuli are detected by specialized sensory interfaces that provide access to circulating factors and visceral conditions.

Circumventricular organs in the brain, including the subfornical organ and organum vasculosum of the lamina terminalis, possess fenestrated vasculature that permits detection

of changes in blood composition[46,47]. These structures have long been recognized as critical sites for sensing hydration status and circulating signals. However, the cellular mechanisms by which distinct physiological perturbations are encoded and translated into specific behavioral and autonomic responses remain incompletely resolved.

Sensory neurons in cranial and spinal ganglia provide complementary information on body physiology[35,48], by detecting interoceptive signals arising from peripheral organs and transmitting this information to central circuits. For instance, pre-absorptive signals from the oropharyngeal cavity and gastrointestinal tract influence appetite circuits before systemic changes occur[49,50], allowing rapid modulation of behavior. Liquid ingestion or changes in gastrointestinal osmolality inhibit forebrain thirst neurons, contributing to timely termination of drinking[51]. Yet the peripheral neural substrates for detecting these visceral signals, the anatomical sites of detection, and the circuit pathways through which these signals are transmitted to central processing remain unclear.

Together, central and peripheral sensing systems construct representations of internal state that guide both behavior and physiological regulation.

AUTONOMIC CONTROL OF ORGAN FUNCTIONS

Communication from the brain to peripheral organs is mediated through autonomic pathways comprising sympathetic and parasympathetic branches[6]. Historical descriptions emphasized opposing functional roles, associating sympathetic activity with increased cardiovascular output and energy mobilization, and parasympathetic activity with restorative processes such as digestion[52,53]. This framework provides a useful conceptual foundation but does not capture the cellular diversity and functional specialization that become increasingly characterized.

Autonomic motor pathways are organized through a two-relay manner in which preganglionic neurons in the central nervous system project to postganglionic neurons in peripheral ganglia, which then innervate target tissues[54–56]. Sympathetic ganglia are distributed along the vertebral column and provide widespread innervation of organs including the heart, lung, gastrointestinal tract, pancreas, liver, and spleen. Parasympathetic pathways regulate organ function through ganglia located close to target tissues.

Recent molecular and anatomical studies have identified diverse autonomic neuron populations defined by transcriptional profiles[57,58], neurotransmitter expression[59], and connectivity[60–63]. These findings suggest that autonomic regulation is implemented through multiple parallel circuits, allowing selective control rather than a uniform output.

Historically, autonomic control was conceptualized as broadly distributed, with neural activity producing generalized physiological effects[64,65]. Sympathetic and parasympathetic circuits were described as primarily noradrenergic and cholinergic, respectively[66]. Functional distinctions were inferred largely from receptor expression and organ-level responses[67,68]. Emerging evidence supports a more refined view in which autonomic regulation is organized through modular circuits with specialized roles. Specificity arise through selective projections of neuron populations to particular organs, differential recruitment of neuron subtypes under distinct conditions, and context-dependent modulation of circuit activity[6,69]. At the molecular level, combinations of neurotransmitters, neuropeptides, and receptor expression patterns shape how target tissues respond to neural input.

This framework has important implications for translational applications. Dysregulation may reflect perturbations within specific circuit modules, such as misrouting of signals to a target organ, inappropriate recruitment of a neuron subtype, or maladaptive plasticity in specific pathways[70–73], rather than global imbalance between sympathetic and parasympathetic tone. Identifying the circuit architecture underlying physiological control provides a foundation for interpreting how disruptions lead to pathological states and for developing targeted interventions.

THESIS OVERVIEW

This thesis investigates brain-body communication through the lens of cellular organization and circuit specificity. By combining molecular, anatomical, physiological and functional analyses, it examines how internal physiological signals are represented, how autonomic pathways are organized, and how defined neural populations regulate organ functions (**Thesis summary diagram**). The goal is to clarify the neural mechanisms for coordinating physiological processes across spatial and temporal scales.

Chapter II focuses on internal state detection in the context of body fluid balance, examining both central sensory neurons within the lamina terminalis and peripheral visceral afferent pathways. Chapter III examines sympathetic regulation of abdominal organs, testing how molecularly defined neuron populations project to visceral targets and causally modulate physiological processes. Chapter IV synthesizes current understanding of autonomic circuit architecture and diversity, discussing the future directions and challenges. Together, these chapters support a unified view: brain-body communication is implemented through structured sensory neurons and autonomic circuits, enabling precise yet flexible coordination of physiology across the organism.

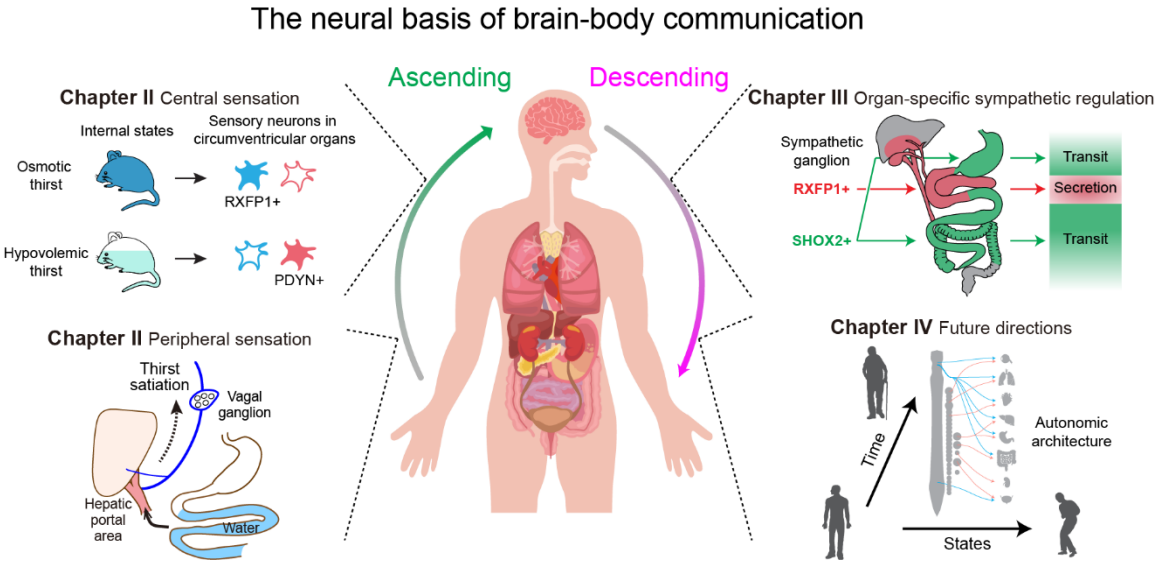

Thesis summary diagram

REFERENCES

1.Luo, L. Architectures of neuronal circuits. *Science* **373**, eabg7285 (2021).

2.Lu, J., Sherman, D., Devor, M. & Saper, C. B. A putative flip-flop switch for control of REM sleep. *Nature* **441**, 589–594 (2006).

3.Murugan, M. *et al.* Combined Social and Spatial Coding in a Descending Projection from the Prefrontal Cortex. *Cell* **171**, 1663-1677.e16 (2017).

4.Sternson, S. M. & Eiselt, A.-K. Three Pillars for the Neural Control of Appetite. *Annu Rev Physiol* **79**, 401–423 (2017).

5.Sammons, M. *et al.* Brain-body physiology: Local, reflex, and central communication. *Cell* **187**, 5877–5890 (2024).

6.Wang, T., Tufenkjian, A., Ajijola, O. A. & Oka, Y. Molecular and functional diversity of the autonomic nervous system. *Nat. Rev. Neurosci.* **26**, 607–622 (2025).

7.Guyenet, P. G. The sympathetic control of blood pressure. *Nat Rev Neurosci* **7**, 335–346 (2006).

8.Lovelace, J. W. *et al.* Vagal sensory neurons mediate the Bezold-Jarisch reflex and induce syncope. *Nature* **623**, 387–396 (2023).

9.Andermann, M. L. & Lowell, B. B. Toward a Wiring Diagram Understanding of Appetite Control. *Neuron* **95**, 757–778 (2017).

10.Augustine, V., Lee, S. & Oka, Y. Neural Control and Modulation of Thirst, Sodium Appetite, and Hunger. *Cell* **180**, 25–32 (2020).

11.Bany Bakar, R., Reimann, F. & Gribble, F. M. The intestine as an endocrine organ and the role of gut hormones in metabolic regulation. *Nat Rev Gastroenterol Hepatol* **20**, 784–796 (2023).

12.Udit, S., Blake, K. & Chiu, I. M. Somatosensory and autonomic neuronal regulation of the immune response. *Nat Rev Neurosci* **23**, 157–171 (2022).

13.Martinez-Sanchez, N. *et al.* The sympathetic nervous system in the 21st century: Neuroimmune interactions in metabolic homeostasis and obesity. *Neuron* **110**, 3597–3626 (2022).

14.Chan, K. L., Poller, W. C., Swirski, F. K. & Russo, S. J. Central regulation of stress-evoked peripheral immune responses. *Nat Rev Neurosci* **24**, 591–604 (2023).

15.Betley, J. N. *et al.* Neurons for hunger and thirst transmit a negative-valence teaching signal. *Nature* **521**, 180–185 (2015).

16.Stuber, G. D., Schwitzgebel, V. M. & Lüscher, C. The neurobiology of overeating. *Neuron* **113**, 1680–1693 (2025).

17.Gizowski, C., Zaelzer, C. & Bourque, C. W. Clock-driven vasopressin neurotransmission mediates anticipatory thirst prior to sleep. *Nature* **537**, 685–688 (2016).

18.Zimmerman, C. A. *et al.* Thirst neurons anticipate the homeostatic consequences of eating and drinking. *Nature* **537**, 680–684 (2016).

19.Tonosaki, K., Hori, Y., Shimizu, Y. & Tonosaki, K. Relationships between insulin release and taste. *Biomed Res* **28**, 79–83 (2007).

20.Aponte, Y., Atasoy, D. & Sternson, S. M. AGRP neurons are sufficient to orchestrate feeding behavior rapidly and without training. *Nat Neurosci* **14**, 351–355 (2011).

21.Xu, M. *et al.* Basal forebrain circuit for sleep-wake control. *Nat Neurosci* **18**, 1641–1647 (2015).

22.Luo, L., Callaway, E. M. & Svoboda, K. Genetic Dissection of Neural Circuits: A Decade of Progress. *Neuron* **98**, 256–281 (2018).

23.Kim, D.-W. *et al.* Multimodal Analysis of Cell Types in a Hypothalamic Node Controlling Social Behavior. *Cell* **179**, 713-728.e17 (2019).

24.Jennings, J. H. *et al.* Visualizing hypothalamic network dynamics for appetitive and consummatory behaviors. *Cell* **160**, 516–527 (2015).

25.Allen, W. E. *et al.* Thirst regulates motivated behavior through modulation of brainwide neural population dynamics. *Science* **364**, 253 (2019).

26.Nath, T. *et al.* Using DeepLabCut for 3D markerless pose estimation across species and behaviors. *Nat Protoc* **14**, 2152–2176 (2019).

27.Xiao, R. & Xu, X. Z. S. Temperature Sensation: From Molecular Thermosensors to Neural Circuits and Coding Principles. *Annu Rev Physiol* **83**, 205–230 (2021).

28.Zsombok, A., Desmoulins, L. D. & Derbenev, A. V. Sympathetic circuits regulating hepatic glucose metabolism: where we stand. *Physiol Rev* **104**, 85–101 (2024).

29.Mota, C. M. D. & Madden, C. J. Neural circuits of long-term thermoregulatory adaptations to cold temperatures and metabolic demands. *Nat Rev Neurosci* **25**, 143–158 (2024).

30.Mehta, N. H. *et al.* Quantifying cerebrospinal fluid dynamics: A review of human neuroimaging contributions to CSF physiology and neurodegenerative disease. *Neurobiology of Disease* **170**, 105776 (2022).

31.Kumari, R. *et al.* Sympathetic NPY controls glucose homeostasis, cold tolerance, and cardiovascular functions in mice. *Cell Rep* **43**, 113674 (2024).

32.Neri, D. *et al.* Distinct sympathetic projections to brown fat regulate thermogenesis and glucose tolerance. *Nat Metab* https://doi.org/10.1038/s42255-025-01429-0 (2026) doi:10.1038/s42255-025-01429-0.

33.Zhu, Y. *et al.* Sympathetic neuropeptide Y protects from obesity by sustaining thermogenic fat. *Nature* **634**, 243–250 (2024).

34.Li, E. *et al.* Control of lipolysis by a population of oxytocinergic sympathetic neurons. *Nature* **625**, 175–180 (2024).

35.Prescott, S. L. & Liberles, S. D. Internal senses of the vagus nerve. *Neuron* **110**, 579–599 (2022).

36.McKinley, M. J. & Johnson, A. K. The physiological regulation of thirst and fluid intake. *News Physiol Sci* **19**, 1–6 (2004).

37.Leib, D. E., Zimmerman, C. A. & Knight, Z. A. Thirst. *Curr Biol* **26**, R1260–R1265 (2016).

38.Oatley, K. Changes of Blood Volume and Osmotic Pressure in the Production of Thirst. *Nature* **202**, 1341–1342 (1964).

39.DiBona, G. F. Neural control of the kidney: functionally specific renal sympathetic nerve fibers. *Am J Physiol Regul Integr Comp Physiol* **279**, R1517-1524 (2000).

40.Zimmerman, C. A. *et al.* A gut-to-brain signal of fluid osmolarity controls thirst satiation. *Nature* **568**, 98–102 (2019).

41.Bai, L. *et al.* Genetic Identification of Vagal Sensory Neurons That Control Feeding. *Cell* **179**, 1129-1143.e23 (2019).

42.Lal, N. K. *et al.* Xiphoid nucleus of the midline thalamus controls cold-induced food seeking. *Nature* **621**, 138–145 (2023).

43.Evans, S. S., Repasky, E. A. & Fisher, D. T. Fever and the thermal regulation of immunity: the immune system feels the heat. *Nat Rev Immunol* **15**, 335–349 (2015).

44.Klein Wolterink, R. G. J., Wu, G. S., Chiu, I. M. & Veiga-Fernandes, H. Neuroimmune Interactions in Peripheral Organs. *Annu Rev Neurosci* **45**, 339–360 (2022).

45.Jin, H., Li, M., Jeong, E., Castro-Martinez, F. & Zuker, C. S. A body-brain circuit that regulates body inflammatory responses. *Nature* **630**, 695–703 (2024).

46.Johnson, A. K. & Gross, P. M. Sensory circumventricular organs and brain homeostatic pathways. *FASEB J* **7**, 678–686 (1993).

47.Bourque, C. W. Central mechanisms of osmosensation and systemic osmoregulation. *Nat Rev Neurosci* **9**, 519–531 (2008).

48.Lechner, S. G. *et al.* The molecular and cellular identity of peripheral osmoreceptors. *Neuron* **69**, 332–344 (2011).

49.Williams, E. K. *et al.* Sensory Neurons that Detect Stretch and Nutrients in the Digestive System. *Cell* **166**, 209–221 (2016).

50.Kim, D.-Y. *et al.* A neural circuit mechanism for mechanosensory feedback control of ingestion. *Nature* **580**, 376–380 (2020).

51.Augustine, V. *et al.* Temporally and Spatially Distinct Thirst Satiation Signals. *Neuron* **103**, 242-249.e4 (2019).

52.Langley, J. N. *The Autonomic Nervous System*. (W. Heffer, 1921).

53.Gibbins, I. Functional organization of autonomic neural pathways. *Organogenesis* **9**, 169–175 (2013).

54.Langley, J. N. On the Regeneration of Pre-Ganglionic and of Post-Ganglionic Visceral Nerve Fibres. *The Journal of Physiology* **22**, 215–230 (1897).

55.Deuchars, S. A. & Lall, V. K. Sympathetic preganglionic neurons: properties and inputs. *Compr Physiol* **5**, 829–869 (2015).

56.Gibbons, C. H. Basics of autonomic nervous system function. *Handb Clin Neurol* **160**, 407–418 (2019).

57.Mapps, A. A. *et al.* Diversity of satellite glia in sympathetic and sensory ganglia. *Cell Rep* **38**, 110328 (2022).

58.Wang, T., Teng, B., Yao, D. R., Gao, W. & Oka, Y. Organ-specific sympathetic innervation defines visceral functions. *Nature* **637**, 895–902 (2025).

59.Sharma, S. *et al.* Tiered sympathetic control of cardiac function revealed by viral tracing and single cell transcriptome profiling. *Elife* **12**, e86295 (2023).

60.Tao, J. *et al.* Highly selective brain-to-gut communication via genetically defined vagus neurons. *Neuron* **109**, 2106-2115.e4 (2021).

61.Veerakumar, A., Yung, A. R., Liu, Y. & Krasnow, M. A. Molecularly defined circuits for cardiovascular and cardiopulmonary control. *Nature* **606**, 739–746 (2022).

62.Coverdell, T. C., Abbott, S. B. G. & Campbell, J. N. Molecular cell types as functional units of the efferent vagus nerve. *Seminars in Cell & Developmental Biology* **156**, 210–218 (2024).

63.Wei, Y. *et al.* Sympathetic functional units encoded by genetically defined postganglionic neurons. *Neuron* **114**, 463-478.e7 (2026).

64.Goldstein, D. S. Differential responses of components of the autonomic nervous system. *Handb Clin Neurol* **117**, 13–22 (2013).

65.Nakamura, K., Nakamura, Y. & Kataoka, N. A hypothalamomedullary network for physiological responses to environmental stresses. *Nat Rev Neurosci* **23**, 35–52 (2022).

66.Langley, J. N. Sketch of the progress of discovery in the eighteenth century as regards the autonomic nervous system. *J Physiol* **50**, 225–258 (1916).

67.Strosberg, A. D. Structure, function, and regulation of adrenergic receptors. *Protein Sci* **2**, 1198–1209 (1993).

68.Ernsberger, U., Deller, T. & Rohrer, H. The sympathies of the body: functional organization and neuronal differentiation in the peripheral sympathetic nervous system. *Cell Tissue Res* **386**, 455–475 (2021).

69.Jänig, W. & McLachlan, E. M. Characteristics of function-specific pathways in the sympathetic nervous system. *Trends Neurosci* **15**, 475–481 (1992).

70.Berthoud, H.-R. & Neuhuber, W. L. Vagal mechanisms as neuromodulatory targets for the treatment of metabolic disease. *Ann N Y Acad Sci* **1454**, 42–55 (2019).

71.Scott-Solomon, E., Boehm, E. & Kuruvilla, R. The sympathetic nervous system in development and disease. *Nat Rev Neurosci* **22**, 685–702 (2021).

72.Ziegler, K. A. *et al.* Immune-mediated denervation of the pineal gland underlies sleep disturbance in cardiac disease. *Science* **381**, 285–290 (2023).

73.Barrett, M. S. *et al.* Ischemia-reperfusion myocardial infarction induces remodeling of left cardiac-projecting stellate ganglia neurons. *Am J Physiol Heart Circ Physiol* **326**, H166–H179 (2024).

Chapter 2

NEURAL SENSING OF INTERNAL FLUID BALANCE

This chapter focuses on fluid balance as a model to understand how neural systems detect internal needs. Fluid intake is an essential innate behavior mainly caused by two distinct types of thirst[1–3]. Increased blood osmolality drives animals to consume pure water. Conversely the loss of body fluid induces hypovolemic thirst in which animals seek both water and minerals to recover blood volume. Circumventricular organs (CVOs) in the lamina terminalis are critical sites for sensing both types of thirst-inducing stimuli[4–6]. However, how different thirst modalities are represented in the brain remains unknown. Here, we show that unique CVO excitatory neuron types are activated upon osmotic and hypovolemic stresses. Furthermore, optogenetic gain-of-function in thirst-modality-specific cell types recapitulated water-specific and non-specific fluid appetite, respectively.

In addition to central sensory neurons, this chapter explores how visceral feedback is conveyed by peripheral sensory pathways. Ingested water stimulates sensory systems in the oropharyngeal and gastrointestinal areas before absorption[7,8], which rapidly inhibits brain thirst neurons in a feed-forward manner[5,9]. Nevertheless, it remains unclear how peripheral sensory neurons detect gut osmolality changes. By *in vivo* calcium recording, we identify a dedicated population of vagal ganglion neurons that are activated by hypotonic but not hypertonic, or nutrient stimuli. These signals are transmitted through the hepatic vagal branch for suppressing thirst neuron activity. Together, these studies demonstrate that internal state monitoring is achieved through layered sensory systems in the brain and body.

Pool, A. H., Wang, T., et al. (2020). “The cellular basis of distinct thirst modalities”. In: *Nature* 588(7836), pp. 112–117. doi: 10.1038/s41586-020-2821-8.

Ichiki, T., Wang, T., et al. (2025). “Sensory representation and detection mechanisms of gut osmolality change”. In: *Nature* 602(7897), pp. 468–474. doi: 10.1038/s41586-021-04359-5.

INTRODUCTION

Detecting internal water imbalance and triggering appropriate fluid intake behavior is critical for survival in any species. In the mammalian brain, fluid imbalance is detected by CVOs in the LT, the sensory organs of the brain that lack the normal blood-brain barrier[10]. The subfornical organ (SFO) and organum vasculosum lamina terminalis (OVLT) are the forebrain CVOs that sense internal fluid status and regulate drinking behavior through their downstream brain sites. Recent studies have shown that the majority of excitatory neurons in these structures are activated under dehydration, and acute stimulation of the same population instantly drives thirst[11–13], highlighting the causal relationship between SFO and OVLT excitatory neurons with thirst.

Peripheral sensory systems such as taste and olfaction can detect multiple stimuli through distinct cell types. Similarly, the brain can detect at least two different thirst-inducing stimuli: osmolality increase and volume decrease in the systemic circulation. Moreover, these two thirst types, osmotic and hypovolemic thirst drive distinct fluid intake patterns[1]. When the brain detects osmolality elevation, animals only consume pure water to alleviate hyperosmotic stress. Conversely, reduced systemic volume induces vigorous intake of both water and salts to recover blood volume at the appropriate osmolality. Natural dehydration is a combination of these two stimuli. While both types of thirst drive drinking behavior, solute preference is drastically different in order to achieve distinct internal consequences. The work in the past several decades revealed histological and behavioral aspects of individual thirst stimuli in exquisite detail[14]. Nevertheless, the neural basis underlying distinct thirst modalities remain unexplored.

All major appetite circuits for hunger, thirst, and sodium appetite receive pre-absorptive feed-forward satiation signals after nutrient ingestion through multiple sensory systems[6–8,11]. Recent studies have shown that thirst neurons in the LT are rapidly inhibited by liquid gulping signals from the upper digestive tract and osmolality signals from the gut[15–17]. Multiple visceral afferent pathways are involved in gut osmolality sensing. Dorsal root

ganglion neurons are sensitive to hypotonic stimuli through a TRP channel possibly contributing to blood pressure regulation[18,19]. Another line of studies using vagotomy demonstrated that normal water intake is disrupted without functioning vagus nerve[20–22]. Despite these functional implications, osmolality responses in peripheral sensory ganglia have not been directly examined and characterized *in vivo*. Moreover, because sensory afferents innervate multiple organs of the gut, specific sensory sites for osmolality detection remain elusive.

CENTRAL DETECTION OF FLUID IMBALANCE

The SFO and OVLT play a key role in detecting osmotic and hypovolemic stimuli. Elevation of blood osmolality and/or loss of body fluid induces robust c-Fos expression as a proxy of neural activation (**Fig.** 1a, Extended Data **Fig.** 1a). Consistent with previous studies[1], acute osmotic stress by intraperitoneal (i.p.) injection of either hypertonic saline or mannitol triggered selective consumption of water over sodium chloride solution (**Fig.** 1b and c, Extended Data **Fig.** 1b). Acute hypovolemia by polyethylene glycol (PEG) or furosemide injection resulted in an increased appetite toward both water and salt solutions (**Fig.** 1b and c, Extended Data **Fig.** 1b). Notably, the preference toward salt was not selective to NaCl, but animals accepted other salts such as KCl (Extended Data **Fig.** 1c). Water-deprived animals showed preference toward water over salts, and sodium-deprived mice selectively consumed sodium demonstrating specific fluid appetite under distinct internal states (**Fig.** 1b). I next asked whether osmotic and hypovolemic stresses activate the same set of neurons in CVOs. To test this, we employed an activity-dependent genetic labeling strategy using transgenic mice where iCre-ER was knocked into the c-Fos gene locus (TRAP2[23]: Extended Data **Fig.** 1d). Injection of high-NaCl in the presence of 4-hydroxy tamoxifen produced robust labeling in the SFO and OVLT compared to non-stimulation control (Osm-TRAP, Extended Data **Fig.** 1e). I first compared Osm-TRAP neurons with endogenous c-Fos gene expression by hypertonic saline i.p. injection. A

majority of Osm-TRAP neurons overlap with NaCl-induced c-Fos expression validating our genetic approach (**Fig.** 1d, e). By contrast, i observed much less hypovolemia-induced c-Fos positive neurons overlapping with Osm-TRAP neurons. These results suggest that osmotic thirst and hypovolemic thirst activate unique sets of cells in CVOs.

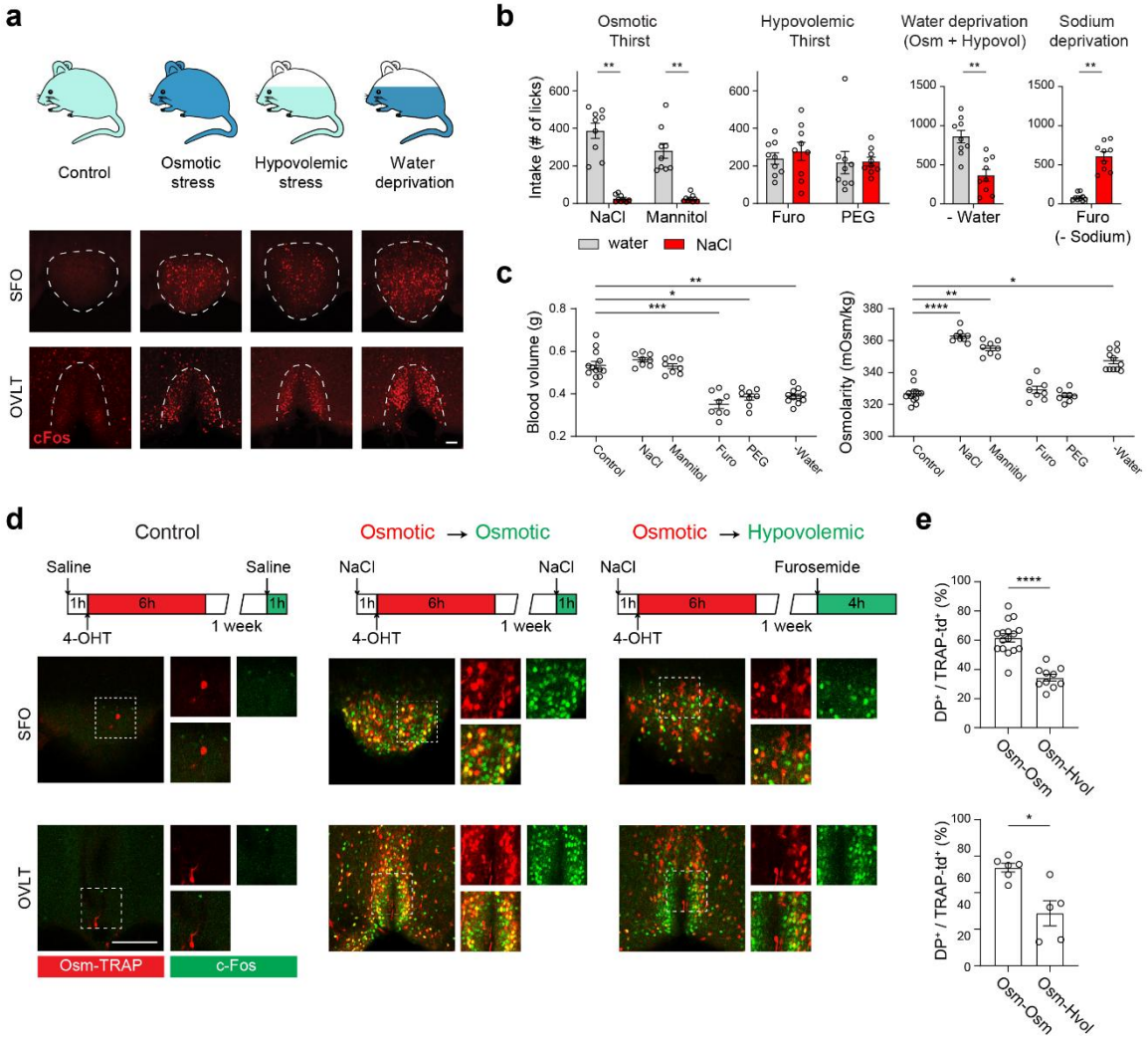

Fig. 1: Fluid consumption, physiological changes, and neural activation pattern under distinct thirst states. a, Schematic of different thirst states: sated (control), osmotic thirst (osmotic stress), hypovolemic thirst (hypovolemic stress), and water-deprivation (top). Representative images of c-Fos expression in the SFO (middle) and OVLT (bottom) under the four conditions (one from 6 mice). **b,** Water (grey) and hypertonic saline intake (0.3 M

NaCl, red) under different thirst states during a one-hour session (n = 9 mice). **c,** Blood volume and osmolality under different thirst states (n = 13 mice for control group, 8 for NaCl, Mannitol, Furo, and PEG, and 11 for water deprivation). **d,** Genetic labeling of thirst-sensitive neurons in TRAP2/Ai14 mice. Experimental design to label activated neurons under osmotic thirst and hypovolemic thirst (top). Osmolality sensitive neurons (Osm-TRAP, red) in the SFO (middle) and OVLT (bottom) overlapped with NaCl-induced acute c-Fos expression (green). Individual labeling and merged images are shown. By contrast, significantly smaller fractions of Osm-TRAP neurons were co-labeled with hypovolemia-induced c-Fos. **e,** Quantification of TRAP2 experiments (SFO: n = 16 from 8 mice for Osm-Osm, 10 from 5 mice for Osm-Hvol; OVLT: n = 6 from 4 mice for Osm-Osm, n = 5 from 4 mice for Osm-Hvol). * $p < 0.05$, ** $p < 0.01$, *** $p < 0.001$, **** $p < 0.0001$ by Wilcoxon matched-pairs signed rank test, Kruskal-Wallis test followed by a Dunn's post test or Mann-Whitney test. All error bars are presented as mean ± s.e.m. Scale bars, 50 μm.

CELLULAR COMPOSITION OF CIRCUMVENTRICULAR ORGANS

The LT contains many cell types and regulates a broad range of functions including water and salt balance, blood pressure, cardiovascular function, and neuroendocrine outputs[24,25]. However, our understanding of the molecular and cellular organization of this important brain structure is still limited. To tackle this bottleneck, we employed high throughput droplet-based scRNA-seq analysis on the 10X Genomics platform to reveal the cellular diversity in CVOs. We surgically isolated the SFO and OVLT from live brain tissue, prepared cell suspensions, and generated scRNA-seq libraries with 7950 and 6161 single-cell transcriptomes, respectively. To identify major cell classes in CVOs we performed unsupervised clustering[26,27] on a graph-based representation of the highly variable gene expression space and visualized the outcome in a UMAP-embedding (**Fig.** 2a, b). These analyses revealed 12 and 13 major cell classes in the SFO and OVLT (**Fig.** 2c, d). In addition to common cell types present in most hypothalamic structures, we found a few

specialized cell types in CVOs that may play an important role in the tissue function. For example, both the SFO and OVLT harbor a specialized endothelial cell class that is labeled by the expression of Plvap (Extended Data **Fig.** 2). This multi-transmembrane protein may contribute to the highly permeable vasculature structures[28]. Moreover, both structures contain a specialized LT astrocyte class labeled by Ucma (Extended Data **Fig.** 2a, b). Our analysis also revealed the gene expression patterns of previously-proposed osmosensory ion channels, peptide hormones and hormone receptors implicated in fluid homeostasis[29,30] (Extended Data **Fig.** 3).

We further analyzed 2642 (SFO) and 1511 (OVLT) single-cell neuronal transcriptomes (**Fig.** 2e-h). We found remarkable diversity among excitatory neurons with less pronounced differences among inhibitory neurons. We found 5 excitatory and 3 inhibitory neuron classes in the SFO (**Fig.** 2e, g) and 6 excitatory and 2 inhibitory neuron classes in the OVLT (**Fig.** 2f, h, Extended Data **Fig.** 2c-f). In accordance with previous findings, all SFO excitatory neurons and 5 of 6 OVLT excitatory neurons expressed ETV1, a genetic marker that labels dehydration-sensitive neurons[11].

To identify specific cell types involved in distinct thirst modalities, we functionally mapped thirst-activated neurons using immediate early gene (IEG) expression[31,32]. To this end, we developed and optimized a 10x Chromium-based functional cell-type mapping approach. We performed scRNA-seq experiments in the presence of a chemical transcription blocker, actinomycin-D, under four different conditions: sated, osmotic stress, hypovolemic stress, and water-deprivation (**Fig.** 3a). This enabled us to eliminate dissociation-related IEG upregulation observed in canonical scRNA-seq experiments and revealed the stimulus-induced activation pattern at a cell-type level (Extended Data **Fig.** 4). Similar to regular scRNA-seq, we identified corresponding neuron subtypes in all four conditions (Extended Data **Fig.** 5). Almost no IEG expression was observed in sated animals in any neuron types whereas most excitatory neurons exhibited robust c-Fos expression after water deprivation[12,33] (36 hours, **Fig.** 3b, c). Interestingly, we found different sets of neuron types activated under osmotic- and hypovolemic-thirst (**Fig.** 3c and Extended Data **Fig.** 4e). One

excitatory neuron class in each structure (SFO: Glut1-Htr7 and OVLT: Glut1-Bmp3) was robustly activated under hypovolemic but not under osmotic thirst. Conversely, the SFO and OVLT also harbored neurons that were selectively activated by osmotic stress (SFO: Glut5-Rxfp3 and OVLT: Glut4-Fam126a, and Glut5-Rxfp1). A few other cell types were activated under both osmotic and hypovolemic stresses (SFO: Glut4-IIrap1l2, OVLT: Glut2-Lypd6). Thus, distinct thirst states activate unique combination of cell types in CVOs. Importantly, natural water-deprivation activated both osmotic- and hypovolemic-stress activated cell types (**Fig.** 3c).

Next, we validated our transcriptomic clustering by fluorescent *in situ* hybridization (Extended Data **Fig.** 6). We focused on a pair of neuron types that are activated by different dipsogenic stimuli (SFO: Glut1-Htr7 and Glut4-Il1rapl2/Glut5-Rxfp3 labeled by Rxfp1 and OVLT: Glut1-Bmp3 and Glut5-Rxfp1). As predicted from our scRNA-seq data, each pair of genes were expressed in distinct cells. We further validated thirst-state-specific activation of single neuron classes (SFO: Glut1-Htr7, Glut5-Rxfp3; OVLT: Glut-Bmp3 and Glut4-Fam126a labeled by Cpne4). Taken together, our transcriptomic analyses on CVOs revealed that 1) each sensory nucleus contains multiple classes of “thirst neurons”, and 2) distinct dipsogenic stimuli engage unique combinations of neuron types.

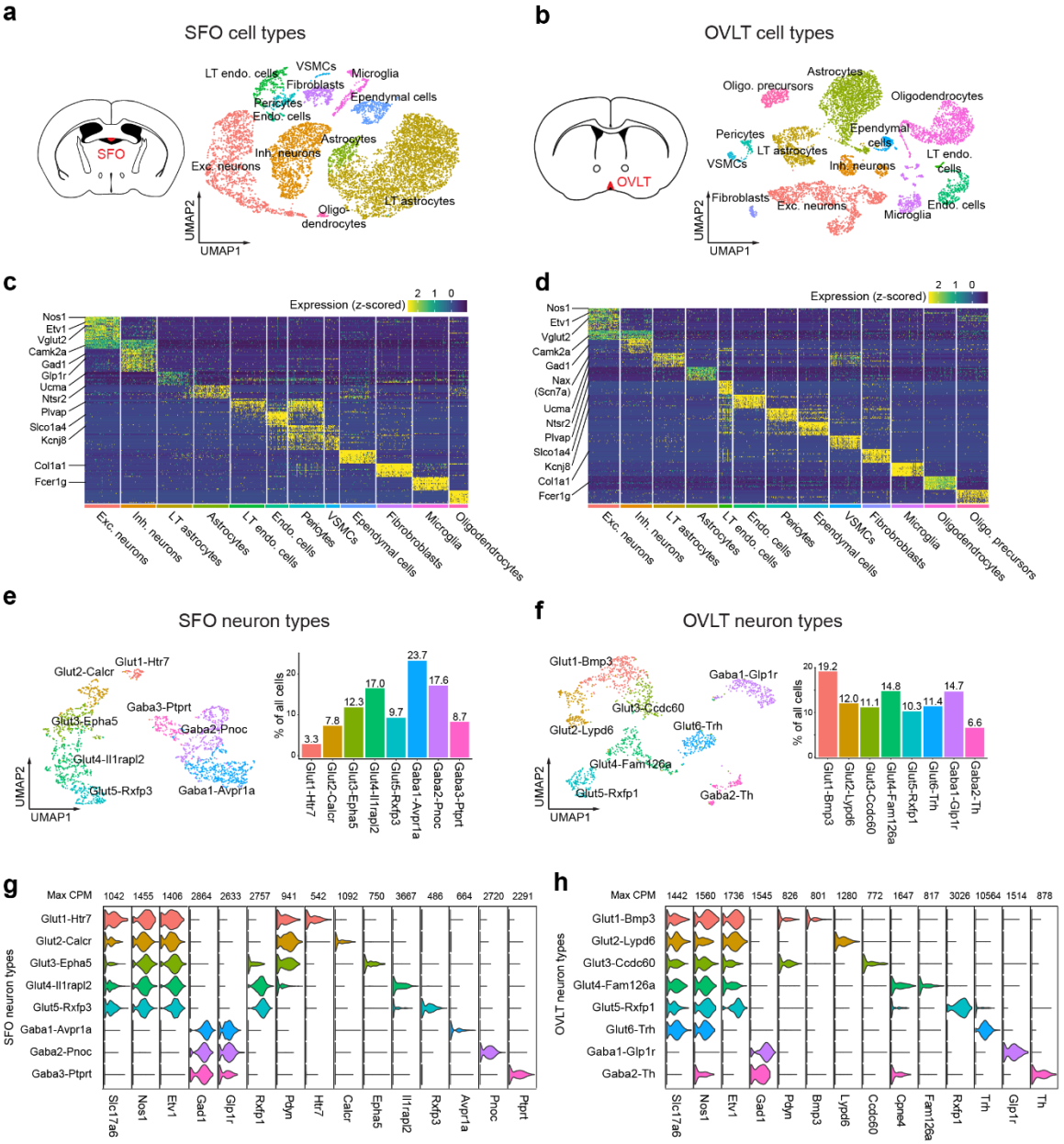

Fig. 2: Major cell types and neuron subtypes in the SFO and OVLT. a and **b,** Transcriptomic analyses of the SFO and OVLT. The SFO contains 12 transcriptomic cell types shown in a UMAP embedding of 7950 cells with color-coded cell identity (a)**,** OVLT contains 13 transcriptomic cell types from 6161 cells (b). **c** and **d,** Heat maps of cell-type-specific gene expression in the SFO (c) and OVLT (d). Gene expression is shown as z score where warmer color indicates higher gene expression. **e,** Transcriptomic analyses of SFO

neurons. The SFO contains transcriptionally distinct 5 excitatory and 3 inhibitory neuron types from 2642 cells with color-coded cell identity (left). The prevalence of each neuron type is shown (right). **f,** The OVLT contains 6 excitatory and 2 inhibitory neuron types form 1511 cells with color coded cell identity. **g,** Violin plot of cell-type-defining genes for SFO neuron types. Gene expression level for each gene is shown as maximum counts per million (max CPM). **h,** Violin plot of cell-type-defining genes for OVLT neuron types.

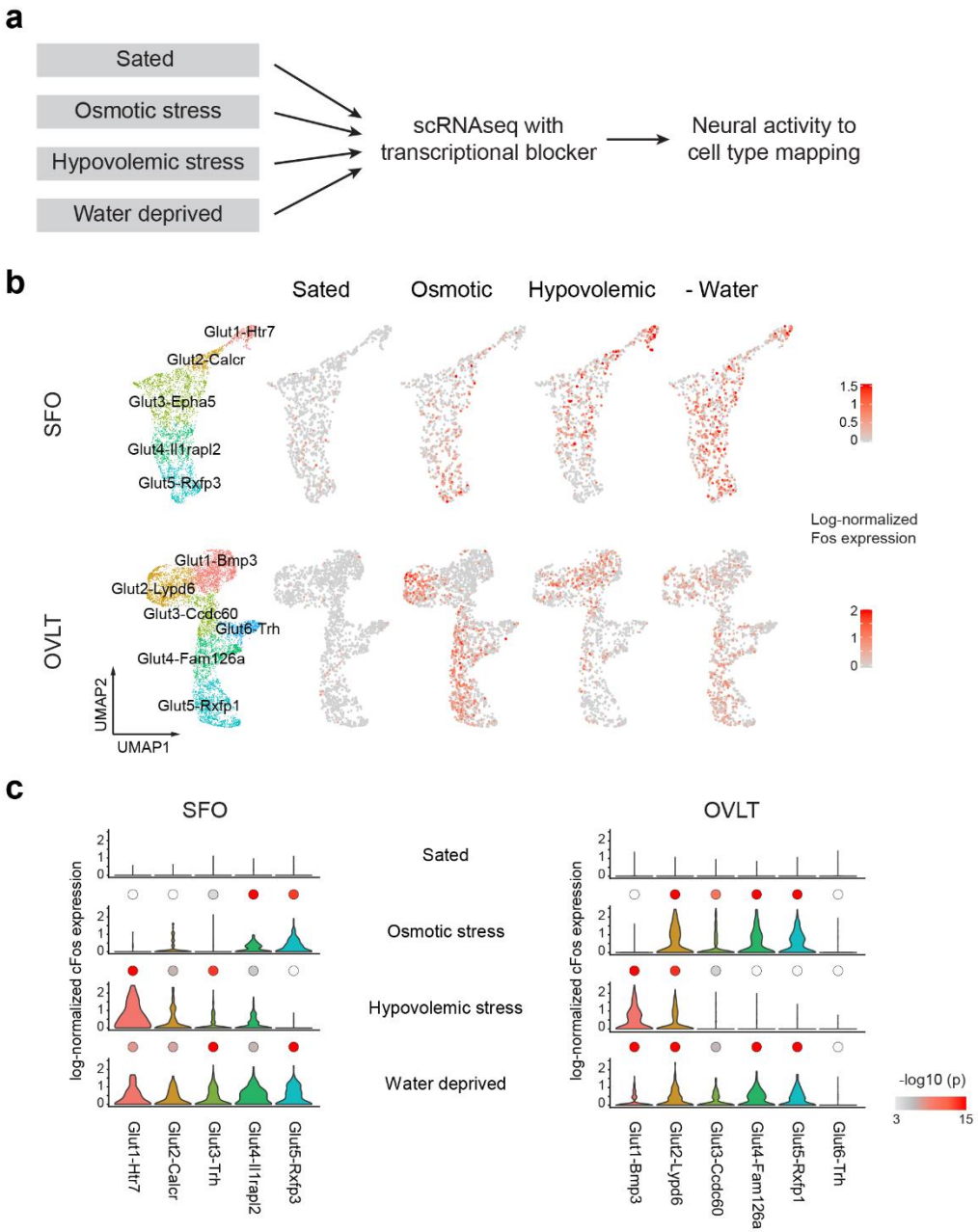

Fig. 3: Functional cell-type-mapping reveals neuron types tuned to distinct thirst states. a, Experimental design for identifying active neurons under distinct thirst states. The SFO and OVLT tissue was dissected and was subjected to scRNA-seq in the presence of actinomycin, a transcriptional blocker. Activated neuron types were mapped based on IEG expression. **b,** Neuronal data from the SFO (top) and OVLT (bottom) under four physiological conditions were aligned using Canonical Correlation Analysis (CCA) and transcriptomic cell types displayed in a UMAP embedding (n= 6540 and n = 7206 neurons for SFO and OVLT, respectively). Expression of c-Fos is plotted on log-normalized scale as a proxy for neural activation (red), showing state-dependent activation of different excitatory neuron types. For control, osmotic stress, hypovolemic stress and water deprivation states, 1866, 1403, 1772 and 1499 neurons (SFO), and 1841, 2257, 1461 and 1647 neurons (OVLT). **c,** Violin plot and Quantification of c-Fos expression in SFO and OVLT excitatory neuron types. Log scaled p-values ($-\log_{10}p$) are color-coded and indicated above each plot. Kruskal-Wallis test with Dunn's post test was used to compare cell type specific gene expression under control conditions to corresponding cell types in three experimental conditions. White color indicates $p>0.001$.

NEURAL POPULATIONS DRIVING DISTINCT FLUID INTAKE BEHAVIORS

Recent transcriptomic studies have successfully revealed cell types, spatial organization, and their putative functions[34,35]. Few cases, however, linked the causal relationship between the activity of functionally-relevant cell types and behavioral consequences. To fill this gap, we utilized the transcriptomic information to identify genetic markers that best correlate with the c-Fos activation pattern using Spearman correlation. These analyses found that Rxfp1 and prodynorphin (Pdyn) expression strongly correlate with neural activation patterns under osmotic and hypovolemic thirst, respectively (**Fig.** 4a, b and Extended Data **Fig.** 7a, b). The expression of these two genes define multiple cell types but are largely non-overlapping in the SFO and OVLT (Extended Data **Fig.** 7a-c). If osmolality-sensitive Rxfp1 neurons (SFO: Glut3-5 and OVLT: Glut5) indeed mediate

osmotic thirst, we predict that stimulation of this neural population should drive animals to consume pure water. To test this hypothesis directly, we generated knock-in mice expressing Cre-recombinase after the coding sequence of Rxfp1 (Rxfp1-Cre, Extended Data **Fig.** 7d and e). For manipulation experiments, we injected adeno-associated virus (AAV) encoding Cre-dependent channelrhodopsin2 (AAV-DIO-ChR2-EYFP) in CVOs of Rxfp1-Cre animals. We then implanted an optic fiber above the SFO or OVLT for light delivery. Upon stimulation of Rxfp1 neurons with blue light, sated animals exhibited vigorous appetite toward water, but refused to consume hypertonic NaCl and other salts (**Fig.** 4c middle panels, Extended Data **Fig.** 8a-c). This specific appetite recapitulates the natural behavior under osmotic stress.

Similarly, Pdyn expression (SFO: Glut1-4 and OVLT: Glut1 and 3) correlates well with hypovolemia-sensitive neurons (**Fig.** 4a, and Extended Data **Fig.** 7c and d). Consistent with hypovolemia-induced drinking, optogenetic stimulation of Pdyn neurons in the SFO and OVLT triggered non-specific drinking behavior toward both water and hyperosmotic salt solutions (**Fig.** 4c right panels and Extended Data **Fig.** 8a-c). Note that appetite selectivity is unrelated to fluid consumption levels (i.e., craving levels) because stimulation of both Rxfp1 and Pdyn neurons induced similar levels of total fluid intake (Extended Data **Fig.** 8d). Finally, chemogenetic inhibition of Rxfp1- but not Pdyn-positive neurons strongly suppressed osmotic-stress-induced water intake (**Fig.** 4d). Together, these results show that distinct thirst modalities are encoded by a unique set of thirst neurons, activation of which induces different drinking specificity. Importantly, optogenetic stimulation of Pdyn neurons did not drive sodium eating behavior, a typical behavior induced by sodium appetite (Extended Data **Fig.** 8e). Moreover, hypovolemic stresses did not activate sodium appetite neurons in the hindbrain[36,37] (Extended Data **Fig.** 8f). Thus, hypovolemia-induced mineral ingestion is unlikely to be a consequence of activation of sodium appetite circuits.

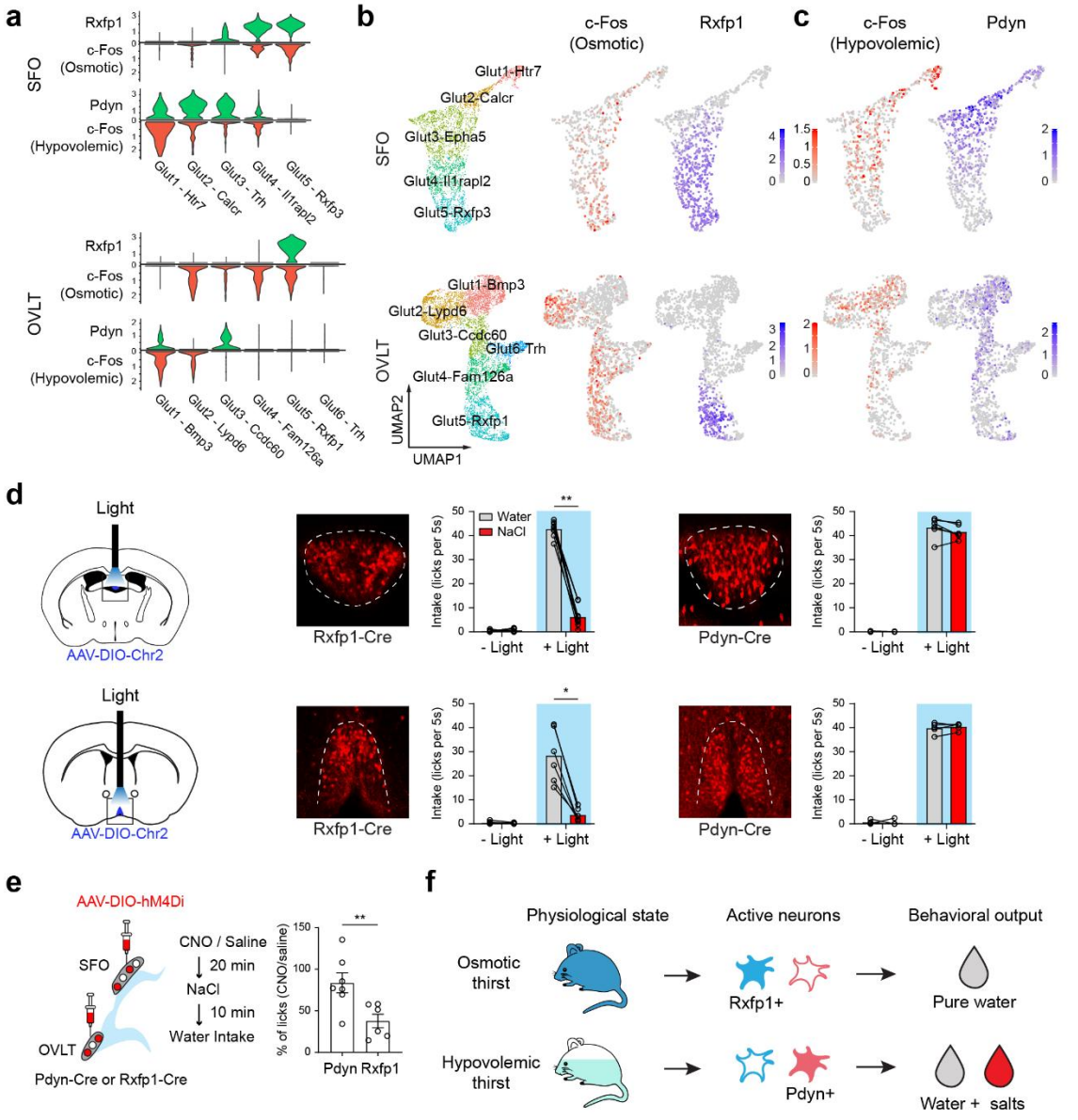

Fig. 4: Activation of thirst-state-specific cell populations in the SFO and the OVLT recapitulates thirst modality-specific drinking patterns. **a**, Violin plots of *Rxfp1* and *Pdyn* log-normalized expression in SFO and OVLT excitatory neuron types (green) compared to thirst-state-specific *Fos* expression (red) in corresponding cell types. The data were reanalysed from Figs. 2, 3. **b**, **c**, UMAP embedding for *Rxfp1* and *Pdyn* log-normalized expression (blue) in SFO (top) and OVLT (bottom) excitatory neuron types. *Fos* data are replotted for reference from **Fig.** 3b. **d**, Optogenetic activation of

osmotic stress-sensitive and hypovolaemic stress-sensitive neurons in the SFO (left) and the OVLT (right). Diagrams of optogenetic gain-of-function experiments for distinct thirst neuron subtypes (left) are shown. Representative images of *Rxfp1–Cre*-labelled cells (middle; *Rxfp1–Cre*/Ai14) and *Pdyn–Cre*-labelled cells (right; *Pdyn–Cre*/Ai3) are also included. Optogenetic activation of RXFP1 neurons drives selective drinking of pure water (middle). Consumption of pure water (grey) and 0.5 M NaCl (red) were quantified from nine mice for the SFO and six mice for the OVLT. Conversely, stimulation of PDYN neurons drives consumption of both water and hyperosmotic salt solution (right). Data were quantified from six mice for the SFO and five mice for the OVLT. Scale bar, 10 μm. **e**, Schematic of chemogenetic inhibition of *Rxfp1*-positive and *Pdyn*-positive neurons under osmotic thirst (left). NaCl (i.p.)-induced drinking was significantly suppressed by the inhibition of *Rxfp1*-positive neurons ($n = 6$ mice), but not by *Pdyn*-positive neurons ($n = 7$ mice). CNO, clozapine *N*-oxide. **f**, A diagram depicting the cellular logic underlying distinct thirst states. $^{*}P < 0.05$, $^{**}P < 0.01$, by two-tailed Wilcoxon matched-pairs signed-rank test or Mann–Whitney *U*-test. All data are shown as mean ± s.e.m.

PERIPHERAL DETECTION OF WATER IN THE INTESTINE

To examine visceral osmolality responses, we performed *in vivo* single-unit calcium recording from vagal ganglia neurons that carry the majority of gut sensory information. To achieve this, we genetically expressed GCaMP6s (*Slc17a6-Cre*;Ai96 line) in vagal sensory neurons and imaged with confocal microscopy (**Fig.** 5a). Hypo-, hyper-osmotic, and glucose infusion for an extended period (2 min) activated large fractions of vagal neurons. Notably, nearly half of these neurons responded to multiple nutrients, which may reflect a combination of sensory nutrient detection and post-absorptive physiological changes as illustrated previously[38,39] (**Fig.** 5b). To selectively visualize rapid sensory detection of osmolality, we employed a short stimulation paradigm (20 sec). With this stimulation scheme, hypotonic responses were largely segregated from hypertonic, glucose and distension responses (**Fig.**

5c). Thus, acute water sensation in the gut activates a dedicated neural population in vagal ganglia. We note that water responses were exclusively observed via intestinal, but not gastric water infusion demonstrating site-specific gut-to-brain communication.

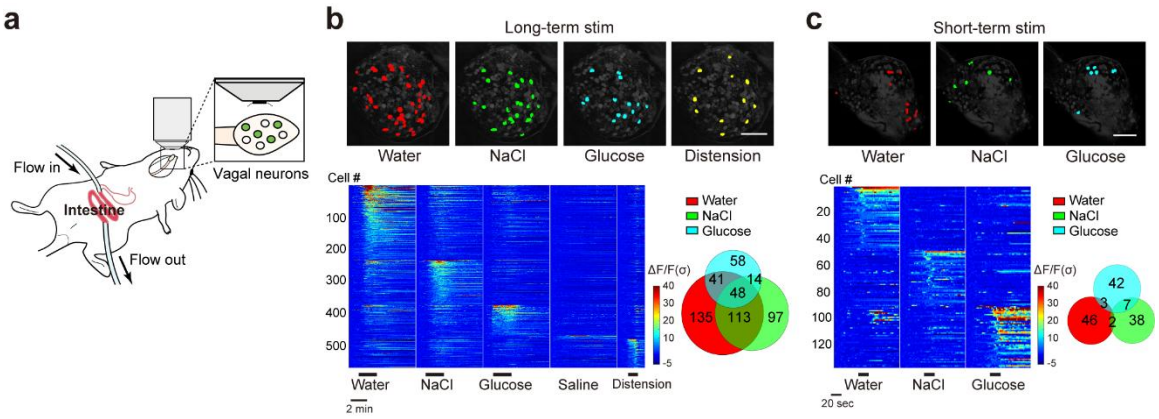

Fig. 5: Visceral hypotonic stimuli activate a dedicated vagal population. a, A diagram of confocal calcium imaging of individual vagal neurons in *Slc17a6-Cre*;Ai96 mice. **b**, Representative vagal responses (top) during the 2-min intestinal water (red), 500 mM NaCl (green), 300 mM glucose (blue) infusion and intestinal distension (yellow). Response heat map and Venn diagram for individual neural activity (n = 6 mice). **c**, Responses during shorter stimulation period (20 sec). Individual neural responses are shown in a heat map and Venn diagram (n = 7 mice). Note the minimal response overlap between different nutrients with shorter stimulation period.

VAGAL HEPATIC BRANCH IN THIRST SATIATION

How does the gut detect osmolality change? Based on potential roles of the hepatic portal area (HPA) in nutrient/water sensing[40,41], we hypothesized that sensory signals from the HPA may play a role in gut osmolality detection. To directly test this possibility, we performed branch-specific loss-of-function study using surgical denervation combined with *in vivo*

imaging. Acute hypotonic responses were abolished after selective denervation of hepatic vagal branch (HVx) while responses to intestinal distension remained largely intact (**Fig.** 6a). Consistent with previous reports, the responses to other nutrients were also blunted by HVx[42,43] (Extended Data **Fig.** 9a).

Previous studies have established that gut water detection rapidly transmits pre-absorptive satiation signals to the brain and inhibits water intake[16,17]. Given the sensory function of the HPA, we next investigated whether HPA-derived water signals mediate thirst satiation. To this end, we subjected animals to water restriction and measured water intake with or without HPA sensory inputs. Animals lacking HPA afferents exhibited significantly increased water consumption after 24-hour water deprivation (**Fig.** 6b). However, spontaneous daily water intake did not change regardless of vagal inputs (Extended Data **Fig.** 9b). These results suggest that HPA-denervation specifically affects thirst satiation under water-deprived states.

Thirst neurons receive two types of feed-forward satiation signals: rapid inhibition by liquid gulping and sustained inhibition by gut osmolality detection. The vagal pathway was suggested to play a role in these satiation signals[16,22]. If the HPA is involved in osmolality-induced satiation, we expected that sustained inhibition of thirst neurons should be selectively abolished after HVx. To examine this idea, we virally expressed GCaMP in NOS1-positive thirst neurons in the subfornical organ (SFO). The activity of thirst neurons was then recorded through an implanted optic fiber with or without HPA inputs (**Fig.** 6c). These neurons were robustly activated by osmotic challenge (intraperitoneal injection of NaCl solution) and rapidly suppressed upon fluid intake under dehydrated states (**Fig.** 6d, e). With intact vagal function, sustained neural inhibition was observed after water intake whereas this osmolality-induced inhibition was significantly reduced after HVx (**Fig.** 6e, top panels). Importantly, gulping-induced rapid inhibition was unchanged by the same operation (**Fig.** 6e, bottom panels). These functional data demonstrate a selective role of HPA-innervating vagus nerve in osmolality-induced thirst modulation.

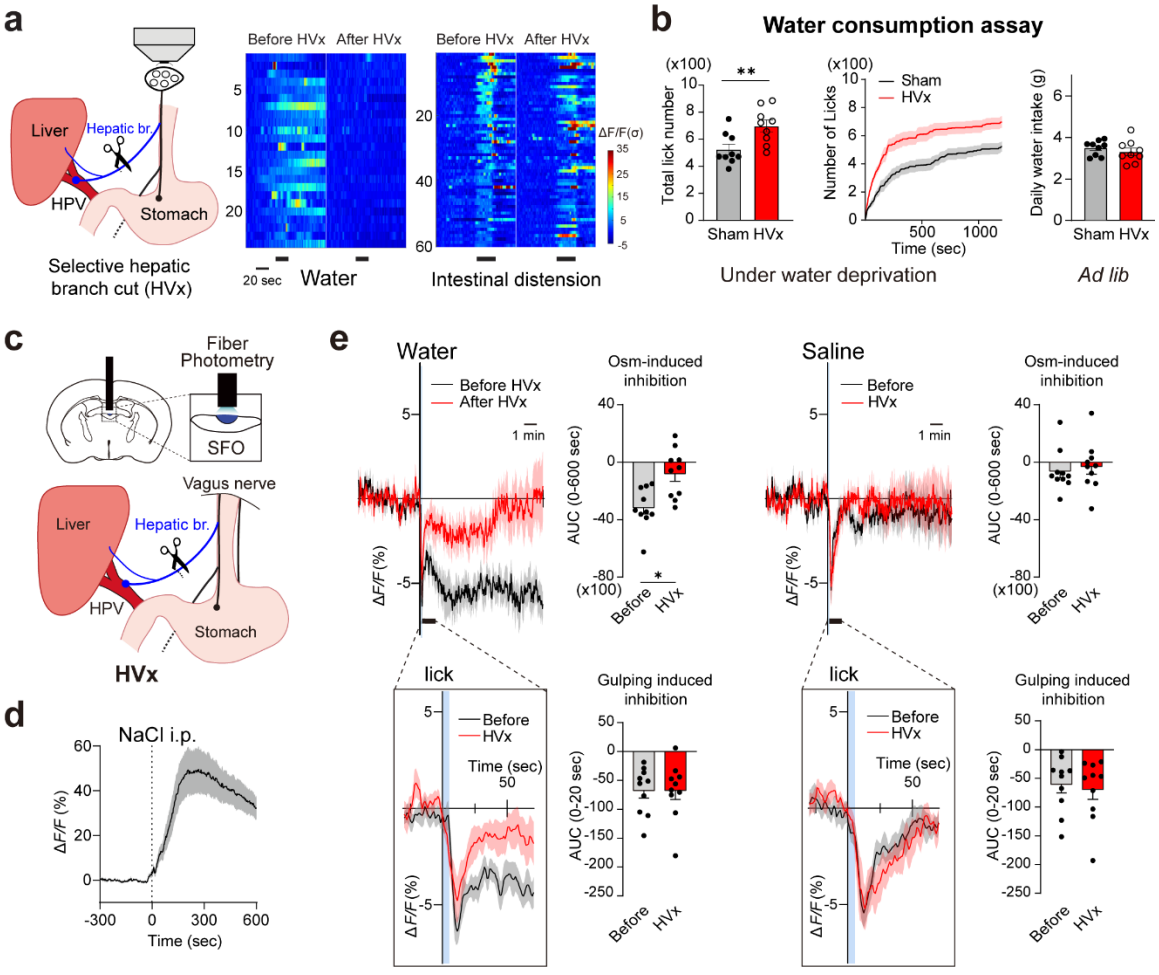

Fig. 6: Vagal sensory inputs from the HPA transmits gut-to-brain osmolality signals. a, The effect of hepatic branch loss-of-function (HVx) on acute water responses. Response heat maps for intestinal water infusion and distension (*Slc17a6-Cre*;Ai96, n = 3 mice). Responding neurons after HVx are quantified as a percentage of those before HVx (less than 1% for water, 72% for distension). **b,** Effect of HVx on water consumption. Water intake during a 20-min session were quantified after 24 hours of water restriction in sham (grey) and HVx (red) animals (n = 9 mice). Importantly, spontaneous daily water intake was not affected (n = 9 mice). **c,** A diagram of optical recording from LT thirst neurons before and after HVx. Thirst neuron activity was recorded by injecting AAV-CaMKII-GCaMP6s into wild-type animals or AAV-Flex-GCaMP6s into *Nos1-Cre* animals. **d,** Thirst neurons are acutely activated by intraperitoneal injection of hypertonic saline (2M NaCl, n = 10 mice).

e, Calcium dynamics and quantified responses (AUC) of thirst neurons after fluid intake (n = 10 mice). Water intake induces rapid and sustained inhibition in intact animals. After HVx, sustained osmolality-induced inhibition was significantly blunted (left top). Conversely, gulping-induced inhibition was unchanged (left bottom). Isotonic saline intake only induced rapid inhibition to thirst neurons (right). Blue shade indicates the drinking period (5 sec). $*P < 0.05$, $**P < 0.01$ by two-tailed Mann-Whitney *U*-test and two-tailed paired *t* test. Data are presented as mean ± s.e.m.

DISCUSSION

In the past half-century, it has been well established that CVOs play a pivotal role in fluid homeostasis[10]. However, the precise molecular census has not been established to date. Our single-cell transcriptomic study revealed comprehensive cell types in the SFO and OVLT, two critical sensory organs that monitor internal water balance. ScRNA-seq-based stimulus to cell-type mapping further unveiled unique cell types involved in two distinct thirst states caused by either systemic hyperosmolality or hypovolemia. These results elucidated the cellular basis of two thirst modalities (**Fig.** 4e).

One of the common functions of peripheral sensory systems is to distinguish among different stimulus qualities (e.g., sweet vs bitter). This enables animals to react and behave appropriately toward different stimuli. Our study shows that this principle is also true for central sensory systems. We show anatomical and functional evidence that thirst consists of two distinct modalities represented by unique neural ensembles in the brain. Stimulation of osmolality- and hypovolemia-sensitive neurons drives different drinking patterns to restore the deficits caused by each stress. Furthermore, these two types of thirst neurons are housed in the same brain structures, which highlights the similar coding principles employed by the peripheral systems.

In various mammalian species, the brain has two osmosensory organs, the SFO and OVLT, which are functionally redundant for sensing internal water balance. Our transcriptomic analyses enabled a systematic comparison between these two structures at both molecular and cellular levels. Two CVOs largely share corresponding major cell classes and neuron types, and gene expression patterns related to potential osmoregulatory molecules (Extended Data **Fig.** 3c, d). These results suggest that the SFO and OVLT are parallel entry points that independently sense body fluid imbalance, and drive dedicated downstream behaviors. However, I found that astrocytes in the SFO, but not OVLT are strongly activated by osmotic stress. Thus, SFO astrocytes may have a dedicated function in fluid regulation[44].

Previous studies defined excitatory neurons in the LT as thirst neurons using two criteria. First, they are activated under dehydration, and second, stimulation of these neurons drives drinking behavior[11–13]. However, we show that these neurons contain at least two functionally distinct components: one for water-specific appetite, and another for non-specific fluid appetite. These neuron groups are labeled by the expression of Rxfp1 and Pdyn. Interestingly, Rxfp1 and Pdyn neurons comprise multiple transcriptomic cell types among excitatory neurons. It would be important to investigate how individual cell types contribute to different thirst states. Our results stress the importance of dissecting neural circuit function at the level of transcriptomic cell types and that functionally-defined neuronal groups often contain subpopulations that have related but distinct functions to achieve a given behavior.

Gut osmolality change induces distinct types of vagal responses: hypotonic specific and general responses. HVx selectively eliminates hypotonic responses suggesting that gut osmolality changes stimulate multiple vagal pathways. Importantly, non-specific nutrient responses emerged with an extended gut stimulation as indicated previously[38,39]. We speculate that rapid hypotonic-specific responses represent sensory detection of osmolality change whereas general responses may be a consequence of delayed physiological effects such as blood pressure or heart rate changes. It is important for future work to investigate how different types of osmolality/nutrient responses contribute to appetite regulation and other physiological changes.

Physiologically and behaviorally, the importance of gut osmolality sensing for thirst regulation has been recognized for decades. Recent studies provided more insights into the neural and molecular mechanisms underlying water detection. Nevertheless, *in vivo* sensory responses to gut water stimuli are not fully understood. In this study, we characterize osmolality responses in sensory ganglia and demonstrate that the vagal pathway transmits gut-to-brain thirst satiation signals. We show that intestinal water stimuli induce hypoosmolality-specific and general osmolality/nutrient responses in vagal neurons, of which the former responses are exclusively mediated by sensory afferents from the HPA. Moreover, we show that HPA-derived sensory signals contribute to feed-forward satiation and thirst-circuit modulation (**Fig.** 6e). This study reveals peripheral representation, signal transmission pathway, and functional significance of gut hypoosmolality sensing.

EXPERIMENTAL MODELS AND METHOD DETAILS

Animals

All animal care and experimental procedures were carried out in accordance with the US NIH guidance for the care and use of laboratory animals and approved by California Institute of Technology Animal Care and Use Committee (protocol #1694-14). Mice used for behavioral experiments were both male and female, at least eight weeks of age. For scRNA-seq experiments determining SFO and OVLT cellular nomenclature we used 7.5 – 8 week old C57BL/6J male mice with tissue accumulated from 8-12 animals per structure. For neural activity to cell type mapping related scRNA-seq experiments we used a total of 48 C57BL/6J animals (24 male and 24 female divided in equal counts between 4 experimental batches) at 7.5-8 weeks of age. The following mice were purchased from the Jackson Laboratory: C57BL/6J (JAX strain 000664); Ai3, (JAX strain 007903); Ai14 (JAX strain 007914), Ai96 (JAX stock #028866). Pdyn–Cre mice were a gift from B. Lowell and M. Krashes. TRAP2 mice were a gift from Liqun Luo. *Slc17a6* (Vglut2)-*Cre* (*Slc17a6*^{Cre}) mice were a gift from V. Gradinaru. Mice were housed in temperature- and humidity-controlled rooms with a 13 hours:11 hours light:dark cycle with *ad libitum* access to chow and water.

Generation of Rxfp1-P2A-Cre mouse line

Rxfp1-P2A-Cre animals were created by nucleofection of 10^6 v6.5 mouse embryonic stem cells (C57/BL6;129/sv; a gift from R. Jaenisch) with ribonucleoprotein (RNP) complexes composed of SpCas9-NLS protein and in vitro transcribed sgRNA (ACTCAATTCTTATTCGTAAC). To enable homology directed repair (HDR), a repair construct in which P2A-Cre was flanked with sequences homologous to the target site was cotransfected with RNP complexes. Colonies grown from transfected cells were directly screened for successful integration. The inserted transgene was fully sequenced from positive clones. Candidate lines were also analyzed for normal karyotype. The first line passing quality control was aggregated with albino morula and implanted into pseudopregnant females, which produced germ line competent chimeric founders.

Viral constructs

The following AAV viruses were purchased from Addgene: AAV5-EF1a-DIO-ChR2-EYFP (Addgene #20298-AAV5), $3.0 \cdot 10^{13}$ viral genomes per ml. AAV8-DIO-hM4Di-mCherry (Addgene #44362), $1.9 \cdot 10^{13}$ viral genomes per ml. AAV1-Syn-Flex-GCaMP6s (100845-AAV1), 2.9×10^{13} viral genomes per ml.

Surgery

Surgery procedures were performed as previously described[12]. Briefly, animals were anesthetized with a mixture of ketamine (1 mg/ml) and xylazine (10 mg/ml) in isotonic saline, injected intraperitoneally (i.p.) at a dose of 10 µl/g bodyweight. Ketoprofen was also subcutaneously administered at 5 µl/g bodyweight. The mouse was then placed in a stereotaxic apparatus (Narishige #SR-5M-HT) on a heating pad at 37 °C. Mouse skull was exposed by an incision of the scalp followed by application of the topical analgesic bupivacaine (2.5 mg/ml). A small craniotomy, less than 1 mm, was made using a hand drill at the regions of interest. Virus injections were performed with pulled glass pipettes using a microprocessor-controlled injection system (World Precision Instruments, Nanoliter 2000) at 100 nl/min. SFO virus injections were performed using the following stereotaxic coordinates with respect to the lambda aligned bregma point: + 800 µm A/P, 0 µm M/L, +2800 µm below the surface of the skull. OVLT virus injections were performed using the following stereotaxic coordinates: -500 µm A/P, 0 µm M/L, +5260 µm below the surface of the skull. Total of 50 – 90 nL of virus was delivered per injection. For optogenetics experiments, optogenetic implants were prepared by gluing a 200-µm diameter optic fiber (Thorlabs, FT200EMT) to a ceramic ferrule (CF230-10, Thorlabs) with epoxy glue. The implants were placed 300 µm above the virus injection site and attached to the skull with Vetbond (SCB, sc-361931) and dental cement (Lang Dental Mfg. Co, #4720FIB, #Jet Liquid). All mice were placed in a clean cage on a heating pad overnight to recover, and were then housed in the animal facility. Behavioral tests were performed after at least 10 days of recovery. At the end of experiments, all animals were euthanized and histologically examined for virus expression as well as the fiber implant position.

Fiber photometry

Surgery for photometry was performed as previously described[17]. In brief, mice were anesthetized with a mixture of ketamine and xylazine solution. The animal was then placed in a stereotaxic apparatus (SR-5M-HT, Narishige) on a heating pad at 37 °C. A total of 150-300 nL viral constructs were injected using a microprocessor-controlled injection system (Nanoliter 2000, World Precision Instruments) at 100 nL/min. SFO virus injections were performed using the following stereotaxic coordinates; AP: −4030, ML: 0, DV: −2550. For photometry, a 400-μm diameter optic fiber (FT400UMT, Thorlabs) and a ceramic ferrule (CF440, Thorlabs) were glued to be implanted to SFO. Virus expression and fiber implant position was verified after data collection.

Bulk fluorescence signals were collected using fiber photometry as previously described [6,13,41]. In brief, GCaMP signals were extracted and subjected to a low-pass filter at 1.8 Hz. To obtain the fitted 405-nm signal, a linear function was used to scale up the 405-nm to 490-nm channel signal. The change in fluorescence intensity (ΔF/F) was calculated as (raw 490 nm signal – fitted 405 nm signal) / (fitted 405 nm signal), and then time-binned by a factor of 2.5 times the sampling frequency and down-sampled to 1 Hz. For all photometry assays, animals were acclimatized for at least 15 min in the chamber before the stimuli were presented. Animal licks were simultaneously recorded. The AUC was quantified by integrating the baseline-subtracted fluorescence signals for 10 min for the osmolality-induced inhibition, 20 sec for the gulping-induced inhibition after the first bout.

Gastrointestinal infusion

A skin incision was made along the abdominal midline. For the intestinal input port, a tubing (60-011-04, HelixMark®) was inserted in the proximal duodenum (within 0.5 cm from the sphincter) in the initial set of experiments. For the remaining experiments to test the HPA function, the input port was set at the jejunum (5 cm from the sphincter) to eliminate the duodenum contribution to osmolality responses through the hepatic branch. The exit port (60-011-09, HelixMark®) was made in the distal intestine before the cecum. Surgical thread

(K802H, Ethicon) was used to fasten and secure tubing sites. Intestinal distension was achieved by temporally closing the exit port while infusing saline.

For gastric infusion, a small incision was made in the fundus of the stomach for the input port. The output tubing was inserted through a duodenum incision into the stomach. Gastric distension was achieved by volume-controlled manual inflation of a surgically implanted latex balloon (73-3478, Harvard Apparatus).

Gastrointestinal contents were flushed with isotonic saline before experiments. Different fluid stimuli were delivered by switching solenoid valves with Arduino. Stimuli used were deionized water, 1 M or 500 mM NaCl, 300 mM glucose, 4% Acetic acid, and Ensure. All solutions were warmed up to 37°C.

Vagal hepatic branch transection

Mice were anesthetized with a mixture of ketamine (100 mg/kg body weight) and xylazine (5 mg/kg body weight) intraperitoneally. Ketoprofen was subcutaneously administered at 5 mg/kg body weight and buprenorphine SR (1 mg/kg body weight) was applied prior to surgery. Animals were placed on their backs and the abdomen was incised along the midline. The hepatic branch was completely transected for the hepatic-branch-specific cut. Sham-operated mice were subjected to all the surgical procedures except the nerve operation.

***In vivo* vagal ganglion imaging**

Vagal ganglion imaging was performed as previously described[38,39]. Briefly, 16-hour fasted animals were anesthetized with pentobarbital. We exposed the vagal ganglion by retracting the carotid artery, and the vagus nerve was transected superior to the jugular ganglion. The ganglion was then immobilized on a custom 5-mm diameter glass coverslip station, and immediately immersed in the silicon adhesive (KWIK-SIL, World Precision Instruments). Imaging was conducted with Leica SP8 confocal microscope, framing rate at 1Hz. Less than 10 μW laser power was used to prevent tissue damage.

Imaging data was analyzed using modified MATLAB scripts based on CaImAn-MATLAB[45]. Briefly, Imaging frames collected from the same animal were registered to correct for motion artifacts. Constrained non-negative matrix factorization (CNMF) algorithm was used to recognize individual cells and to extract the Ca^{2+}-activity traces. CNMF outputs were manually inspected to remove neuropil or other non-neuronal signals. For calculating sensory responses, 25 sec (10 sec for DRG imaging) before the stimulus onset was used as baseline period. The responses are reported in units of baseline standard deviation (σ) as previously published[37]. The mean (μ) and standard deviation (σ) of F0(t) over a baseline period were computed as $F(t) = (F0(t) - \mu)/\sigma$. Cells were defined as responsive to each stimulus if the average $\Delta F/F(\sigma)$ value during the stimulus period exceeded 2.5 s.d..

Optogenetic manipulation

For optogenetic photostimulation, 473-nm laser pulse sequences (20 ms, 20 Hz, 30 sec pulse sequence) were delivered via an optic cable (MFP-FC-ZF, Doric Lenses) using a pulse generator (World Precision Instruments, SYS-A310) for all behavioral assays performed in the custom gustometer (Dialog Instruments). For rock salt experiments, pulse sequences (20 ms, 20 Hz, repeated pulse sequence of 1 sec on, 3 sec off) were generated by a pulse generator (Quantum Composers, Sapphire 9200). The laser intensity was maintained at 5 mW at the tip of the fiber.

Induction of physiological states

Osmotic thirst was induced by an intraperitoneal (i.p.) injection of either 2 M NaCl (5 μl/g bodyweight) or 2 M mannitol solution (10 μl/g bodyweight). After 10 min in the home cage without food or water, animal behavior was tested. For immunohistochemistry or scRNA-seq, animals were kept in the home cage without access to food or water for one hour to allow for stimulus induced expression of immediate early genes.

Hypovolemic thirst was induced either by an i.p. injection of furosemide (Sigma, F4381) at a dose of 50 mg/kg bodyweight or subcutaneous (s.c.) injection of 40% polyethylene glycol (PEG, Sigma, 89510) at a dose of 10 mg/kg body weight. Mice stayed in a clean cage without food or water for either 3 hours after furosemide injection or 6 hours after PEG administration followed by behavioral testing. Tissue collection for immunohistochemistry or scRNA-seq was done either 4 hours after furosemide or 7 hours after PEG administration.

For water deprivation experiments, animals were kept in their home cages without water for 36 hours, and were provided with food and 1 ml of water daily. For sodium-restriction experiments, a low-sodium diet (Envigo, TD. 90228) and water were provided for one day after furosemide injection at a dose of 50 mg/kg bodyweight. After that, animals were tested for behavior or sacrificed for scRNA-seq as well as immunohistochemistry experiments. All animals were given at least two days on the normal diet to recover after each treatment.

Behavioral assays

All behavioral assays were performed in a custom gustometer (Dialog Instruments) system, unless otherwise noted. Animals used were water deprived 24 hours for training in the gustometer before behavioral assays. For two-choice consumption preference assay, one bottle of water and one bottle of mineral solution (0.3 M or 0.5 M NaCl, 0.3 M or 0.5 M KCl, 0.05 M $MgCl_2$, or 0.05 M $CaCl_2$) were presented in sequence during the same session as previously described, measuring the number of licks towards different solutions[11]. For **Fig.** 1 and Extended Data **Fig.** 1, mice of different thirst states were recorded for an hour containing a number of 60-sec trials. After the first lick of each trial, mice had ad libitum access to the spout for 5 sec. There is a 10-sec interval between each trial.

For optogenetics experiments, 30 sec of photostimulation was delivered to sated animals for each trial, with an inter-trial-interval of 60 sec. Animals were given 5 sec access to solution within one trial. Using the same two-choice preference assay, we measured animal consumption preference for 10 trials in total. To evaluate total fluid intake caused by photostimulation, one bottle of water was presented to the same testing animals for 20 trials.

For chemogenetic inhibition experiments, CNO was administrated at 10 mg/kg body weight, 20 min before osmotic thirst induction. Animals were then provided with a bottle of water for 30 min.

During the training session of rock salt experiments, sodium deprived animals were accustomed for an hour in a transparent acrylic box (50 cm x 25 cm x 25 cm) with a rock salt (Halite Himalayan Crystal Salt) fixed in one corner. Lick events of animals were monitored for 30 min using a webcam under sated, photostimulated and sodium-deprived conditions, and bout frequency was manually quantified. For the photostimulation experiments, animals received pulses for one second every four seconds during the entire 30-min session.

Immunohistochemistry

Mice were euthanized with CO_2 and perfused with PBS followed by 4% paraformaldehyde (PFA, pH=7.4). Mouse brains were extracted, post-fixed overnight at 4°C in 4% PFA and coronally sectioned at 100 μm intervals on a vibratome (Leica, VT-1000s). Brain sections were blocked (10% donkey serum, 0.2% Triton X-100 in PBS) for an hour at room temperature followed by overnight primary antibody incubation in block buffer at 4°C. The following primary antibodies were used: rabbit anti-c-Fos (1:500, Cell Signaling, #2250), sheep anti-FOXP2 (1:2000, R&D Systems, AF5647), rabbit-anti-ETV1 (1:500, Abcam, ab81086), chicken anti-GFP (1:1000, Abcam, ab13970), rat anti-mCherry (1:500, Invitrogen, 16D7). After washing 3 times with PBS, the brain sections were stained with secondary antibodies (1:500, Jackson Immunoresearch) and DAPI (2 μg/ml) for 4 hours at room temperature. After another 3 PBS washes, sections were mounted on glass slides and imaged on a confocal microscope (Leica, TCS SP8).

Genetic labeling of stimulus activated cell types (TRAP2)

Detailed generation and characterization of TRAP2 animals were described in previous studies[23]. We crossed TRAP2 animals with Ai14 animals and used double-positive mice for genetic labeling experiments. Food and water were removed after inducing osmotic thirst by

injecting hypertonic saline (i.p.) as described above. 4-hydroxytamoxifen (4-OHT) (Sigma H6278) was dissolved at 20 mg/ml in pure ethanol by shaking at 37 °C for 15 min. The dissolved 4-OHT was mixed with double volume of corn oil (Sigma C8267) at room temperature for 15 min. Ethanol was evaporated in vacuum centrifugation. The final 10 mg/ml 4-OHT solution was injected (i.p.) at a dose of 50 mg/kg an hour later. Water and food were returned 6 hours after 4-OHT administration. Mice were given 1 week for fluorescent reporter expression before subjecting them to either osmotic thirst or hypovolemic thirst induction followed by immunohistochemistry for c-Fos expression.

Blood volume and osmolality measurements

After inducing different thirst states, trunk blood was collected from 8-week old C57BL/6J male mice. Extracted blood volume was quantified by weight. Plasma was then separated by centrifugation at 1600 *g* for 20 min. Plasma osmolality was measured using an osmometer (Vapro 5520).

Tissue processing into single cell suspensions and sequencing library construction for 10x scRNA-seq

7.5-8 week old animals were anaesthetized with isoflurane in an isolated plexiglass chamber. Brains were rapidly extracted and dropped into ice cold carbogenated (95% O2, 5% CO2) NMDG-HEPES-ACSF (93 mM NMDG, 2.5 mM KCl, 1.2 mM NaH_2PO_4, 30 mM $NaHCO_3$, 20 mM HEPES, 25 mM glucose, 10 mM $MgSO_4$, 1 mM $CaCl_2$, 1 mM kynurenic-acid Na salt, 5 mM Na-ascorbate, 2 mM Thiourea, 3 mM Na-pyruvate, pH adjusted to 7.4, osmolarity ranging 300 – 310 mOsm). 2 mm brain sections containing either SFO or OVLT were cut with a razor blade on a stainless steel brain matrix (Stoelting #51392) and transferred to a dissection dish on ice containing NMDG-HEPES-ACSF. For SFO microdissections, the surface of the fornix was exposed and SFO was peeled off with forceps by grabbing the posterior end of the SFO and extracting the structure. For OVLT, the abdominal anterior surface of the 3rd ventricle containing the OVLT was exposed with forceps and OVLT was extracted by cutting out a triangular shape of tissue (height ~350 microns, base ~350 microns,

depth 150 microns from the surface of the 3rd ventricle) with microsurgical stab knife (Surgical Specialties #72-1501). Microdissected tissue was aggregated from 8-12 animals per scRNA-seq run (12 animals for SFO and 8 animals for OVLT) in a collection tube on ice containing NMDG-HEPES-ACSF. For enzymatic digestion of tissue NMDG-HEPES-ACSF was replaced by Trehalose-HEPES-ACSF (92 mM NaCl, 2.5 mM KCl, 1.25 mM NaH_2PO_4, 30 mM $NaHCO_3$, 20 mM HEPES, 25 mM glucose, 2 mM $MgSO_4$, 2 mM $CaCl_2$, 1 mM kynurenic-acid Na salt, 2.5 wt/vol trehalose, pH adjusted to 7.4, osmolarity ranging 330 – 340 mOsm) containing papain (60 U/ml Sigma Aldrich #P3125, pre-activated with 2.5 mM cysteine and a 30 min incubation at 34 ºC and supplemented with 0.5 mM EDTA). Extracted SFO and OVLT tissue was incubated at 34 ºC with gentle carbogenation for 1 hour 20 min and 50 min, respectively. During enzymatic digestion the tissue was pipetted periodically every 10 min. At the end of enzymatic digestion the medium was replaced with 200 µl of room temperature Trehalose-HEPES-ACSF containing 3 mg/ml ovomucoid inhibitor (Worthington #OI-BSA) 25 U/ml DNAse I (Thermo Scientific #90083) and tissue was gently triturated into a uniform single cell suspension with consecutive rounds of trituration with fire-polished glass Pasteur pipettes with tip diameters of 600, 300 and 150 µm. Resulting cell suspension volume was brought up to 1 ml with Trehalose-HEPES-ACSF with 3 mg/ml ovomucoid inhibitor and pipetted through a 40 µm cell strainer (Falcon #352340) into a new microcentrifuge tube. Thereafter, the single cell suspension was centrifuged down at 300 *g* for 5 min at 4 ºC and the supernatant replaced with fresh ice cold Trehalose-HEPES-ACSF and cell pellet resuspended. Cells were pelleted again and resuspended in 100 µl of ice-cold Resuspension-ACSF (117 mM NaCl, 2.5 mM KCl, 1.25 mM NaH_2PO_4, 30 mM $NaHCO_3$, 20 mM HEPES, 25 mM glucose, 1 mM $MgSO_4$, 2 mM $CaCl_2$, 1 mM kynurenic-acid Na salt, 0.05% BSA, pH adjusted to 7.4, osmolarity ranging 330 – 340 mOsm) compatible with 10x reverse transcription chemistry (i.e. lacking trehalose and reduced Mg^{2+}). Cell suspensions were kept on ice while cell densities were quantified with a hemocytometer and final cell densities were verified to be in the range of 300 – 1000 cells/µl. Cell suspension volumes estimated to retrieve ~8000 single-cell transcriptomes were added to the 10x Genomics RT reaction mix and loaded to the 10X Single Cell A chip (10x Genomics #230027) per manufacturer's protocol. We used the Chromium Single Cell 3' Library and Gel Bead Kit

v2 (10x Genomics #120237) and Chromium i7 Multiplex Kit (#120262) to prepare Illumina sequencing libraries downstream of reverse transcription following manufacturer's protocol applying 12 rounds of cDNA library amplification and 11 rounds of sequencing library amplification.

Tissue processing into single cell suspensions and sequencing library construction for neural activity to cell-type mapping

In order to reveal endogenous immediate early gene expression with 10x Genomics based scRNA-seq and block tissue processing related artificial induction of IEG levels, a number of changes were made to single cell suspension generation protocol. Brains were extracted from 12 animals following respective physiological state induction as described above. 3 mm tissue sections containing both SFO and OVLT were cut out on a stainless steel brain matrix and both structures were microdissected. Extracted SFO and OVLT tissues were collected into separate microcentrifuge tubes on ice containing NMDG-HEPES-ACSF and 30 µM actinomycin D. For enzymatic digestion of tissue NMDG-HEPES-ACSF was replaced by Trehalose-HEPES-ACSF containing papain (80U/ml Sigma Aldrich #P3125, pre-activated with 2.5 mM cysteine and a 30 min incubation at 34ºC and supplemented with 0.5 mM EDTA) and 15 µM actinomycin D. Extracted SFO and OVLT tissue was incubated at room temperature with gentle carbogenation for 1 hour 45 min and 1 hour 15 min for SFO and OVLT, respectively. During enzymatic digestion the tissue was pipetted periodically every 10 min. At the end of enzymatic digestion the medium was replaced with 200 µl of room temperature Trehalose-HEPES-ACSF containing 3 mg/ml ovomuccoid inhibitor, 25 U/ml DNAse I and 15 µM actinomycin D. Tissue was gently tritruted into a uniform single cell suspension with consecutive rounds of trituration with fire polished glass Pasteur pipettes with tip diameters of 600, 300 and 150 µm. Resulting cell suspension volume was brought up to 1 ml with Trehalose-HEPES-ACSF containing 3 mg/ml ovomuccoid inhibitor and pipetted through a 40 µm cell strainer (Falcon #352340) into a new microcentrifuge tube. Thereafter, the single cell suspension was centrifuged down at 300 *g* for 5 min at 4 ºC and the supernatant replaced with fresh ice-cold Trehalose-HEPES-ACSF and cell pellet

resuspended. Cells were pelleted again and resuspended in 100 µl of ice-cold Resuspension-ACSF. Cell suspensions were kept on ice while cell densities were quantified with a hemocytometer and final cell densities were verified to be in the range of 300 – 1000 cells/µl. Cell suspension volumes estimated to retrieve ~10 000 single cell transcriptomes were added to the 10x Genomics RT reaction mix and loaded to the 10X Single Cell B chip (10x Genomics #1000074) per manufacturer's protocol. We used the Chromium™ Single Cell 3' GEM, Library & Gel Bead Kit v3 (10x Genomics #1000075) and Chromium i7 Multiplex Kit (#120262) to prepare Illumina sequencing libraries downstream of reverse transcription following manufacturer's protocol applying 11 rounds of cDNA library amplification and 12 rounds of sequencing library amplification applied to 70 ng of cDNA library input to library synthesis.

Sequencing, read-mapping and generation of digital expression data

For mapping sequencing reads to the transcriptome, we assembled a custom pre-mRNA transcriptome reference to capture reads mapping to exons, introns and un-annotated 3' UTRs of select neuronal genes. To this end we modified the genome annotation of the *Mus musculus* Ensemble genome reference release 93 for GRCm38 (mm10) genome build by defining transcript spans as exons. Furthermore, to prevent losing reads due to newly overlapping exonic regions, we removed 294 pseudogenes with little to no exonic read mapping from the genome annotation and reverted 450 genes back to exonic annotation. Finally, for several dozen genes, we observed high levels of read mapping just 3' of annotated gene regions that occasionally spliced to known exons and are therefore likely to be derived from unannotated 3' UTR regions. In order to capture those reads, we manually modified the genome annotation for 18 genes (e.g. Etv1, Glp1r) to include the unannotated 3' regions. The transcriptomic reference was assembled with 10x Genomics Cell Ranger v. 3.0.1 mkref pipeline based on the modified genome annotation file and mm10 genome sequence.

ScRNA-seq sequencing libraries were sequenced on an Illumina HiSeq4000 or NovaSeq6000 sequencers (paired-end 150). Illumina sequencing data were aligned to the custom made pre-mRNA reference transcriptome and digital gene-cell matrices were

generated with 10x Genomics Cell Ranger v.3.0.1 count pipeline with anticipated cell count parameter set at 10 000. Regular scRNA-seq samples generated with 10x Genomics v2 kit yielded an average of 49 331 reads/cell for SFO and 33 247 reads per cell for the OVLT library. Neural activity to cell-type mapping data sets generated by 10x Genomics v3 kit had a mean read depth ranging from 44 628 – 78 429 reads/cell.

Sequencing data pre-processing

For the scRNA-seq data generated with 10x genomics v2, expression data were further filtered to exclude cells with fewer than 1000 or more than 35 000 unique transcripts (potential doublets), as well as cells exhibiting more than 15% of mitochondrial transcripts (stressed cells). In order to eliminate doublets, we excluded cell clusters co-expressing two or more markers for canonical cell classes (Ndrg4 for neurons, Ntsr2 for astrocytes, Ucma for lamina terminalis astrocytes, Slco1c1 for endothelial cells, Fcer1g for microglia, Mag for oligodendrocytes). Finally, we eliminated a low transcript abundance neuronal cluster in SFO datasets (stressed cells emerging in samples requiring long enzymatic digestion times). This yielded an SFO dataset with 7950 cells with a median profiling resolution of 2951/4123 genes per cell for all cells and neurons respectively. The resulting OVLT dataset contained 6161 cells with a median profiling resolution of 1729/3353 genes per cell for cells and neurons respectively.

For the neural activity to cell-type mapping datasets generated with 10x Genomics v3, the data were processed as described above with minor modifications. Expression data were filtered to exclude cells with fewer than 1000 or more than 45 000 unique transcripts, as well as cells exhibiting more than 15% of mitochondrial transcripts. Furthermore, cells co-expressing female specific (Xist) and one or more Y-chromosome derived male specific genes (Ddx3y, Eif2s3y, Gm29650, Kdm5d, Uty) were excluded as potential doublets. This yielded median profiling resolutions ranging from 3046.5/4330.5 to 4826/5925 genes per cell for all cell types and neurons respectively.

Analysis of scRNA-seq data

Transcriptomic cell types were determined by analyzing the scRNA-seq data in R (3.5.1) using Seurat (v.3.0.3.9019) as previously described[26]. Briefly, genes expressed in fewer than 10 cells were discarded from digital expression data. SFO and OVLT data were analyzed separately. Expression data from the 4 physiological conditions in neural activation to cell-type mapping experiments were merged into a single gene expression matrix for SFO and OVLT respectively. Gene expression count data were normalized to 10 000 reads and log transformed $[\ \ln\left(\frac{(gene\ count+1)*10\ 000}{total\ transcript\ count\ per\ cell}\right)\ ]$ which was used for most downstream analyses. In order to identify transcriptomic cell classes, we identified genes with most variable expression across the entire data set while controlling for the relationship between mean expression and dispersion. To determine major cell classes, we identified top 850 differentially expressed genes as largest outliers in the mean expression and dispersion space using the vst method in Seurat::FindVariableFeatures function. In order to identify different neural subtypes, we proceeded with top 200 differentially expressed genes. To reduce the effects of cell health on clustering results, we used linear regression to remove the effects of mitochondrial read fraction from expression data and the resulting residuals for the most variable features were then scaled (mean centered and normalized to std. deviation for each gene). We performed dimensionality reduction with principal component analysis on the scaled gene expression data and used the PC-s accounting for most variance (as determined by the "elbow" in the Scree plot ranging from 15 – 20 PCs for major cell classes and 9-15 PCs for neuronal subtypes) as input to clustering analysis. We compiled the shared nearest neighbor graph and identified transcriptomic clusters by optimizing the graph modularity function with the Louvain algorithm as implemented by Seurat::FindNeighbors and Seurat::FindClusters (resolution parameter ranging from 1.5 – 1.7 for major cell classes and 0.4 – 0.8 for neurons) functions respectively. The results of clustering were visualized in a two dimensional UMAP embedding and gene expression programs defining cell types were identified by Wilcoxon Rank Sum test.

OVLT scRNA-seq datasets contain cells that are present both in and around OVLT. To restrict single cell analysis to neurons that are only present in the OVLT, we identified neuron types and cell type specific genetic programs in the OVLT scRNA-seq dataset as described

above (Extended Data **Fig.** 2d). We determined whether specific neuron types were exclusively present in the OVLT, present both inside and outside OVLT or exclusively outside OVLT based on in situ hybridization data from the Allen Brain Institute (https://mouse.brain-map.org/,[46]). Transcriptomic analysis on cell classes and neuron types (**Fig.** 2, 3) was performed on OVLT datasets excluding neurons that were not anatomically located within the OVLT.

In order to overcome misalignment of transcriptomic neuron types due to physiological state derived transcriptional changes, we used canonical correlation analysis implemented in Seurat[26,27] (Extended Data **Fig.** 5). To this end we log-normalized gene expression data in SFO and OVLT neural activity to cell-type mapping datasets and identified integration anchors based on the top 150 differentially expressed gene sets from the untreated neuronal datasets from SFO and OVLT respectively. Based on the latter, we generated joint batch corrected gene-cell matrices using the Seurat::IntegrateData function separately for SFO neurons and OVLT neurons. We identified the previously described neuron types by carrying out clustering analysis on the batch corrected gene cell matrices as described above enabling us to ascribe immediate early gene induction patterns to distinct neuron types in the SFO and OVLT.

Transcriptional homology between SFO and OVLT cell classes and neuron types was evaluated by Spearman correlation of averaged gene expression data per cell type. Here, we used single cell data generated by the 10x Genomics v2 focusing on the union of top 850 differentially expressed genes from SFO and OVLT for major cell classes (total 1224 genes) and top 200 differentially expressed genes from SFO and OVLT neuron types (total 315 genes). First, we estimated the average expression of the joint genes for each cell type. Next we calculated the cross-correlation matrix based on the average gene expression values between the major SFO and OVLT cell classes as well as neuron types respectively using the Spearman correlation. The correlation coefficients between cell types were visualized in a heatmap using the heatmap.2 function in the R gplots library. The cell types were hierarchically clustered by calculating a Euclidean distance matrix based on the correlation

values using the hclust function in R and hierarchical clustering was performed using the Ward agglomeration method.

Correlation analysis for genetic targeting of state specific neural populations

Genetic markers that show best correlation with c-Fos expression under distinct thirst state were identified by Spearman correlation. To this end, we calculated the average expression of the top 1500 most variable genes in the SFO and OVLT as identified by the vst method implemented in Seurat. We correlated the cell type averaged expression of the most variable genes to either cell averaged c-Fos expression under osmotic or hypovolemic stresses for each structure and ordered the genes in descending order according to their Spearman correlation coefficient yielding a list of marker genes that best correlate with the state specific cFos expression pattern.

RNA-Scope based multicolor *in situ* hybridization

In situ hybridization was performed with RNAscope Multiplex Fluorescent Assay (Advanced Cell Diagnostics, #320850). Fixed frozen brains under sated, water deprived, osmotic, or hypovolemic thirst state from C57BL/6, Pdyn-ires-Cre, or Rxfp1-P2A-Cre animals were prepared following the manufacturer's instructions. Briefly, 20 μm cryosectioned slices were mounted on Superfrost Plus slides (Fischer Scientific, 22-037-246). The tissue sections were pre-treated with Target Retrieval solution and Protease III. In the SFO, gene expression was visualized with Htr7 (#401321), Rxfp1 (#458001), Pdyn (#318771), Rxfp3 (#439381), Cre (#312281) and Fos (#316921) probes. For OVLT, the tissue was probed for Bmp3 (#428461), Rxfp1, Pdyn, Cpne4 (#474721), Cre and Fos probes. Following target probe hybridization, the sections were treated with Hybridize Amp 1-4 and stained with DAPI. The sections were imaged with confocal microscopy and probe labeling was manually quantified from 40x z-stacks.

Statistics

Data were processed and analyzed using either R, Python 3 or Prism 8.2. No statistical methods were used to predetermine sample sizes. Data collection and analysis were not performed blind to the condition of the experiments. The sample sizes and statistically significant effects are reported in each figure/figure legend. The significance threshold was held at $\alpha = 0.05$ ($p>0.05$; * $p < 0.05$, ** $p < 0.01$, *** $p < 0.001$, **** $p < 0.0001$) or color coded as specified in the figure legend.

Data availability

Raw and fully processed scRNA-seq data are available at the NCBI Gene Expression Omnibus (GEO accession no. GSE154048).

Code availability

The MATLAB code used to perform vagal neuron calcium imaging analysis is modified from the CaImAn code at https://github.com/flatironinstitute/CaImAn-MATLAB, and is available at https://github.com/Oka-Lab/Imaging-analysis.

Acknowledgements

We thank the members of the Oka laboratory, D.J. Anderson, M. Thomson, S. Chen, S.D. Liberles, C.S. Zuker for helpful discussion and comments. We thank B. Ho and A. Koranne for maintaining and genotyping animal lines. We thank Jeff Park and Single-Cell Profiling Center (SPEC) in the Beckman Institute at Caltech for technical assistance with single-cell RNA-seq; B. Lowell and M. Krashes for generously sharing Pdyn-Cre mice; L. Luo for a generous gift of TRAP2 mice; T. Zhang, W. Han and I.E. Araujo for technical advice on surgical techniques, L. Luebbert for initial imaging analysis, T. Karigo for technical help, X. Chen and V. Gradinaru for advice on virus development and tissue clearing.

SUPPLEMENTAL INFORMATION

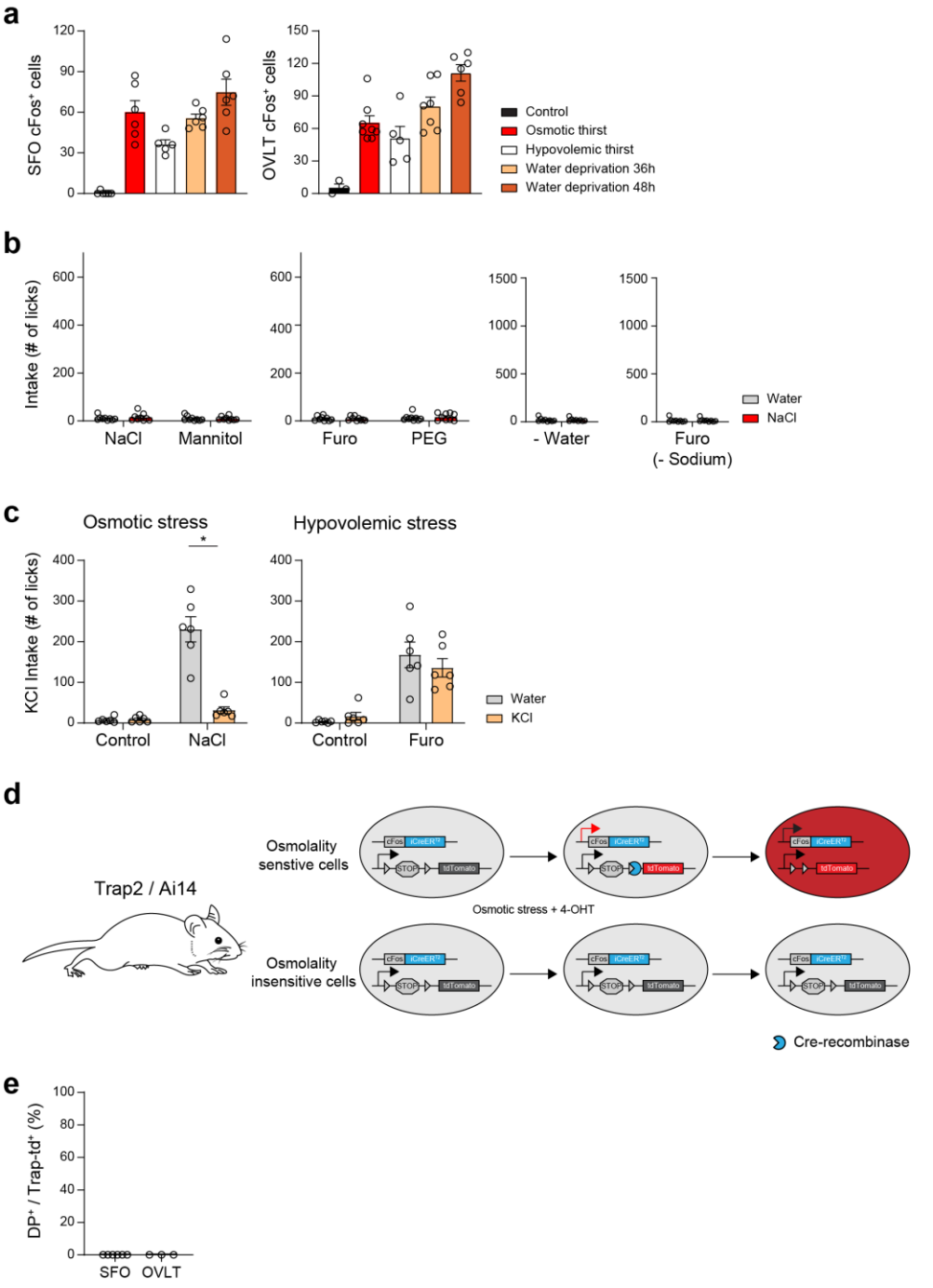

Extended Data Figure 1. Thirst-state-dependent drinking behavior and genetic labeling of active neurons. a, c-Fos expression in the SFO (left) and OVLT (right) under the five

conditions (SFO: n = 6 mice for control, osmotic thirst, water deprivation 36 hours and water deprivation 48 hours, 5 for hypovolemic thirst; OVLT: n = 3 for control, 8 for osmotic thirst, 5 for hypovolemic thirst, 7 for water deprivation 36 hours, 6 for water deprivation 48 hours). **b,** Water and 0.3M NaCl consumption in sated control animals. The number of total licks for water (grey) and 0.3M saline (red) were quantified during a one-hour session (n = 13 for control group, 8 for NaCl, Mannitol, Furo and PEG, and 11 for water deprivation). **c,** Water (grey) and 0.3M KCl intake (orange) under osmotic and hypovolemic thirst states. The number of total licks was quantified during a one-hour session (n = 6 mice). **d,** Experimental diagram for TRAP2 activity-dependent genetic labeling. TRAP2/Ai14 double transgenic animals were challenged with osmotic stress by i.p. injection of NaCl solution in the presence of 4-hydroxytamoxifen (4-OHT). Osmolality sensitive cells (upper) express Cre-ER under the promoter of c-Fos gene, which turns on tdTomato expression (red). In osmolality insensitive cells, the same stimulus does not induce tdTomato expression (bottom). **e**, TRAP labeling in the SFO and OVLT of sated control animals (n = 6 from 3 mice for SFO, n = 3 from 2 mice for OVLT). * $p < 0.05$, ** $p < 0.01$, *** $p < 0.001$by Wilcoxon matched-pairs signed rank test. Data is presented as mean ± s.e.m.

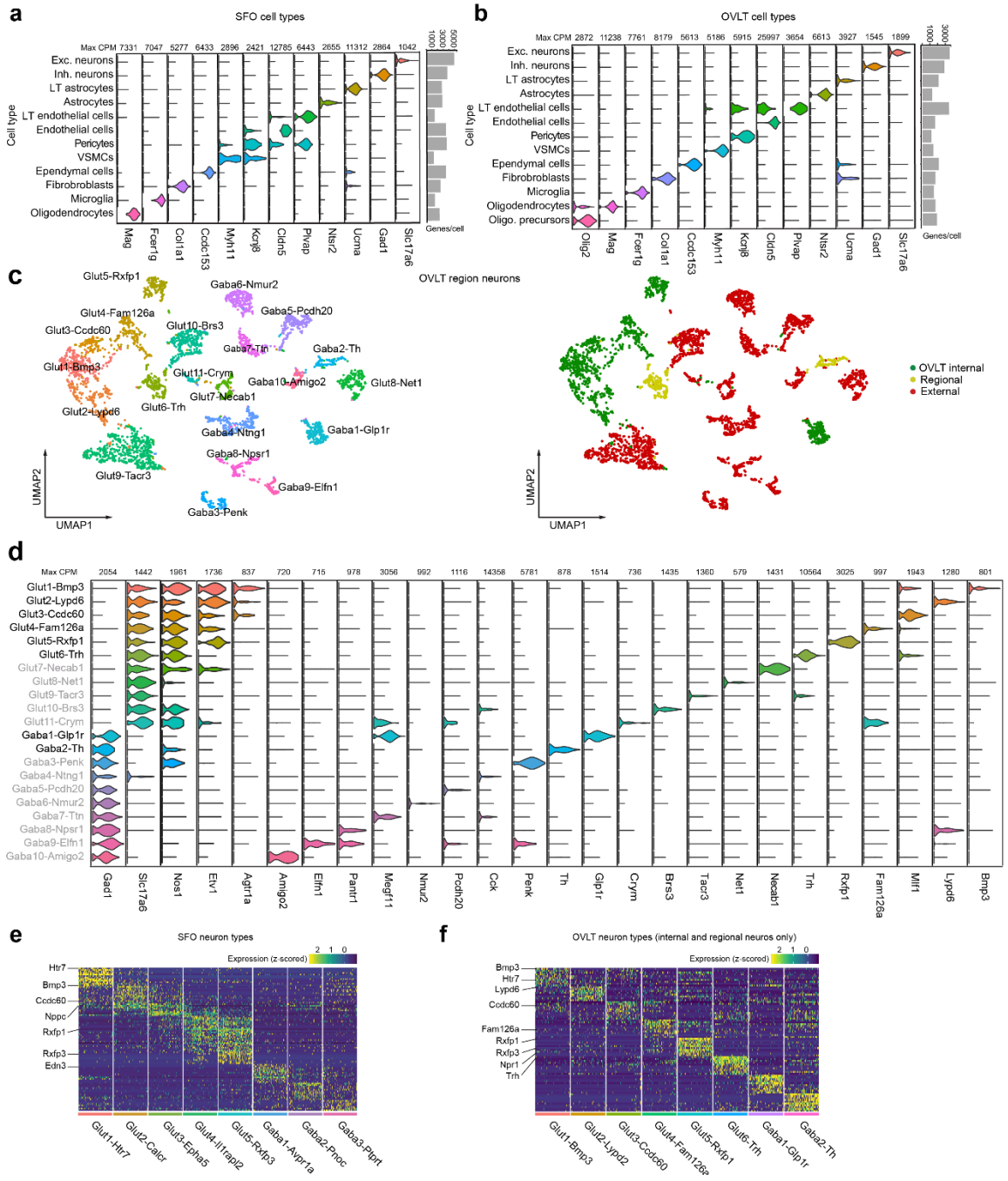

Extended Data Figure 2. Profiling of cell and neuron types in the SFO and OVLT. a and **b,** Violin plot of cell-type-defining genes for SFO (a) and OVLT (b) major cell types. Gene expression level for each gene is shown as maximum counts per million (max CPM). Bar graph shows median profiling resolution per cell type in genes/cell. **c,** Transcriptomic

neuron types in the OVLT region (n = 4109 cells) in a UMAP embedding (left). Based on Allen In Situ Brain Atlas, cell types were annotated into three anatomic classes: inside (green), outside (red), and both inside/outside of the OVLT (yellow). We excluded non-OVLT cell types (red) for further analyses (**Fig.** 2, Extended Data **Fig.** 2e). **d,** Violin plot of genes in all neurons around the OVLT. Neuron types outside the OVLT are shown in gray. **e** and **f,** Heat map of neuron-type-specific gene expression in the SFO (**e**) and OVLT (**f**).

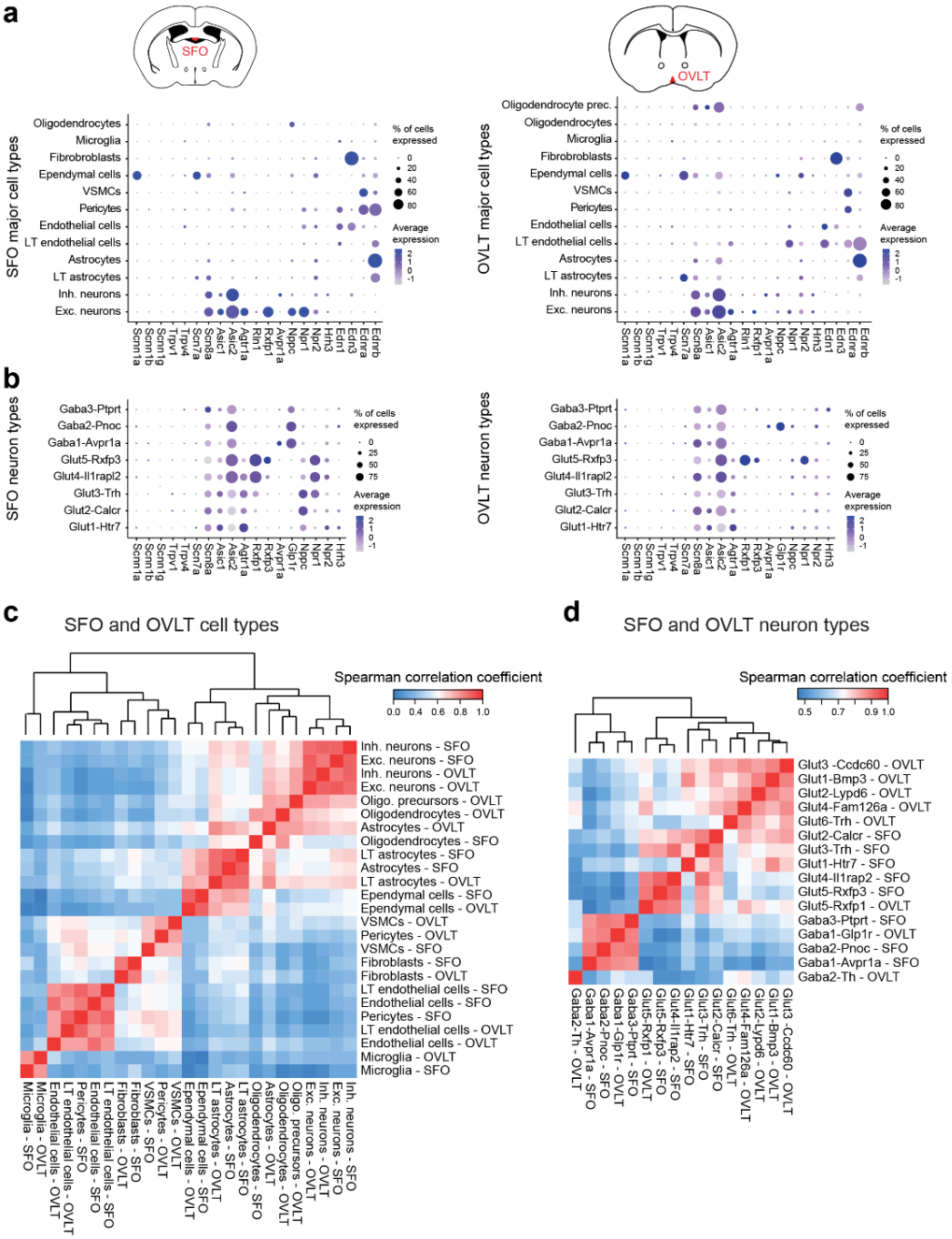

Extended Data Figure 3. Expression of putative osmoregulatory channels/hormone receptors and cellular comparison between the SFO and OVLT. a, Dotplot of cell-type-specific expression for putative osmosensory ion channels and receptor genes for osmoregulatory hormone systems in major cell types in the SFO and OVLT (dot size is

proportional to % of cells with transcript count > 0 expression, color scale represents z-scored average gene expression). **b,** Dotplot of neuron-type-specific expression for putative osmosensory ion channels and receptor genes for osmoregulatory hormone systems in neuron types in the SFO and OVLT[44,47–52]. Although some of the putative genes are not enriched in the SFO or OVLT, they may function outside the LT to regulate thirst. **c,** Evaluation of transcriptional homology between SFO and OVLT cell types based on Spearman correlation between average expression of top 850 most variable genes from the SFO and OVLT, respectively (n = 1224 genes total). Euclidean distance matrix between cell types was calculated based on the Spearman correlation coefficients between cell types, which were then hierarchically clustered using Ward agglomeration. **d,** Same analysis on transcriptional homology between SFO and OVLT neuron types based on top 200 most variable genes from the SFO and OVLT (n = 315 genes total).

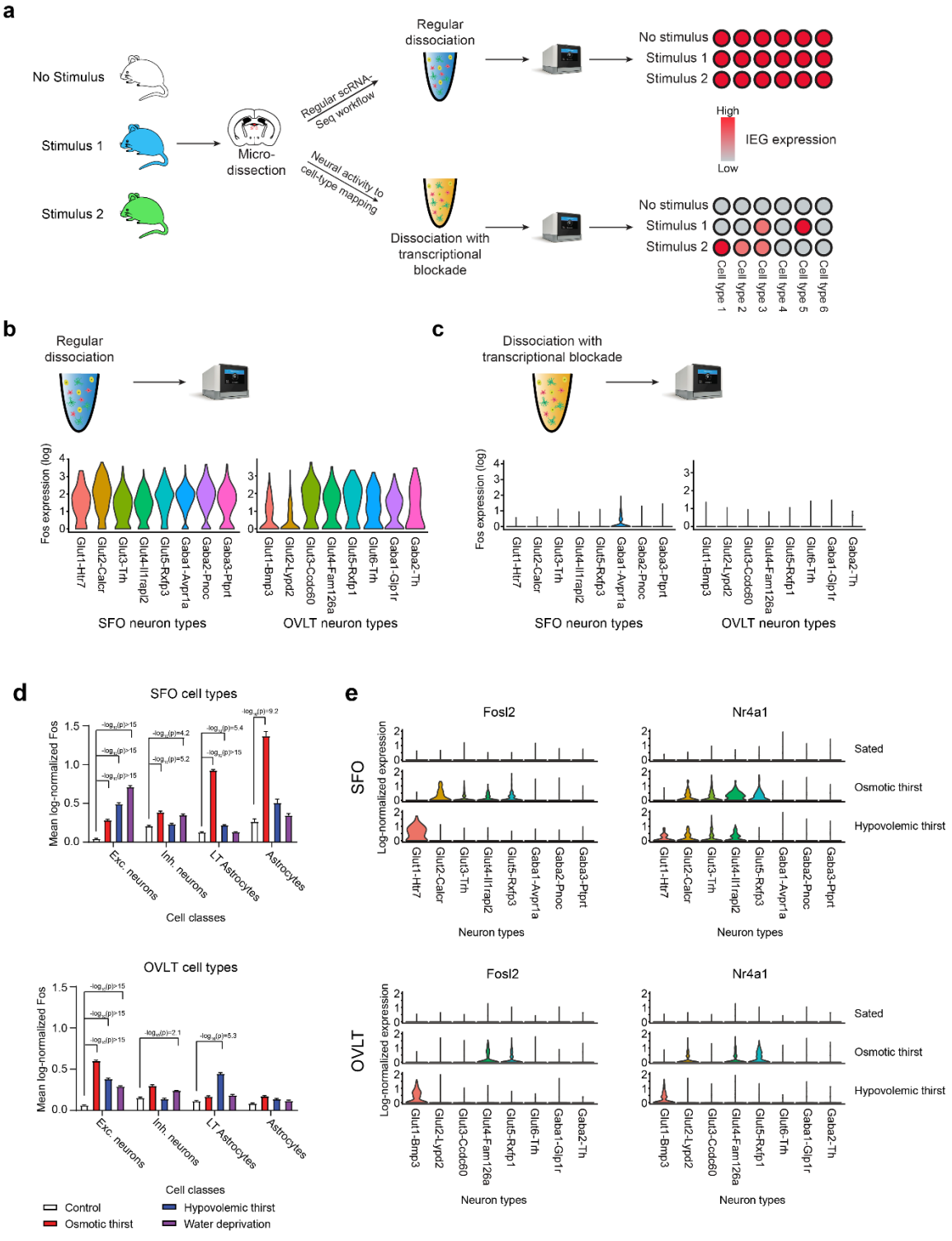

Extended Data Figure 4. Functional cell-type mapping in SFO and OVLT. a, A diagram of scRNA-seq-based stimulus to cell-type mapping protocol. As previously reported, regular

scRNA-seq results in artificial induction of IEGs in all neuron types due to experimental treatments. Performing scRNA-seq with a transcriptional blocker during tissue dissociation suppresses artificial induction of IEGs and allows identification of stimulus-induced IEG expression pattern. **b,** Transcriptional silencing of SFO and OVLT neurons. Regular scRNA-seq induces high levels of c-Fos expression in all SFO and OVLT neuron types (left). Data are shown as a violin plot of log-normalized c-Fos transcript count data. **c,** In the presence of actinomycin D, artificial induction of IEGs in non-stimulated SFO and OVLT neurons is abolished. **d,** Expression of c-Fos in SFO and OVLT major cell classes under distinct thirst states. **e,** Expression of other IEGs (Nr4a1 and Fosl2) in SFO and OVLT neuron types under distinct thirst states. Kruskal-Wallis test with Dunn's post test. P values are shown on a $\log_{10}(p)$ scale.

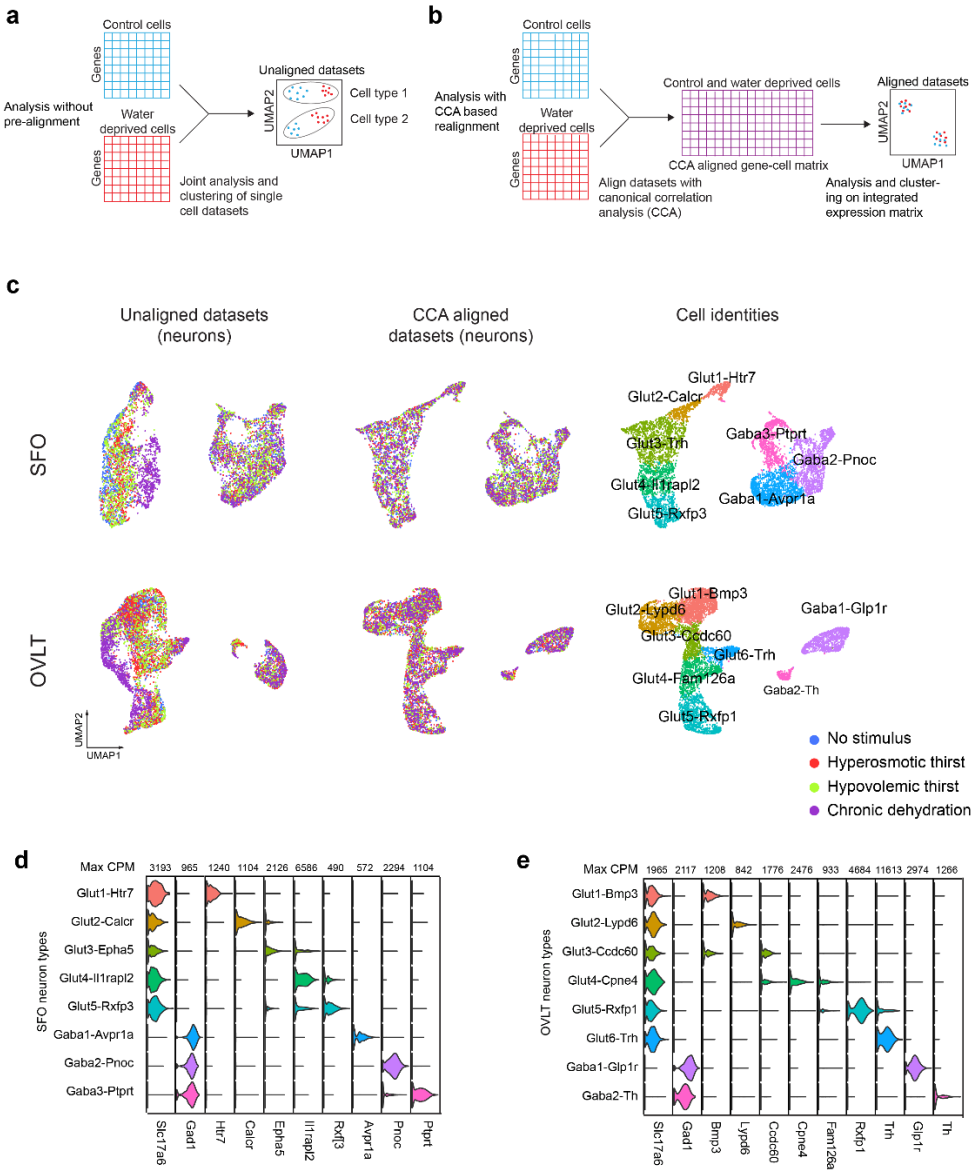

Extended Data Figure 5. Canonical correlation analysis (CCA) based alignment of transcriptomic neuron types under different physiological conditions. a, A misalignment of cell types under distinct physiological states with regular graph-based clustering analysis. **b,** CCA workflow for realigning cell types for joint analysis of transcriptomic datasets. **c,** UMAP embedded scRNA-seq data from SFO and OVLT neurons under distinct thirst status without alignment (left), with CCA alignment (middle) and cell type identification on CCA aligned data (right). **d, e,** Violin plots of cell-type defining marker genes in CCA aligned stimulus to cell-type mapping datasets for SFO and OVLT respectively.

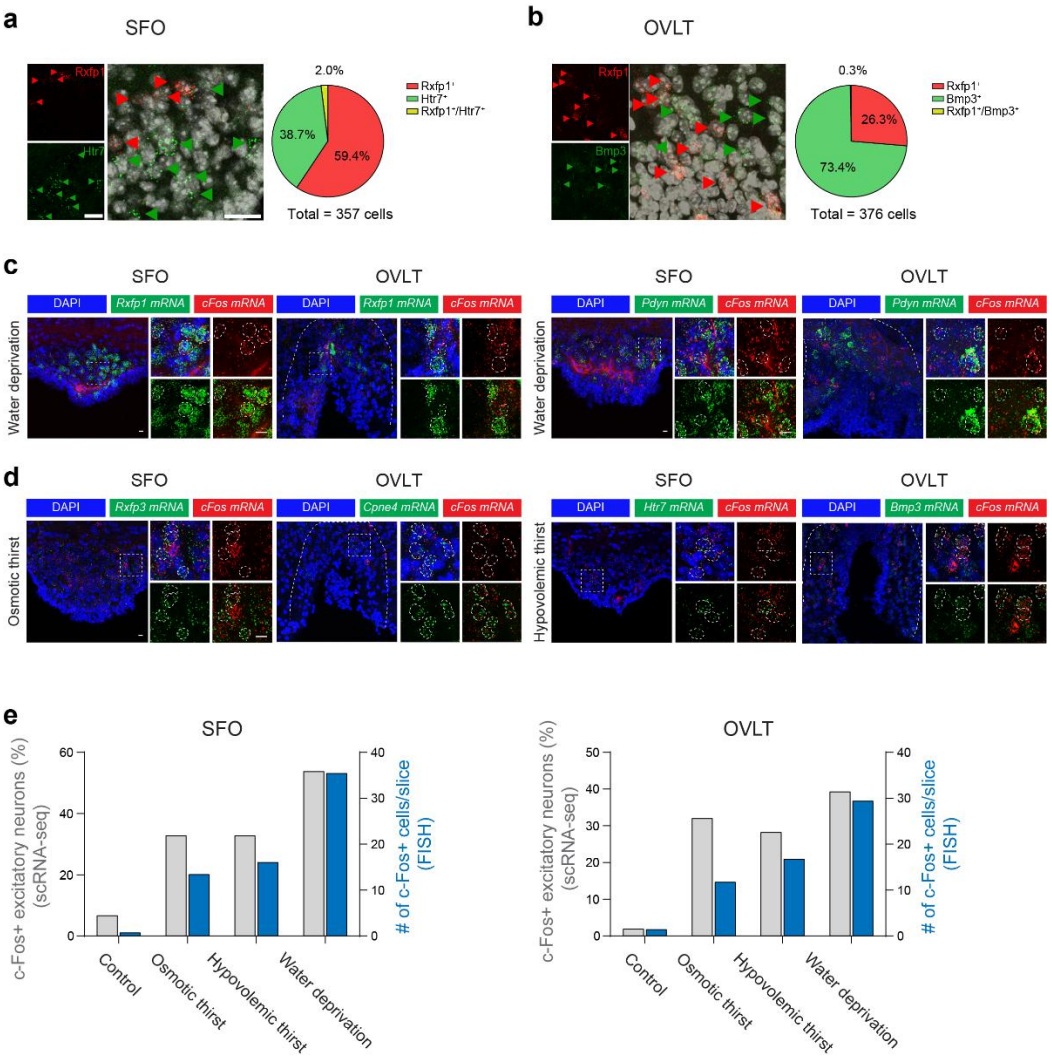

Extended Data Figure 6. Multi-color *in situ* hybridization for anatomical validation of scRNA-Seq cell-types. a, Quantification of SFO Htr7- and Rxfp1-positive cells and their overlap in the SFO (n=12 slices from 4 animals). Scale bar 20 µm. Nuclei are visualized by DAPI staining (white). **b,** Quantification of Bmp3- and Rxfp1-positive cells and their overlap in the OVLT (n=15 slices from 8 animals). **c,** Rxfp1-positive cells in the SFO and OVLT co-express c-Fos under water deprived conditions. Scale bar 10 µm. **d,** Pdyn expressing cells in SFO and OVLT co-express c-Fos under water deprived conditions. **e,** Single cell-types labeled by Rxfp3 (SFO) and Cpne4 (OVLT) express c-Fos under osmotic thirst conditions. **f,** Single cell types labeled by Htr7 (SFO) and Bmp3 (OVLT) express c-Fos under under hypovolemic thirst.

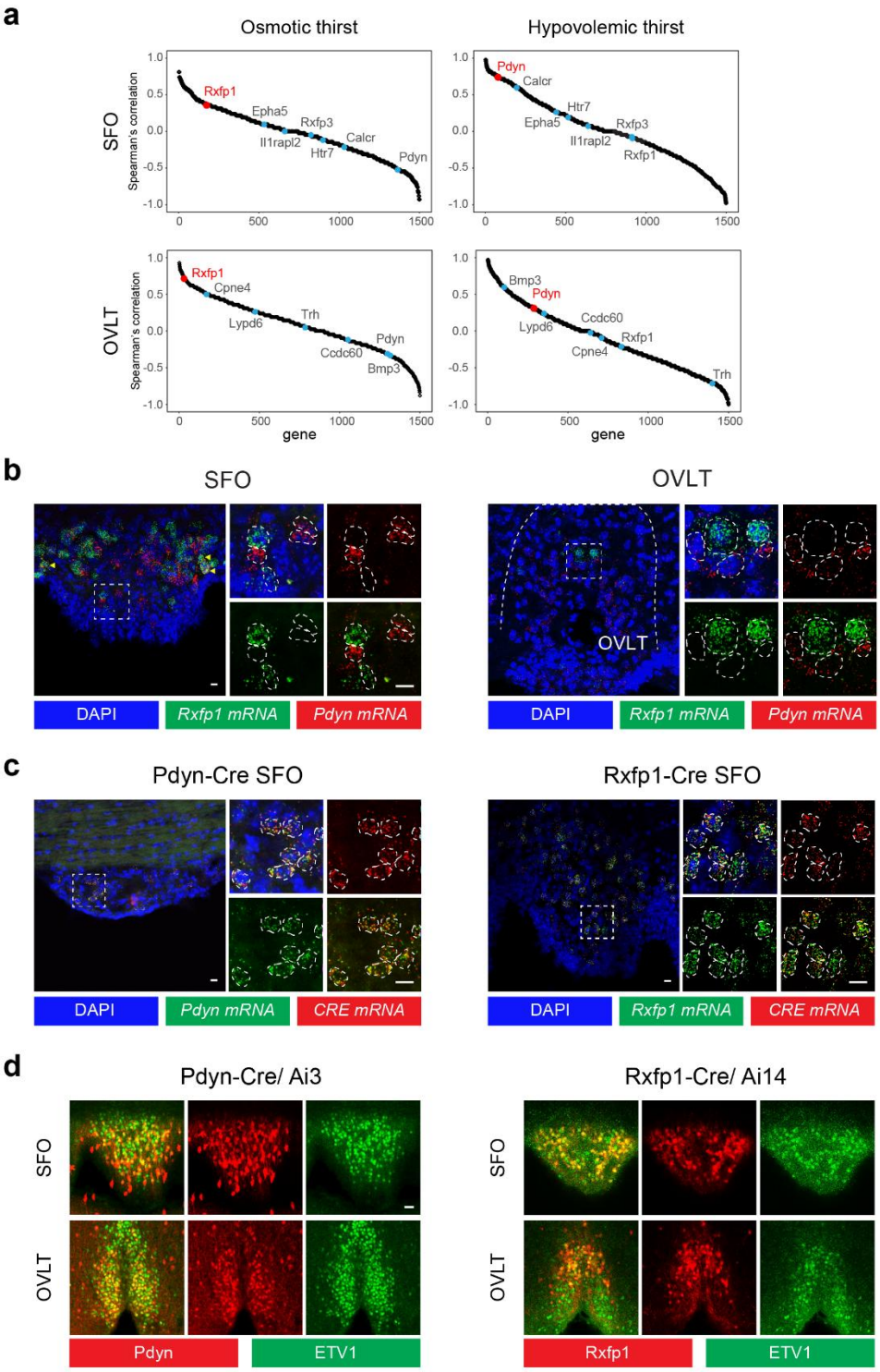

Extended Data Figure 7. Genetic targeting of osmotic and hypovolemic thirst activated cell populations in the SFO and OVLT. a, Spearman correlation between c-Fos expression

under distinct thirst states, excitatory cell type specific markers and marker genes used to target state activated neuron types in the SFO and OVLT. **b,** Two-color *in situ* hybridization of Pdyn and Rxfp1. These gene expression patterns are mostly distinct with minor overlap (arrowhead). **c,** Validation of Cre expression in Pdyn-Cre and Rxfp1-Cre lines (95.5% of Pdyn-Cre and 100% of Rxfp1- Cre expression matched endogenous gene expression, scale bar 10 μm). **d,** Immunostaining of the SFO (top) and OVLT (bottom). Shown are Pdyn-positive neurons in Pdyn-Cre/Ai3 animals (left) and Rxfp1-positive neurons in Rxfp1-Cre/Ai14 animals (right). Pdyn- and Rxfp1-positive neurons (red) are a partial population of ETV1-positive excitatory neurons (green). Almost all (>90%) Pdyn- and Rxfp1-positive neurons expressed ETV1. Rxfp1 and Pdyn data are from **Fig.** 4c (scale bar 10 μm).

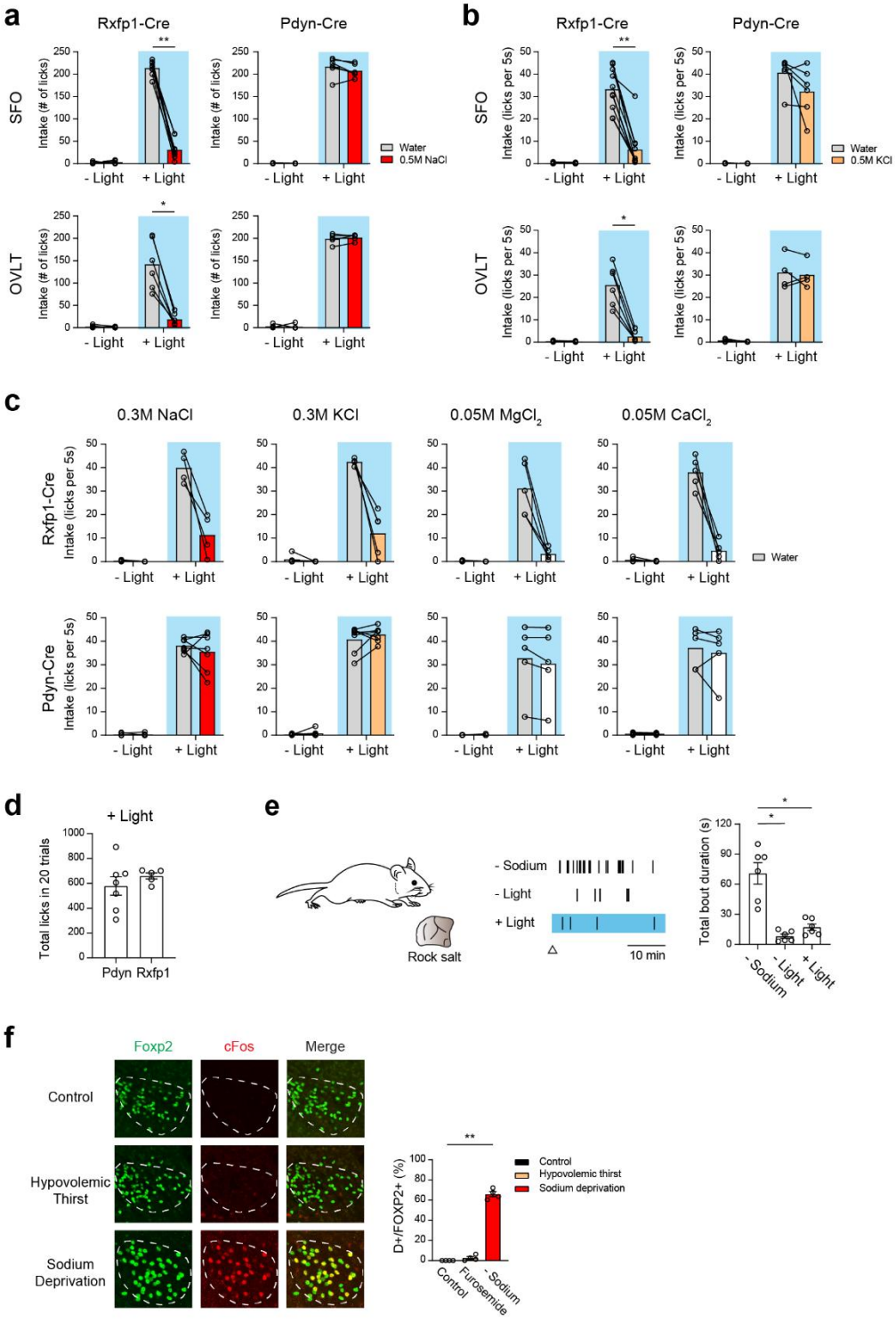

Extended Data Figure 8. Characterization of Rxfp1-Cre and Pdyn-Cre activation derived consumption phenotypes. a, Re-analyzed data of **Fig.** 4c and d that shows total

number of lick during the session. **b,** Photostimulation of SFO^{Rxfp1} neurons triggered robust drinking preference to pure water (middle panel, n = 10 sessions from 5 mice), while photostimulation of SFO^{Pdyn} neurons induced indiscriminate intake of both water and 0.5 M KCl (n = 6 mice). We observed similar preference in OVLT neurons (n = 6 sessions from 3 animals for Rxfp1-Cre, and n = 4 mice for Pdyn-Cre). **c,** Drinking patterns of Rxfp1-Cre and Pdyn-Cre animals to different concentrations and various salts. Photoactivation of SFO^{Rxfp1} induced robust pure water drinking, while the same animal avoided NaCl (0.3 M, n = 4 mice), KCl (0.3 M, n = 5 mice), $MgCl_2$ (0.05 M, n = 5) and $CaCl_2$ (0.05M, n = 5). Animals that receive stimulation in SFO^{Pdyn} neurons accepted all of the above solutions (n = 7 mice for NaCl and KCl, 5 mice for $MgCl_2$ and $CaCl_2$). **d,** Photostimulation of SFO^{Pdyn} and SFO^{Rxfp1} neurons triggered comparable total fluid intake (n = 7 mice for SFO^{Pdyn}, n = 5 mice for SFO^{Rxfp1}). The total lick number of 20 trials was quantified. **e,** Photostimulation of SFO^{Pdyn} neurons did not drive sodium-licking behavior (n = 6 animals). Schematic of rock salt behavior test (left). Representative raster plots under sodium deprivation (-Sodium), sated (-Light) and photostimulation (+ Light) are presented (middle). Triangle marks the start time of recording. The total bout duration is quantified (right). **f,** Hypovolemic stress failed to activate sodium appetite neurons in Pre-LC. Representative images of c-Fos (red) and Foxp2 expression (a genetic marker for sodium appetite neurons, green) under sated (Control), hypovolemic thirst (Furosemide) and sodium deprived conditions (Sodium deprivation). Quantification shows percentage of activated sodium appetite neurons (double positive / Foxp2 positive neurons, right, n = 4 mice per group). * $p < 0.05$, ** $p < 0.01$, *** $p < 0.001$, **** $p < 0.0001$, by Wilcoxon matched-pairs signed rank test, Mann-Whitney test, Friedman test or Kruskal-Wallis test followed by a Dunn's post test. Data is presented as mean ± s.e.m.

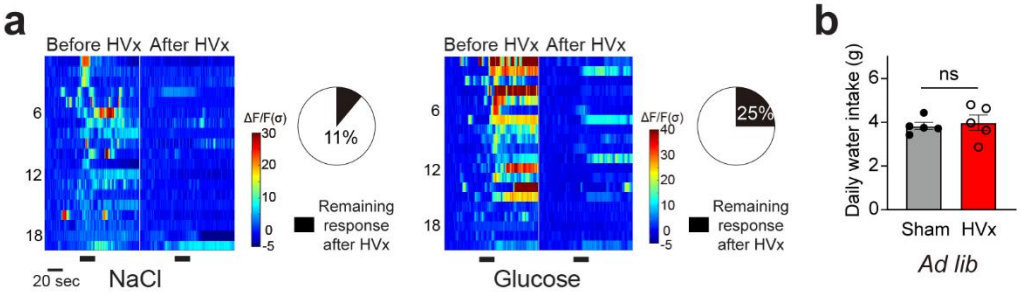

Extended Data Fig. 9. The physiological effects of hepatic vagal branch transection. a, Vagal response heatmaps to 500 mM NaCl or 300 mM glucose stimuli before and after HVx (*Slc17a6-Cre*;Ai96, n = 3 mice). **b,** No change was observed for daily *ad libitum* water intake in sham (grey) and HPA denervation (red) animals (n = 5 mice).

REFERENCES

1.Oatley, K. Changes of Blood Volume and Osmotic Pressure in the Production of Thirst. *Nature* **202**, 1341–1342 (1964).

2.McKinley, M. J. & Johnson, A. K. The physiological regulation of thirst and fluid intake. *News Physiol Sci* **19**, 1–6 (2004).

3.Leib, D. E., Zimmerman, C. A. & Knight, Z. A. Thirst. *Curr Biol* **26**, R1260–R1265 (2016).

4.Bourque, C. W. Central mechanisms of osmosensation and systemic osmoregulation. *Nat Rev Neurosci* **9**, 519–531 (2008).

5.Zimmerman, C. A., Leib, D. E. & Knight, Z. A. Neural circuits underlying thirst and fluid homeostasis. *Nat Rev Neurosci* **18**, 459–469 (2017).

6.Augustine, V., Lee, S. & Oka, Y. Neural Control and Modulation of Thirst, Sodium Appetite, and Hunger. *Cell* **180**, 25–32 (2020).

7.Browning, K. N., Verheijden, S. & Boeckxstaens, G. E. The Vagus Nerve in Appetite Regulation, Mood, and Intestinal Inflammation. *Gastroenterology* **152**, 730–744 (2017).

8.Kim, K.-S., Seeley, R. J. & Sandoval, D. A. Signalling from the periphery to the brain that regulates energy homeostasis. *Nat Rev Neurosci* **19**, 185–196 (2018).

9.Andermann, M. L. & Lowell, B. B. Toward a Wiring Diagram Understanding of Appetite Control. *Neuron* **95**, 757–778 (2017).

10.McKinley, M. J. *et al.* The sensory circumventricular organs of the mammalian brain. *Adv Anat Embryol Cell Biol* **172**, III–XII, 1–122, back cover (2003).

11.Oka, Y., Ye, M. & Zuker, C. S. Thirst driving and suppressing signals encoded by distinct neural populations in the brain. *Nature* **520**, 349–352 (2015).

12.Augustine, V. *et al.* Hierarchical neural architecture underlying thirst regulation. *Nature* **555**, 204–209 (2018).

13.Leib, D. E. *et al.* The Forebrain Thirst Circuit Drives Drinking through Negative Reinforcement. *Neuron* **96**, 1272-1281.e4 (2017).

14.Stricker, E. M. Osmoregulation and volume regulation in rats: inhibition of hypovolemic thirst by water. *Am J Physiol* **217**, 98–105 (1969).

15.Thrasher, T. N., Nistal-Herrera, J. F., Keil, L. C. & Ramsay, D. J. Satiety and inhibition of vasopressin secretion after drinking in dehydrated dogs. *Am J Physiol* **240**, E394-401 (1981).

16.Zimmerman, C. A. *et al.* A gut-to-brain signal of fluid osmolarity controls thirst satiation. *Nature* **568**, 98–102 (2019).

17.Augustine, V. *et al.* Temporally and Spatially Distinct Thirst Satiation Signals. *Neuron* **103**, 242-249.e4 (2019).

18.Lechner, S. G. *et al.* The molecular and cellular identity of peripheral osmoreceptors. *Neuron* **69**, 332–344 (2011).

19.Brierley, S. M. *et al.* Selective role for TRPV4 ion channels in visceral sensory pathways. *Gastroenterology* **134**, 2059–2069 (2008).

20.Zimmer, L. J., Meliza, L. & Hsiao, S. Effects of cervical and subdiaphragmatic vagotomy on osmotic and volemic thirst. *Physiol Behav* **16**, 665–670 (1976).

21.Smith, G. P. & Jerome, C. Effects of total and selective abdominal vagotomies on water intake in rats. *J Auton Nerv Syst* **9**, 259–271 (1983).

22.Kim, D.-Y. *et al.* A neural circuit mechanism for mechanosensory feedback control of ingestion. *Nature* **580**, 376–380 (2020).

23.Allen, W. E. *et al.* Thirst-associated preoptic neurons encode an aversive motivational drive. *Science* **357**, 1149–1155 (2017).

24.Johnson, A. K. & Gross, P. M. Sensory circumventricular organs and brain homeostatic pathways. *FASEB J* **7**, 678–686 (1993).

25.Johnson, A. K., Zardetto-Smith, A. M. & Edwards, G. L. Integrative mechanisms and the maintenance of cardiovascular and body fluid homeostasis: the central processing of sensory input derived from the circumventricular organs of the lamina terminalis. *Prog Brain Res* **91**, 381–393 (1992).

26.Butler, A., Hoffman, P., Smibert, P., Papalexi, E. & Satija, R. Integrating single-cell transcriptomic data across different conditions, technologies, and species. *Nat Biotechnol* **36**, 411–420 (2018).

27.Stuart, T. *et al.* Comprehensive Integration of Single-Cell Data. *Cell* **177**, 1888-1902.e21 (2019).

28.Benz, F. *et al.* Low wnt/β-catenin signaling determines leaky vessels in the subfornical organ and affects water homeostasis in mice. *Elife* **8**, e43818 (2019).

29.Bourque, C. W., Oliet, S. H. & Richard, D. Osmoreceptors, osmoreception, and osmoregulation. *Front Neuroendocrinol* **15**, 231–274 (1994).

30.Sharif-Naeini, R., Ciura, S., Zhang, Z. & Bourque, C. W. Contribution of TRPV channels to osmosensory transduction, thirst, and vasopressin release. *Kidney Int* **73**, 811–815 (2008).

31.Wu, Y. E., Pan, L., Zuo, Y., Li, X. & Hong, W. Detecting Activated Cell Populations Using Single-Cell RNA-Seq. *Neuron* **96**, 313-329.e6 (2017).

32.Hrvatin, S. *et al.* Single-cell analysis of experience-dependent transcriptomic states in the mouse visual cortex. *Nat Neurosci* **21**, 120–129 (2018).

33.Betley, J. N. *et al.* Neurons for hunger and thirst transmit a negative-valence teaching signal. *Nature* **521**, 180–185 (2015).

34.Campbell, J. N. *et al.* A molecular census of arcuate hypothalamus and median eminence cell types. *Nat Neurosci* **20**, 484–496 (2017).

35.Moffitt, J. R. *et al.* Molecular, spatial, and functional single-cell profiling of the hypothalamic preoptic region. *Science* **362**, eaau5324 (2018).

36.Geerling, J. C. & Loewy, A. D. Central regulation of sodium appetite. *Exp Physiol* **93**, 177–209 (2008).

37.Lee, S. *et al.* Chemosensory modulation of neural circuits for sodium appetite. *Nature* **568**, 93–97 (2019).

38.Williams, E. K. *et al.* Sensory Neurons that Detect Stretch and Nutrients in the Digestive System. *Cell* **166**, 209–221 (2016).

39.Tan, H.-E. *et al.* The gut-brain axis mediates sugar preference. *Nature* **580**, 511–516 (2020).

40.Adachi, A., Niijima, A. & Jacobs, H. L. An hepatic osmoreceptor mechanism in the rat: electrophysiological and behavioral studies. *Am J Physiol* **231**, 1043–1049 (1976).

41.Baertschi, A. J. & Vallet, P. G. Osmosensitivity of the hepatic portal vein area and vasopressin release in rats. *J Physiol* **315**, 217–230 (1981).

42.Niijima, A. Glucose-sensitive afferent nerve fibres in the hepatic branch of the vagus nerve in the guinea-pig. *J Physiol* **332**, 315–323 (1982).

43.Morita, H., Fujiki, N., Hagiike, M., Yamaguchi, O. & Lee, K. Functional evidence for involvement of bumetanide-sensitive Na+K+2CI- cotransport in the hepatoportal Na+ receptor of the Sprague-Dawley rat. *Neurosci Lett* **264**, 65–68 (1999).

44.Hiyama, T. Y., Watanabe, E., Okado, H. & Noda, M. The subfornical organ is the primary locus of sodium-level sensing by Na(x) sodium channels for the control of salt-intake behavior. *J Neurosci* **24**, 9276–9281 (2004).

45.Kennedy, A. *et al.* Stimulus-specific hypothalamic encoding of a persistent defensive state. *Nature* **586**, 730–734 (2020).

46.Watanabe, E. *et al.* Nav2/NaG channel is involved in control of salt-intake behavior in the CNS. *J Neurosci* **20**, 7743–7751 (2000).

47.Lein, E. S. *et al.* Genome-wide atlas of gene expression in the adult mouse brain. *Nature* **445**, 168–176 (2007).

48.Antunes-Rodrigues, J., McCann, S. M., Rogers, L. C. & Samson, W. K. Atrial natriuretic factor inhibits dehydration- and angiotensin II-induced water intake in the conscious, unrestrained rat. *Proc Natl Acad Sci U S A* **82**, 8720–8723 (1985).

49.Ciura, S. & Bourque, C. W. Transient receptor potential vanilloid 1 is required for intrinsic osmoreception in organum vasculosum lamina terminalis neurons and for normal thirst responses to systemic hyperosmolality. *J Neurosci* **26**, 9069–9075 (2006).

50.Gizowski, C., Zaelzer, C. & Bourque, C. W. Clock-driven vasopressin neurotransmission mediates anticipatory thirst prior to sleep. *Nature* **537**, 685–688 (2016).

51.Kinsman, B. *et al.* Osmoregulatory thirst in mice lacking the transient receptor potential vanilloid type 1 (TRPV1) and/or type 4 (TRPV4) receptor. *Am J Physiol Regul Integr Comp Physiol* **307**, R1092-1100 (2014).

52.Liedtke, W. & Friedman, J. M. Abnormal osmotic regulation in trpv4-/- mice. *Proc Natl Acad Sci U S A* **100**, 13698–13703 (2003).

Chapter 3

ORGAN-SPECIFIC SYMPATHETIC REGULATION OF VISCERAL FUNCTIONS

SUMMARY

The autonomic nervous system orchestrates the brain and body functions through the sympathetic and parasympathetic pathways. However, our understanding of the autonomic system, especially the sympathetic system, at the cellular and molecular levels is severely limited. In this chapter, I summarize the anatomical architecture of the descending autonomic system, providing a foundation for understanding its structural complexity. Then I show unique topological representations of individual visceral organs in the major abdominal sympathetic ganglion complex, celiac-superior mesenteric ganglia (CG-SMG). Using multi-modal transcriptomic analyses, we identified molecularly distinct sympathetic populations. Notably, individual CG-SMG populations exhibit selective and mutually exclusive axonal projections to visceral organs, targeting either the gastrointestinal (GI) tract or secretory areas including the pancreas and bile tract. This combinatorial innervation pattern suggests functional segregation between different CG-SMG populations. Indeed, our neural perturbation experiments demonstrated that one class of neurons regulates GI transit. Another class of neurons controls digestion and glucagon secretion independent of gut motility. These results reveal the molecularly diverse sympathetic system and suggest modular regulations of visceral organ functions by sympathetic populations.

Wang, T., et al. (2025). “Molecular and functional diversity of the autonomic nervous system”. In: *Nature Reviews Neuroscience* 26(10), pp. 607–622. doi: 10.1038/s41583-025-00941-2.

Wang, T., et al. (2025). “Organ-specific sympathetic innervation defines visceral functions”. In: *Nature* 637(8047), pp. 895–902. doi: 10.1038/s41586-024-08269-0.

INTRODUCTION

Whether confronting a predator or anticipating a feast, the brain communicates with the body through the autonomic nervous system (ANS) to prepare for the appropriate physiological response[1]. For example, in a state of hunger, the brain sends signals to the pancreas to release glucagon that elevates the blood glucose level[2,3]. Following food consumption, the brain detects incoming nutrients and enhances intestinal motility and digestive enzyme secretion to facilitate energy replenishment[4,5]. These physiological responses often precede measurable internal state changes, ensuring swift and efficient adaptation[6,7].

Over the past decade, significant progress has been made in understanding body-brain communications, particularly focused on the roles of vagal and spinal afferent neurons. These advances have been reviewed in recent literature[8–12]. In contrast, autonomic motor neurons remain relatively underexplored partly due to the anatomical complexity and technical challenges that limit functional analysis in awake states[13].

The ANS is classically divided into three branches: the sympathetic, parasympathetic and enteric nervous systems[14–16]. This thesis focuses on the sympathetic and parasympathetic divisions that serve as primary conduits for brain-body communication. The sympathetic division, which includes both neuronal and adrenal gland components, orchestrates broad, emergent responses such as increased heart rate and vasoconstriction, often associated with "fight or flight" situations[17–19]. Under relaxed conditions, the parasympathetic branch promotes "rest and digest" functions, counteracting sympathetic activity[20]. While this dichotomous framework offers a useful conceptual model, it fails to capture the cellular and functional heterogeneity inherent within the ANS[21,22]. Advances in genetic tools have revealed a remarkable diversity of autonomic motor neuron types, each defined by unique gene expression profiles[23–28]. A few recent studies identified genetically distinct parasympathetic pathways to cardiovascular[3] and gastrointestinal[18] areas, while the sympathetic division remains largely unknown.

ANATOMICAL ARCHITECTURE OF DESCENDING AUTONOMIC PATHWAYS

General anatomical structure

Autonomic signals are transmitted to the body through preganglionic neurons located in the brainstem or spinal cord, and postganglionic neurons in the periphery[40]. A representative ANS structure based on human and rodent data is shown (**Fig. 1a**). The sympathetic and parasympathetic divisions of the ANS exhibit significant anatomical and molecular differences[15,41]. In the sympathetic system, preganglionic neurons are situated in the spinal cord and project to postganglionic neurons in sympathetic ganglia or to chromaffin cells in the adrenal medulla[42]. These ganglia include the paravertebral chain, which runs alongside the vertebral column in a topographical arrangement, and the prevertebral ganglia, located closer to the target organs. In contrast, parasympathetic preganglionic neurons are found in the brainstem or the sacral spinal cord[43]. Their axons travel through cranial nerves, particularly the vagus nerve, or via the pelvic splanchnic nerves to reach ganglia situated near or within their target organs.

Another key distinction between the two divisions lies in their neurotransmitters (**Fig. 1b**)[44]. In the sympathetic system, preganglionic neurons release acetylcholine to activate postganglionic neurons. These postganglionic neurons in turn release norepinephrine and other molecules (e.g., neuropeptide Y: NPY) to modulate target organs[45–47], although a few exceptions were reported[48,49]. In contrast, both preganglionic and postganglionic neurons in the parasympathetic system use primarily acetylcholine for synaptic transmission. These distinct signaling mechanisms have historically been used to identify autonomic neurons, based on molecules involved in neurotransmitter synthesis, release, and reuptake[50].

Sympathetic adrenergic and noradrenergic neurons are characterized by the expression of tyrosine hydroxylase (TH) and dopamine β-hydroxylase (DBH), enzymes essential for norepinephrine synthesis[51,52]. In adrenal chromaffin cells, phenylethanolamine N-methyltransferase (PNMT) further converts norepinephrine to epinephrine, also known as adrenaline[53–55]. The vesicular monoamine transporter 2 (VMAT2, encoded by

the *Slc18a2* gene) packages monoamines such as norepinephrine into synaptic vesicles[56,57], while the norepinephrine transporter (NET, encoded by *Slc6a2*) facilitates norepinephrine reuptake into presynaptic terminals[58,59]. Parasympathetic neurons, on the other hand, express choline acetyltransferase (ChAT) and utilize the high-affinity choline transporter (ChT, encoded by *Slc5a7*) to uptake choline for acetylcholine synthesis[60,61]. The vesicular acetylcholine transporter (VAChT, encoded by *Slc18a3*) transports acetylcholine into secretory vesicles for release[62,63].

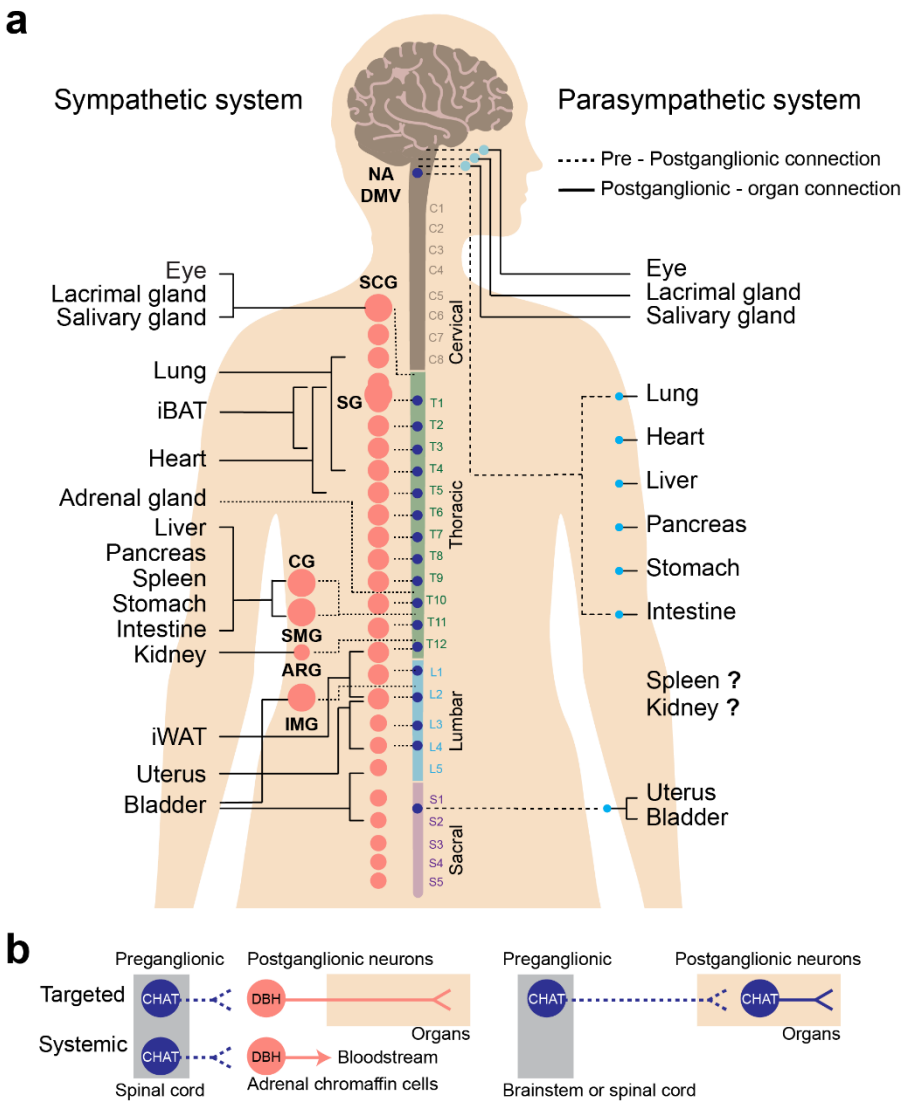

Fig. 1 Brain-to-body autonomic pathways. a, An anatomical scheme for the autonomic signals from the central nervous system to the peripheral organs, which contains

sympathetic (left) and parasympathetic (right) pathways. The innervation is organized in a two-relay manner: preganglionic to postganglionic connection (dashed line), and postganglionic to organ projection (solid line). **b,** In the sympathetic system (left), preganglionic neurons release acetylcholine to activate either postganglionic neurons that mediate targeted organ responses, or the adrenal chromaffin cells which produce systemic effects. By contrast, the parasympathetic preganglionic and postganglionic neurons (found in brainstem or spinal cord) both use acetylcholine for synaptic transmission (right). ARG, aorticorenal ganglion; CG, coeliac ganglion; ChAT, choline acetyltransferase; DBH, dopamine β-hydroxylase; DMV, dorsal motor nucleus of the vagus; iBAT, interscapular brown adipose tissue; IMG, inferior mesenteric ganglion; iWAT, inguinal white adipose tissue; NAm, nucleus ambiguous; SCG, superior cervical ganglion; SG, stellate ganglion; SMG, superior mesenteric ganglion.

These canonical markers have been widely utilized in histological analyses to distinguish sympathetic and parasympathetic innervation across species. However, cholinergic and noradrenergic markers are not always mutually exclusive in some ganglia such as the pelvic ganglion[64–66]. Additionally, these markers are not entirely specific to autonomic motor neurons, as other peripheral neurons can also exhibit noradrenergic or cholinergic properties. For instance, TH is expressed in some visceral sensory neurons[67,68], leading to the labeling of both sensory afferents and sympathetic efferents in the same tissue. Further, spinal sensory neurons traverse sympathetic ganglia enroute to various tissue beds, adding another layer of complexity[21]. Therefore, accurately mapping autonomic innervation requires combining marker expression with anatomical tracing techniques to confirm the origin of neurons from autonomic ganglia.

Mapping autonomic innervation

Tracing experiments with synthetic dyes or viral vectors have been widely used to study anatomical projections of autonomic motor neurons (**Fig. 1a**). While general organizational

principles of autonomic innervation appear conserved across species, the specific patterns vary depending on the animal model studied. For instance, noradrenergic fibers were detected within the liver parenchyma of a wide range of species, but were absent in mice and rats[69]. Sympathetic preganglionic neurons that project to the adrenal gland span a comparable range of spinal cord segments across species, yet the segment containing the peak number of projecting neurons differs between models[70].

In the sympathetic chain, the superior cervical ganglion (SCG) typically targets axial organs of the head and neck such as eyes, lacrimal glands and salivary glands[71–73]. The stellate ganglion (SG) innervates the heart, lungs and interscapular brown adipose tissue (iBAT)[26,74–76]. The celiac-superior mesenteric ganglia (CG-SMG) project to most abdominal organs including the gastrointestinal (GI) tract, biliary system, pancreas, and spleen[77–80]. The inferior mesenteric ganglion (IMG) innervates the large intestine and urinary bladder[81,82], and the aorticorenal ganglion (ARG) sends axons to the kidney[83]. The liver and kidney receive separate sympathetic inputs from the CG-SMG and ARG, respectively, despite the physical proximity[84]. Retrograde tracing has identified several thoracic sympathetic ganglia as sources of innervation to region-specific adipose tissue[85,86], as well as reproductive organs such as the uterus[87,88], but the targets of many other chain ganglia remain poorly characterized due to limited anatomical accessibility. Adding further but important complexity, axons from various tissues can be traced retrograde to specific regions of ganglia, for example, the craniomedial pole of the stellate ganglion houses cardiac and pulmonary neurons[26,74,75]. Anterograde tracing studies, primarily conducted in larger animals, have mostly confirmed the above findings[89–91].

In the parasympathetic branch, the cranial nerve III (oculomotor) innervates the eye[92]. The cranial nerve VII (facial) supplies lacrimal and salivary glands[93–95], while the cranial nerve IX (glossopharyngeal) targets parotid glands and the stylopharyngeus muscle[96]. Vagal efferent fibers arise from two major sources within the brainstem: the nucleus ambiguus (NA) and the dorsal motor nucleus of the vagus (DMV)[97–100]. NA neurons project to the thoracic organs, including the heart and lungs[24]. DMV neurons primarily innervate

abdominal organs[23,101,102] with minor projections to thoracic areas[103–109]. Pelvic splanchnic nerves carry parasympathetic fibers from the spinal cord to the urinary bladder, reproductive organs, and to a lesser degree to the distal colon[110–112]. Parasympathetic input to the kidney, spleen and adrenal gland remain controversial and require further investigation[70,113–118].

In target organs, autonomic postganglionic neurons innervate multiple tissue types, mainly smooth muscle, cardiac muscle, and glandular tissues[20,21]. Sympathetic postganglionic neurons regulate smooth muscle contraction in blood vessels and airways[49,71,119], enhance cardiac output by acting on cardiac muscle[17,120], and modulate secretion in glands such as salivary and sweat glands[121–123]. Parasympathetic postganglionic neurons predominantly promote smooth muscle relaxation[124,125], stimulate glandular secretion in the lacrimal and digestive glands[73,94,123], and decrease heart rate[24,120,126]. Beyond these canonical targets, autonomic fibers also influence adipose tissue metabolism[3,30,30,127], immune cell activity[32,72,128], and stem cell niche homeostasis[36,129,130], reflecting the expansive and multifaceted reach of autonomic output in the periphery.

New molecular and anatomical tools such as tissue clearing have enabled the characterization of high-resolution three-dimensional autonomic innervation patterns. For instance, genetically labeled TH or CHAT neurons have been visualized in a whole-mount preparation[52,84,131–133], and intersectional genetics have enhanced the specificity of neural and axonal labeling[134,135]. These approaches are paving the way for a more comprehensive understanding of the spatial complexity of autonomic innervation.

CONNECTIVITY MAPPING BETWEEN THE GANGLION AND ORGANS

Although the anatomy of the sympathetic system has been well-described[19–22], its molecular and functional organization remains largely unknown. The lack of basic understanding poses a challenge in developing targeted therapeutic interventions for autonomic disorders such as irritable bowel syndrome and gastroparesis[23]. The current treatments still largely rely on non-specific modulation of neurotransmitters identified over a century ago. Here, I applied transcriptomics, organ mapping, and cell-type-specific functional perturbation to the major visceral sympathetic ganglia, CG-SMG. Our results demonstrate that distinct sympathetic neuron types innervate unique combinations of visceral organs to regulate GI transit and secretory functions.

Peripheral organs receive sympathetic inputs from pre- and para-vertebral ganglia organized in a topological manner known as the sympathetic chain[24]. The CG-SMG complex consists of three ganglia (bilateral CG and SMG) that send sympathetic signals to visceral organs[25]. To gain insights into sympathetic regulatory mechanisms, we determined the topological representation of visceral organs in CG-SMG (**Fig.** 1). I performed retrograde tracing using wheat germ agglutinin (WGA) from eight visceral organs: spleen, hepatic portal area (HPA), pancreas, stomach, duodenum, jejunum, ileum, and colon. I developed a computational pipeline to build a standardized CG-SMG atlas for precise ganglia-organ mapping across animals (**Fig.** 1a, Extended Data **Fig.** 1a, b). The reference anatomy was generated from 20 ganglia through unsupervised image alignment processing. Auto-detected WGA signals were then mapped onto the reference image (Extended Data **Fig.** 1c). This analysis revealed unique topological representations of visceral organs on CG-SMG (**Fig.** 1b, Extended Data **Fig.** 2). Neurons that project to the spleen, HPA, pancreas, stomach, and duodenum were predominantly located in lateral CG-SMG. Distal small intestine and large intestine were mainly mapped to medial areas. Our anterograde tracing supported these results (Supplementary **Fig.** 1). I next asked whether different organs receive inputs from the same or different sets of CG-SMG neurons by performing dual-color tracing from paired organ sites. While injection of both WGAs in

the same organ produced mostly overlapping neural labeling, I found minimal overlap of WGA signals derived from two different organs (**Fig.** 1c, Extended Data **Fig.** 2d). These results are consistent with a recent study on the GI tract[26], and further demonstrate that adjacent visceral organs are innervated by separate neurons in proximal areas of CG-SMG.

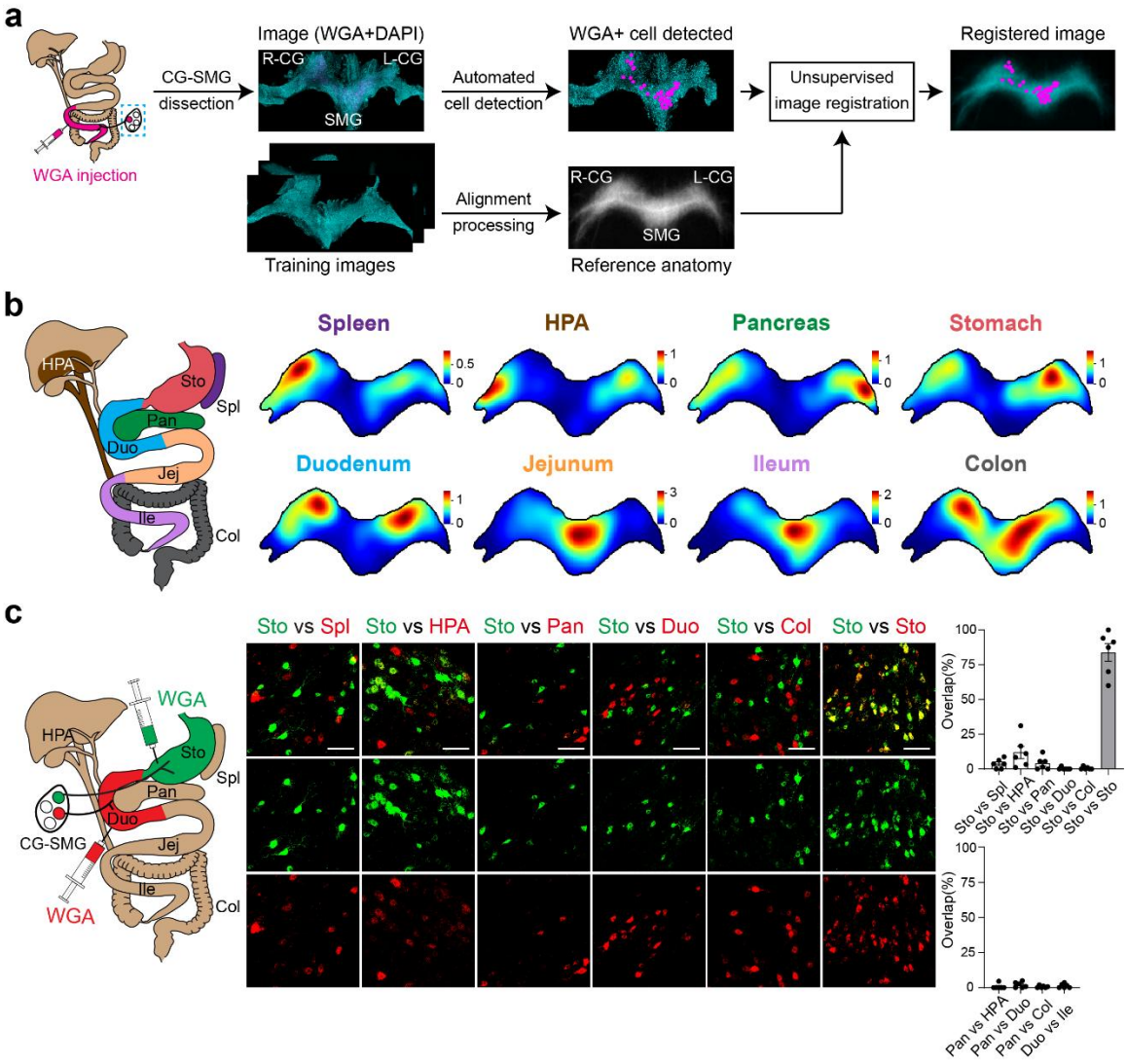

Fig. 1: Topographical representation of visceral organs in CG-SMG sympathetic complex. a, A computational pipeline for organ topographical mapping. WGA was injected in a given visceral organ for retrogradely labeling CG-SMG neurons. WGA-positive cells (magenta) were auto-detected on CG-SMG using DAPI (blue) as a

background shape. R-CG, right CG; L-CG, left CG. For aligning ganglia across animals, 20 training images were used to build a standardized reference image through an unsupervised alignment process. Organ maps (WGA-positive neurons) from each animal were registered to the reference atlas. **b**, Gaussian heatmaps of WGA-positive cells traced from individual visceral organs. Eight organ sites were targeted: the spleen (Spl), hepatic portal area (HPA), pancreas (Pan), stomach (Sto), duodenum (Duo), jejunum (Jej), ileum (Ile), and colon (Col). For each organ site, the average of heatmaps from eight mice is presented. **c,** WGA dual-color tracing experiments of visceral organ pairs. Left: a diagram showing WGA 488 (green) injection to the stomach and WGA 647 (red) injection to the duodenum. Middle: representative CG-SMG images with two-color WGA injections to organs as indicated. Minimal overlap was detected between paired organs. Right: quantification of the overlapped neurons as a percentage of total WGA-positive neurons (n = 6 mice per group). Scale bar, 100 μm. Data are presented as mean ± s.e.m.

MOLECULAR DIVERSITY OF SYMPATHETIC NEURONS

To examine the cellular diversity of CG-SMG neurons, i performed single-cell RNA sequencing (scRNA-seq) from 25k CG-SMG cells. Based on uniquely expressed genes in each cell cluster, I selected 371 genes for spatial transcriptomics experiments (**Fig.** 2a, Extended Data **Fig.** 3a). Freshly frozen CG-SMG samples were subjected to SeqFISH[27] to visualize spatial gene expression map. Among all cells, neurons were identified based on the expression of tyrosine hydroxylase (TH), a general sympathetic neuronal marker (Extended Data **Fig.** 3b-d)[28–30]. Further analyses focusing on TH-positive CG-SMG (CG-SMGTH) neurons revealed two molecularly distinct neuron classes expressing relaxin receptor type 1 (CG-SMG^{RXFP1}) or a homeobox gene, *Shox2* (CG-SMG^{SHOX2}, **Fig.** 2b). These two populations exhibited differential expression of several receptors and transduction molecules while sharing similar expression levels of previously described neuropeptides including NPY[31–34] (Extended Data **Fig.** 3e, f). I also found that CG-SMG^{SHOX2} neurons comprise at least two subclasses labeled by the expression of *Bmp3*

and *Dsp* (**Fig.** 2c), although functional differences between these subtypes remain to be tested.

CG-SMG^{RXFP1} and CG-SMG^{SHOX2} neurons, which together account for ~80 % of the entire CG-SMG neurons (**Fig.** 2d), showed unique topological distribution. While both neural populations were distributed in CG and SMG, the majority of CG-SMG^{RXFP1} neurons were located in CG (**Fig.** 2e, f). Different subclasses of CG-SMG^{SHOX2} neurons were intermingled in both CG and SMG (Extended Data **Fig.** 4).

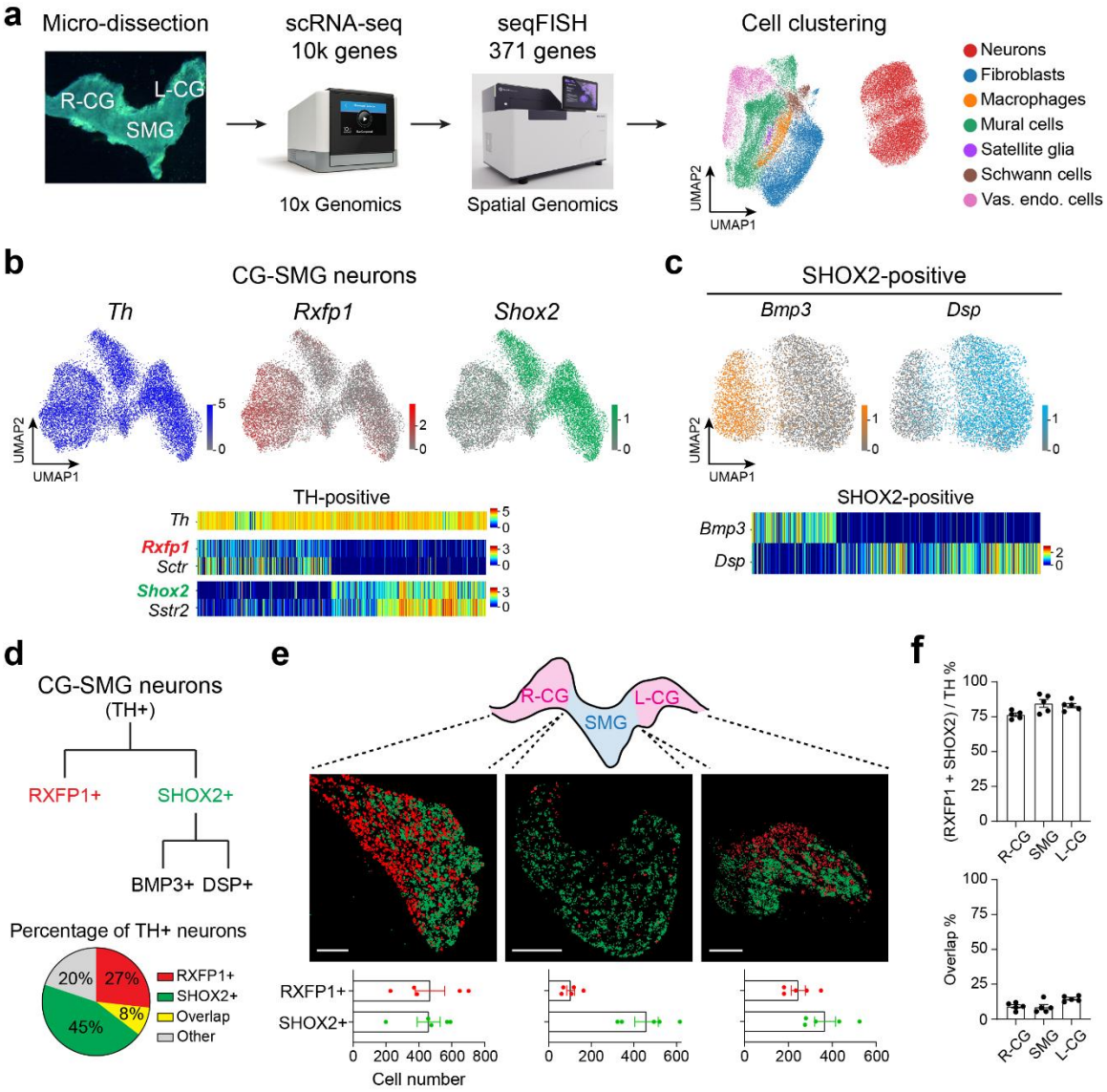

Fig. 2: Multi-transcriptomic analyses reveal molecularly and spatially distinct CG-SMG neural populations. a, Experimental design for identifying transcriptomic cell types and for visualizing spatial localization of cells in the CG-SMG complex. By analyzing >10k genes in scRNA-seq, 371 cell-type marker genes were used for seqFISH analysis. UMAP embedding of major cell types identified from seqFISH experiments (n = 25,932 cells from 5 sections of 3 mice per Right (R)-CG, SMG, Left (L)-CG). Vas. endo. cells, vascular endothelial cells. 10x Chromium Controller and Gene Positioning System images were provided by 10x Genomics and Spatial Genomics, respectively. **b,** SeqFISH analysis of CG-SMG neurons. Top: UMAP plotting for log-normalized *Th* (blue), *Rxfp1* (red) and *Shox2* (green) expression. Bottom: heatmaps of neuronal marker gene expression (n = 13,105 cells). **c,** UMAP (top) and heatmap (bottom) plotting for subtypes of CG-SMG^{SHOX2} neurons (n = 7,152 cells). **d,** Top: a summary diagram of CG-SMG neuronal types. Bottom: a pie chart displaying the percentage of neuron types. **e,** Spatial localization of CG-SMG^{RXFP1} and CG-SMG^{SHOX2} neurons. Representative seqFISH images for the expression of *Rxfp1* (red) and *Shox2* (green) in CG-SMG areas. Scale bar, 200 μm. Shown are quantification of RXFP1- and SHOX2-positive neurons (n = 5 sections of 3 mice per R-CG, SMG, L-CG). **f,** Quantification of RXFP1- and SHOX2-positive neurons in each area of CG-SMG (top) and overlapping percentage (bottom, n = 5 sections of 3 mice per R-CG, SMG, L-CG). Data are presented as mean ± s.e.m.

Using RXFP1-Cre and SHOX2-Cre[35] animals, I explored neuron-to-organ projections. In these lines, I confirmed that Cre was faithfully expressed in CG-SMG^{RXFP1} and CG-SMG^{SHOX2} neurons (Extended Data **Fig.** 5 and 6). For virus tracing, transgenic animals were injected with AAV-FLEX-tdTomato in the CG-SMG complex (**Fig.** 3a). After viral expression, each organ was dissected, cleared in ScaleS solution[36], and fluorescent projection was visualized. In all animals, I validated robust and selective fluorescent expression in CG-SMG (Extended Data **Fig.** 7). TH-Cre animals were used to target CG-SMG neurons ubiquitously.

Intriguingly, each CG-SMG population innervates largely non-overlapping visceral organs (**Fig.** 3b, c and Extended Data **Fig.** 8). CG-SMG^{RXFP1} neurons sent projections to the upper digestive and secretory organs, including the bile duct, HPA, pancreas, and duodenum. The stomach was devoid of projections from CG-SMG^{RXFP1} neurons. Conversely, CG-SMG^{SHOX2} neurons projected to the stomach, and lower intestinal areas (jejunum, ileum, and colon). Neither of these populations showed tissue-layer specific innervation (Extended Data **Fig.** 8c). All visceral organs received strong innervations from CG-SMGTH neurons. These combinatorial organ projections led us to speculate that each population may mediate specific visceral functions.

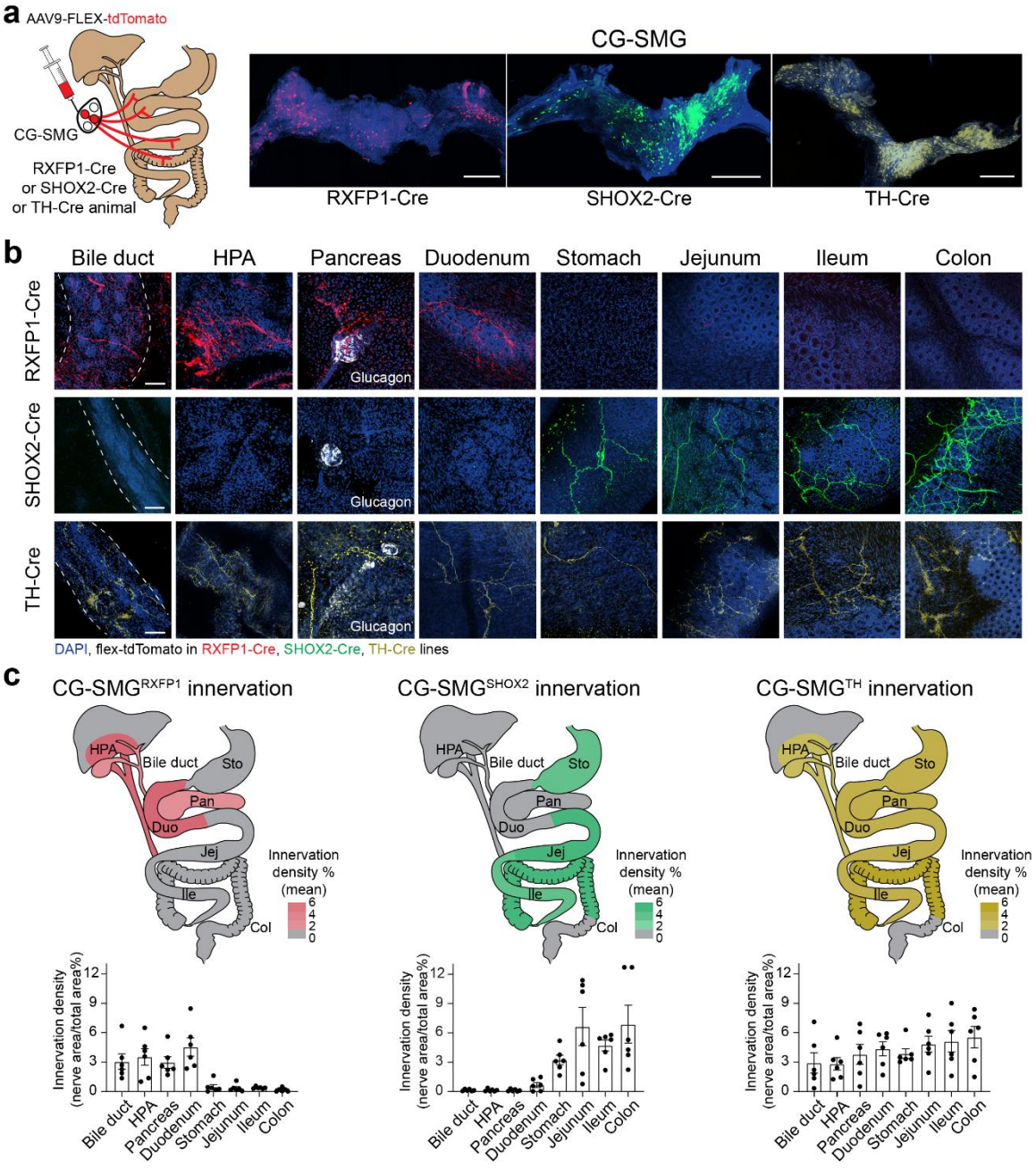

Fig. 3: Complementary organ projections by CG-SMG^{RXFP1} and CG-SMG^{SHOX2} neurons. a, CG-SMG neuron anterograde tracing. Cell bodies and nerve terminals were visualized by injecting AAV-FLEX-tdTomato into CG-SMG of RXFP1-Cre, SHOX2-Cre and TH-Cre animals. Representative images of tdTomato expression after AAV infection are shown with TH immunostaining (blue, n = 3 mice). Scale bar, 500 µm. **b,** Visualization

of CG-SMG axons in visceral organs. Representative images for whole-mount organ innervation of CG-SMG^{RXFP1}, CG-SMG^{SHOX2}, CG-SMGTH neurons as indicated (n = 3). Top and middle: RXFP1+ and SHOX2+ neurons target complementary visceral organs. Bottom: TH+ neurons project to all visceral organs as a positive control. The pancreatic islet is identified by the indicated glucagon antibody staining (white) and nuclei are visualized by DAPI staining (blue). Scale bar, 100 μm. **c,** Summary maps of anatomical innervation patterns by CG-SMG neurons with color-coded average nerve density. The nerve density quantification is shown at the bottom (n = 6 images from 3 mice per organ). HPA, hepatic portal area. Pan, pancreas. Duo, duodenum. Sto, stomach. Jej, jejunum. Ile, ileum. Col, colon. Data are presented as mean ± s.e.m.

NEURONS THAT MODULATE DIGESTIVE FUNCTIONS

To examine the functional role of individual CG-SMG populations, I applied neural manipulation tools to CG-SMG neuron types *in vivo*. We electrophysiologically characterized action potentials induced by optogenetic and chemogenetic stimulation. TH-Cre;Ai32 double transgenic animals were used to express channelrhodopsin (ChR2) in CG-SMGTH neurons (**Fig.** 4a). CG-SMG neurons showed action potentials in response to light pulses, and increasing light frequency caused higher firing rate that plateaued around 10 Hz (**Fig.** 4b). For chemogenetic stimulation, CG-SMG of TH-Cre animals were injected with AAV-FLEX-hM3Dq. Clozapine *N*-oxide (CNO) application to DREADD-expressing CG-SMG neurons induced persistent firing (**Fig.** 4c). These results validated functional perturbation tools in CG-SMG neurons.

The visceral sympathetic system regulates various functions, including gut motility and digestion[37]. I examined how CG-SMG^{RXFP1} and CG-SMG^{SHOX2} populations are involved in these visceral functions. For digestive functions, I investigated bile secretion, a key component of fat digestion in the intestine that receives sympathetic modulation[38]. Due to the extremely low volume of bile secretion, I developed an *in vivo* microfluidic system

combined with computer vision analysis that allows bile measurement at sub-second resolution (**Fig.** 4d, Extended Data **Fig.** 9a, b). Under undisturbed conditions, bile secretion was about 1 μl per min, which was increased by the application of cholecystokinin[39] (Extended Data **Fig.** 9c, d). I explored how secretion speed changes upon manipulation of distinct CG-SMG neurons. Each CG-SMG population was activated either by topical application of CNO or photostimulation (488 nm). As suspected from the projection pattern, optogenetic or chemogenetic stimulation of CG-SMG^{RXFP1} neurons, but not CG-SMG^{SHOX2} neurons, significantly slowed down bile secretion compared to a control group (**Fig.** 4e, f, Extended Data **Fig.** 9e-k). These inhibitory effects were abolished by blocking norepinephrine signaling (Extended Data **Fig.** 9l). Notably, CG-SMG^{RXFP1} neurons densely innervate the bile entry site (Extended Data **Fig.** 8a) suggesting that regulation of bile is mainly at the intestinal entry site (Extended Data **Fig.** 9g).

CG-SMG^{RXFP1} neurons also project to other secretory organs, in particular, the pancreatic islet (Extended Data **Fig.** 8a). Since sympathetic activation leads to glucagon secretion and elevates glucose levels under stress conditions[40,41], I tested whether the CG-SMG^{RXFP1} population concurrently regulate bile and glucagon secretion. Under food-deprived conditions, glucagon levels were significantly increased in portal vein blood (**Fig.** 4g, Extended Data **Fig.** 9m). Chemogenetic activation of CG-SMG^{RXFP1} neurons in sated animals increased glucagon secretion similar to CG-SMGTH neuron stimulation (**Fig.** 4g, Extended Data **Fig.** 9n, o). By sharp contrast, the same functional manipulation of CG-SMG^{SHOX2} population had no effects on glucagon secretion. Ablation of CG-SMG^{RXFP1} neurons showed functional necessity of this population for glucagon secretion under fasting state (Extended Data **Fig.** 9p, q). These results demonstrate that CG-SMG^{RXFP1} neurons innervate combinatorial upper visceral organs, including the bile duct, duodenum, pancreas, and liver, to control digestion- and secretion-related functions.

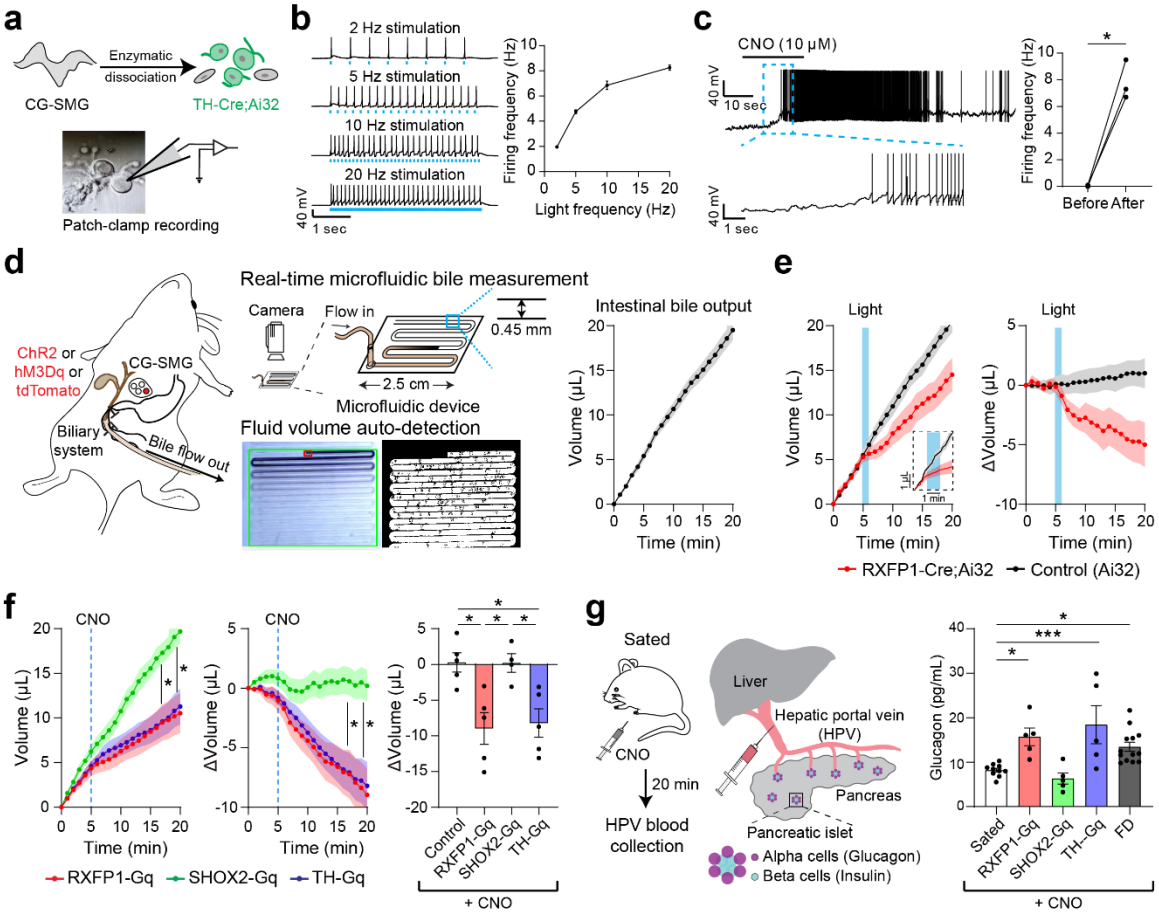

Fig. 4: Activation of CG-SMG^{RXFP1} neurons regulates secretory functions. a, Electrophysiological recording from ChR2-expressing CG-SMG neurons. **b,** Neural responses to 10 ms-long light pulses (n = 5 neurons from 3 mice). **c,** Left: action potentials upon CNO application to hM3Dq-expressing neurons (10 μM). Right: quantification of firing rate before and after CNO application (n = 3 neurons from 2 mice). **d,** Left and middle: schematic for measuring bile secretion volume with a custom microfluidic chamber. Right: Automated fluid detection of bile volume across time is plotted (n = 9 mice). **e,** Optogenetic stimulation of CG-SMG^{RXFP1} neurons inhibited bile secretion. Total bile secretion (left) and volume change (right) over time (n = 4 RXFP1-Cre;Ai32 mice, n = 6 cagemate control mice). Light pulses of 2 ms at 20 Hz were applied at CG-SMG for 1 min as indicated by the blue shade. A zoomed-in view shows a 3 peri-stimulation window with 30 Hz sampling rate. **f,** Left: Chemogenetic activation of CG-SMG^{RXFP1} (red) and CG-

SMG^{TH} (blue) neurons significantly suppressed bile secretion, but not CG-SMG^{SHOX2} (green) neurons. Middle: Bile volume change upon chemogenetic stimulation. Right: Quantification of volume change. RXFP1-Cre animals injected with tdTomato were used as a control group (Extended Data **Fig.** 9j). Data were quantified from 5 mice for RXFP1-tdT, 5 mice for RXFP1-Gq, 4 mice for SHOX2-Gq, and 5 mice for TH-Gq. **g,** Left and Middle: Experimental protocol of measuring blood glucagon level in the hepatic portal vein. Right: Activation of CG-SMG^{RXFP1} (red), but not CG-SMG^{SHOX2} neurons (green) increased glucagon release under sated conditions. n = 10, 5, 5, 5, 13 mice for wild-type sated, RXFP1-Gq, SHOX2-Gq, TH-Gq, wild-type food-deprived (FD) conditions. *P < 0.05, **P < 0.01, ***P < 0.001 by two-tailed paired t-test, one-way or two-way ANOVA with Dunnett's multiple comparisons test. Data are presented as mean ± s.e.m.

NEURONS THAT REGULATE GASTROINTESTINAL TRANSIT

I next explored the functions of the CG-SMG^{SHOX2} population that projects complementary organs. These neurons innervate both myenteric and submucosal plexus of the stomach and distal intestine (**Fig.** 3c, Extended Data **Fig.** 8c). Based on this innervation pattern, I suspected that the CG-SMG^{SHOX2} population may contribute to the GI transit[42]. To test this idea, I quantified food transit by subjecting animals to food deprivation, allowing them brief access to dyed chow (10 min), and examining the upper gut transit mainly controlled by the stomach (**Fig.** 5a, Extended Data **Fig.** 10a-d). I found that stimulation of CG-SMG^{SHOX2} or CG-SMG^{TH} neurons drastically suppressed the GI transit but did not reduce food intake (**Fig.** 5b, Extended Data **Fig.** 10b). Conversely, negligible effects were observed when I activated CG-SMG^{RXFP1} neurons (**Fig.** 5c). These results show that CG-SMG^{SHOX2}, but not CG-SMG^{RXFP1} neurons control food transit after ingestion. I further tested fecal output in awake-behaving animals as a proxy for lower gut motility[43]. Under sated conditions, CG-SMG^{SHOX2} or CG-SMG^{RXFP1} neurons were activated by CNO while observing the number of stools produced during the next 3-hour period (**Fig.** 5d). Stool expulsion was essentially abolished when CG-SMG^{TH} or CG-SMG^{SHOX2} neurons were

activated (**Fig.** 5e, Extended Data **Fig.** 10e, f). This suppression effect was mediated by norepinephrine (Extended Data **Fig.** 10g). By contrast, stimulation of CG-SMG^{RXFP1} neurons did not have any effects (**Fig.** 5f). Consistent with the upper and lower gut transit results, activation of CG-SMG^{SHOX2} neurons significantly delayed total gut transit (**Fig.** 5g, Extended Data **Fig.** 10h). Taken together, this study demonstrate that sympathetic neurons comprise diverse cell types, each serving as a functional module that controls functionally related visceral organs (**Fig.** 5h).

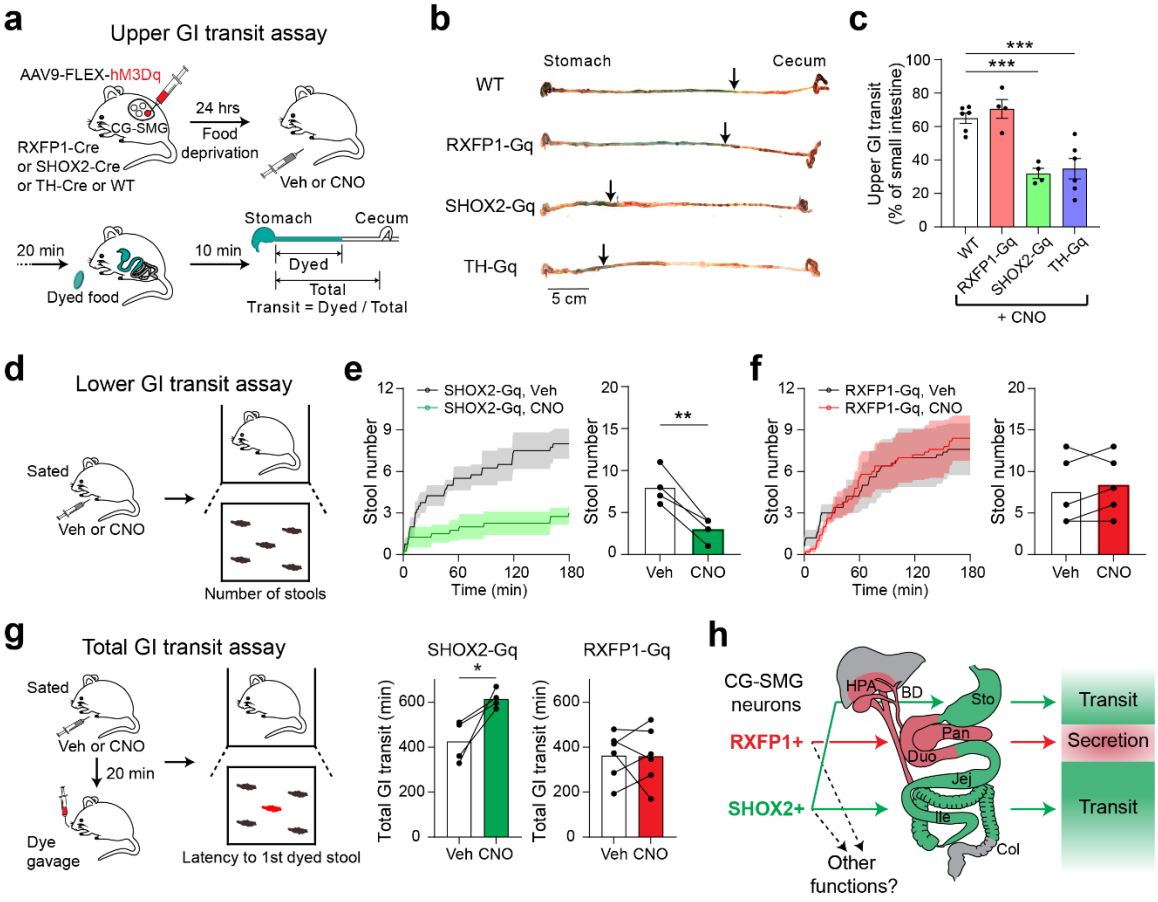

Fig. 5: Activation of CG-SMG^{SHOX2} neurons inhibits gut transit. a, An experimental design for the upper GI transit measurement using dyed food with chemogenetic activation. **b,** Representative images of the small intestine after activating individual CG-SMG neuron populations. Arrows indicate where dyed food (blue) travels after 10 min of feeding. **c,** Quantified data showing that the upper GI transit was significantly suppressed by the

activation of CG-SMG^{SHOX2} or CG-SMGTH neurons, but not by CG-SMG^{RXFP1} neurons. Wild-type sham-surgery animals were examined after intraperitoneal CNO administration. n = 6 mice for WT, 4 mice for RXFP1-Gq, 4 mice for SHOX2-Gq, 6 mice for TH-Gq groups. **d,** Schematic for stool number measurement. Upon intraperitoneal vehicle (Veh) or CNO application, sated animals were placed in an open field chamber for 3-hour video recording. **e,** Chemogenetic stimulation of CG-SMG^{SHOX2} neurons suppressed spontaneous stool expulsion. The total number of stools was plotted and quantified (n = 4 mice). **f,** Conversely, activation of CG-SMG^{RXFP1} neurons had no effects on stool defecation (n = 5 mice). **g,** Chemogenetic activation of CG-SMG^{SHOX2} neurons significantly delayed the total GI transit (n = 4 mice), while stimulating CG-SMG^{RXFP1} neurons had no effects (n = 6 mice). Carmine dye was gavaged to quantify the latency to first dyed stool. **h,** Modular sympathetic regulation of visceral organs. $^{*}P < 0.05$, $^{**}P < 0.01$, $^{***}P < 0.001$ by two-tailed paired *t*-test or one-way ANOVA with Dunnett's multiple comparisons test. All data are shown as mean ± s.e.m.

DISCUSSION

Recent studies highlighted diverse neural populations in ascending and descending nervous systems[3,7,11,18]. The vagal and spinal sensory neurons comprise molecularly distinct populations with various sensory functions. Here, I show that the sympathetic nervous system also shows cellular and molecular diversity. *Rxfp1* and *Shox2* are expressed by two types of neurons in CG-SMG. Furthermore, GI-innervating CG-SMG^{SHOX2} neurons contain at least two populations (**Fig.** 2d). These results are in accordance with recent studies in other sympathetic chain ganglia[28,29]. However, our transcriptomic analyses identified only a few different CG-SMG neuron types. This simple cellular composition may reflect the relatively narrow functionality of the sympathetic system. Alternatively, future higher-resolution transcriptomic analyses could reveal more granular cell classes with distinct functionality.

Various models have been proposed to explain how the sympathetic nervous system regulates peripheral organs. One such model is a uniform regulation where visceral functions are ubiquitously controlled by the sympathetic system[44,45]. Another model suggests that different organs are controlled by distinct sympathetic populations[46,47]. Our study strongly favors the latter model: CG-SMG^{RXFP1} and CG-SMG^{SHOX2} neurons exhibited complementary projection patterns with distinct functions. CG-SMG^{RXFP1} neurons project to secretory sites (bile duct, duodenum, pancreas, and the liver), whereas CG-SMG^{SHOX2} neurons send innervations to the visceral GI tract. Our functional perturbation experiments supported separate functions between these populations for controlling bile and glucagon secretion vs. the GI transit. Further analyses are required to determine if each CG-SMG population contributes to other visceral functions, and how specific tissues and layers within the same organ are innervated by sympathetic populations.

The activity of sympathetic neurons is regulated by descending signals from the brain through pre-ganglionic neurons that reside in the spinal cord. Previous studies extensively characterized the activity of these pre-ganglionic neurons under different physiological conditions such as hunger or hypoxia[48,49]. How pre-ganglionic neurons connect to CG-SMG and other sympathetic ganglia to regulate activity is unknown. Exploring the descending sympathetic circuits at cell-type-specific precision presents an intriguing prospect, particularly after identifying genetically defined CG-SMG populations. Deciphering individual brain-to-body pathways may offer avenues for refined therapeutic solutions by regulating specific functions, such as altering blood glucose levels and GI motility independently.

EXPERIMENTAL MODELS AND METHOD DETAILS

Animals

All experimental procedures were in accordance with US National Institutes of Health guidelines for the care and use of laboratory animals, and were approved by the California Institute of Technology Institutional Animal Care and Use Committee (IACUC; protocol #1694 and 1866). Male and female animals of at least 7 weeks old were used for data collection. Ai32 (#024109), and C57BL/6J (#000664) lines were acquired from the Jackson Laboratory. RXFP1-Cre line was developed in our previous publication[50]. SHOX2-Cre animals were generously provided by Y. Chen[35]. TH-Cre mice were a gift from D. Anderson. Animals were housed in a facility with controlled temperature (71-75°F) and humidity (30-70%), following a 13:11 hour light-dark cycle. Animals had *ad libitum* access to chow and water.

Viral constructs

The following viral constructs were used: AAV9-CAG-FlEX-tdTomato, 2.8 x 10^{13} genome copies per ml (Addgene, 28306-AAV9). AAV9-CAG-DIO-hM3D(Gq)-mCherry, 1.1 x 10^{13} genome copies per ml (Canadian Neurophotonics Platform Viral Vector Core Facility, 651-aav9). AAV8-EF1a-mCherry-FLEX-DTA, 3 x 10^{13} genome copies per ml (Salk Institute, 58536). AAV5-FLEX-taCaspase3-TEVP, 4.2 x 10^{12} genome copies per ml (UNC Vector Core).

Surgery

For all survival surgeries, mice were anesthetized with a mixture of ketamine (100 mg/kg body weight) and xylazine (5 mg/kg body weight) solution via intraperitoneal administration. Ketoprofen (5 mg/kg body weight) and buprenorphine XR (3.25 mg/kg body weight) were subcutaneously applied prior to surgery. Animals were placed on their backs and the abdomen was incised along the midline.

Celiac-superior mesenteric ganglia injection

The CG-SMG complex was exposed following reflection of the viscera. The small and large intestine were externalized and covered by a wet, sterile gauze. Using the superior mesenteric artery and celiac artery as landmarks, 100-300 nl virus containing 0.05% Fast Green FCF (Sigma, F7252-5G) was delivered to three sites (left CG, SMG and right CG) of the CG-SMG complex at a rate of 100 nl/min with a microprocessor-controlled injection system (World Precision Instruments, Nanolitre 2000). Successful injection was visualized by Fast Green FCF dye slowly filling the ganglion without leakage. For the anterograde virus tracing experiments, tissue collection was done at least 3 weeks after the injections. For the chemogenetic experiments, animals had at least 2 weeks of recovery period.

For anterograde tracing from individual ganglion of CG-SMG, 300 nl DiI (Invitrogen, D3899) was injected to either left CG, SMG or right CG at a rate of 100 nl/min. Tissue was collected three days after surgery.

Retrograde tracing from visceral organs

After the abdominal incision, a total of 0.5-1 μl retrograde tracer (WGA 488 or WGA 647, ThermoFisher, W11261, 5 mg/mL) was injected to the target organ at 100 nl/min. For GI tract injection, tracer was delivered into the layer between the muscularis externa and serosa at 4-8 sites, covering a total area of approximately 1 cm^2. For injection to the spleen and pancreas, tracer was uniformly administered across the organ's surface at 4-8 evenly spaced sites. For injection to the HPA, tracer was delivered to the connective tissue surrounding the portal vein and the areas of the liver where portal vein enters. Peripheral ganglia were harvested three days post-injections for histological and imaging analyses. For dual-color tracing experiments, two or three regions containing both WGA 488- and WGA 647-labeled cells were quantified for the ratio of double-positive cells among all WGA-positive cells.

Organ topographical mapping

To perform organ topographical mapping on the CG-SMG complex, CG-SMG neurons were retrogradely traced from eight organ sites (spleen, HPA, pancreas, stomach, duodenum, jejunum, ileum and colon) by WGA dye as described above. Three mice per organ site were injected. I developed a computational pipeline to build a standardized reference anatomy image, align WGA-labeled ganglia image, and register WGA-positive cells, by applying the VoxelMorph library (version 0.2)[51,52] in Python (3.9.17). In brief, the entire CG-SMG ganglia complex was whole-mount and z-stack imaged to visualize all projecting neurons via confocal microscopy (Leica, TCS SP8). By digitally drawing vertical lines from both the left and right sides towards the center, I determine the lateral boundaries to be at 20% of its maximum width.

The atlas was generated using the TemplateCreation network with default architecture and mean squared error (MSE) loss. Other model settings were: batch size = 1, steps per epoch = 100, loss weight = [0.5, 0.5, 1, 0.01], learning rate = 1e-4. All input images for the network were first resized to 128 pixels x 64 pixels. In particular, the initialization of the reference was the average of the training dataset comprising twenty stained CG-SMG training images. I trained the neural network over 25 epochs for performance optimization. Consistent atlas was built from DAPI- or TH-stained images (Extended Data **Fig.** 1b). The atlas generated from the CG-SMG dataset of DAPI staining was used for the following image registration on the organ mapping dataset of 64 WGA-labeled images. WGA-positive cells on DAPI background were auto-detected using the OpenCV (4.5.1) library, and the cell coordinates were obtained. The number of WGA-positive cells was automatically counted (Extended Data **Fig.** 2b). Next, I trained the VxmDense network on WGA-labeled images with default architecture, MSE loss, batch size = 4, steps per epoch = 50, loss weight = [1, 0.1], learning rate = 1e-4, and number of epochs = 25. All input images for the network are first resized to 256 pixels x 128 pixels. Each WGA-labeled image was aligned to the reference atlas based on DAPI staining by the unsupervised model. This same spatial transformation was applied to WGA-positive cells. I calculated the mapping of WGA-positive cell coordinates from WGA-labeled images to the atlas.

After image registration, WGA-positive cells were plotted on the atlas image as scaled Gaussian heatmaps using 'gaussian_filter' in 'SciPy' (1.11.1) package.

Bile secretion measurement

Fabrication of the microfluidic chamber

The microfluidic channels were 3D printed (Elegoo Mars 3) using ultraviolet-sensitive polymer resin (Anycubic High Clear Resin). The structure was then cleaned with isopropyl alcohol to remove excess resin, followed by ultraviolet treatment under 365 nm light for 2 min and heat curing at 80ºC for 2 min. The chamber's top layer, a 75 μm polyethylene terephthalate (PET, McMaster-Carr) sheet, was attached using double-sided medical adhesive (3M). This bilayer was cut using a 50W CO2 laser cutter (Universal Laser System) at 40% power, 100% speed, 1000 PPI, vector mode, 2 copies. The PET layer, with laser-cut inlet and outlet holes, was then laminated onto the 3D printed channels. A watertight inlet seal was created by gluing a silicone rubber connector (Dragon Skin™ FX-Pro™, Smooth-On), which was shaped in a 3D printed mold and cured at 80ºC for 5 min.

Surgical procedure for bile secretion measurement

Under isoflurane anesthesia, a skin incision was made along the abdominal midline. A small fragment (< 1 cm, within 1.5 cm from the sphincter) of duodenum containing the bile duct entry was isolated by tying both ends with sutures (Ethicon, K802H). Then an intraintestinal tube (HelixMark®, 60-011-04) was positioned adjacent to the bile duct entry site, secured by sutures, and connected to the customized microfluidic chamber. For the bile duct tubing, the duct was first ligated near the duodenum and then incised for the tube (Instech, BTPU-014) insertion. A camera was positioned vertically above the microfluidic chamber for video recording at a frame rate of 30 Hz.

For optogenetic stimulation, an optic fiber was held with tip close to the right CG, delivering 20 Hz, 473-nm laser pulses (2-ms duration) for 1 min with the pulse generator (Quantum composers, Sapphire 9200). The laser intensity was maintained at 5 mW at the

fiber tip. For positive control, CCK (Bachem, 4030663, 0.625 µg/kg body weight) was intraperitoneally administrated at 50 µl/min using an infusion syringe pump (New Era Pump Systems, NE-300) during 30 sec. For chemogenetic manipulation, clozapine N-oxide (CNO) (Sigma, 2.5 mg/kg body weight) or vehicle (PBS) was locally administered around the hepatic region (bile duct and duodenum). For the antagonist experiment in Extended Data **Fig.** 9l, labetalol hydrochloride (5 mg/kg body weight, Sigma, PHR1335) was intraperitoneally injected 10 min prior to anesthesia. Mice were immediately euthanized for histological verification after the recording session.

Computer vision-based video analysis

Dried soluble black ink was placed at the inlet of the microfluidic chamber to visualize the fluid flow's tip (Extended Data **Fig.** 9b). As bile enters the chamber, the tip of the flow becomes marked by the black ink, enhancing its visibility. The initial 10-min equilibration period was not included in the video analysis. The fluid flow tip's location and the cumulative area covered by the fluid were tracked using background subtraction method in OpenCV (4.5.1). The volume of fluid over time was calculated based on the specifications of the microfluidic device, and this data was recorded for every frame, achieving a resolution at the nanoliter scale with a sampling rate of 30 Hz. To normalize the flow volume in **Fig.** 4e and f, the average flow rate in **Fig.** 4d was subtracted. Data points representing the first frame of each minute were plotted unless indicated in the figure legend. In Extended Data **Fig.** 9c, the average flow rate of three minutes before and after bile duct transection was quantified. In Extended Data **Fig.** 9d, the average flow rate during the minute before and after CCK application was quantified. For optogenetic experiments, the average flow rates of the minute after light stimulation were quantified (Extended Data **Fig.** 9e,f).

Plasma glucagon concentration measurements

The following groups were tested: sated, 24-hour food-deprived wild-type mice, and sated transgenic mice with DREADD-expressing CG-SMG neurons. Intraperitoneal CNO

injection was performed 20 min before blood collection. For food deprivation, animals had free access to water and single chow pellet daily. The hepatic portal vein blood was collected to tubes with sodium fluoride / Na_2EDTA additive (BD, 365992) under isoflurane anesthesia. Plasma was obtained by centrifugation at 1500 g for 20 min. The glucagon concentration was determined by ELISA kit (RayBiotech, EIAM-GLU-1).

Systemic glucose level measurements

Systemic glucose level was assessed using a glucometer (KETO-MOJO) on blood samples obtained following toenail trimming under isoflurane anesthesia. Sated and 24-hour food-deprived wild-type mice were examined. RXFP1-Gq animals were tested 20 min after intraperitoneal injection of either PBS (as a control vehicle) or CNO. Additional measurements were conducted 40 min post-CNO delivery. Each measurement was separated by a minimum recovery period of one week.

Assessment of food transit

Animals were food deprived for 24 hours prior to the food transit experiments. Chow pellets were uniformly coated with food-grade dye through a quick immersion process, followed by drying on a hotplate at 80 °C for 20 min. Twenty minutes following the intraperitoneal administration of PBS or CNO (2.5 mg/kg body weight), animals were placed in an empty cage with one dyed pellet and were euthanized between 3 to 30 minutes into their meal, as indicated in figures. The gut was immediately evaluated either by terminal dissection or through rapid surgical opening under isoflurane anesthesia. The extent to which the dye had traveled was quantified as a percentage of the total length of the small intestine, from the pyloric sphincter to the ileocecal junction.

Behavioural assays

<u>Stool analysis</u>

Individual sated animals were located in a 25 cm x 25 cm acrylic open field chamber after intraperitoneal PBS or CNO injection, and were recorded for three hours at 30 frames per sec. The stool number was quantified based on the videos. For the antagonist experiment in Extended Data **Fig.** 10g, labetalol hydrochloride (5 mg/kg body weight, Sigma, PHR1335) was intraperitoneally injected 20 min prior to CNO administration.

Total GI transit

Oral gavage solution was prepared by dissolving methylcellulose (0.5% w/v) in hot distilled water and then mixing with carmine (6% w/v, Sigma, C1022). Mice were gavaged with 300 µl gavage solution between 8-10 am local time. Animals were then placed in acrylic chamber, which is 12.5 cm x 12.5 cm in area where they can move freely. Video was recorded at 30 frames per sec until the first red fecal pellet of each animal was observed or until 10.5 hours.

Food intake

Animals were individually housed and acclimated to the BioDAQ cages (Research Diets) for 3 consecutive days. For food intake measurement, mice were food deprived for 24 hours and intraperitoneally injected PBS or CNO 20 min before the experiments. The total chow intake in 10 min was quantified.

CG-SMG neuron electrophysiological recordings

CG-SMG neuron isolation

CG-SMG neurons from adult mice were acutely isolated using an enzymatic dispersion technique modified from a previous procedure[53]. In brief, mice were euthanized by cervical dislocation under isoflurane anesthesia, and perfused with cold artificial cerebrospinal fluid (ACSF). The CG-SMG complex was dissected to cold ACSF, and the connective tissue capsule was carefully peeled and removed under dissecting microscope. The ganglia were minced with iridectomy scissors into fine pieces and then transferred to a 35 mm petri dish

containing 2 ml enzyme mix (0.4 mg/ml Trypsin (Roche), 1.2 mg/ml collagenase D (Roche), 0.15 mg/ml DNase I (Roche) dissolved in EBSS (Sigma)). The tissue fragments were incubated in the enzyme mix for 1 hour at 35 °C, bubbled with 5% CO2 and 95% O2. After enzyme digestion, 2 ml of minimum essential medium (MEM) containing 10% FBS, 1% glutamine and 1% penicillin-streptomycin antibiotics was added to the petri dish. The cell suspension was then centrifuged at 200 g for 5 min. Discard the supernatant and resuspend the cells with the MEM solution mentioned above. Gentle trituration is optional to help break down ganglion tissue and isolate CG-SMG neurons. The cells were plated onto cover glass coated with Cell-tek (Corning) and incubated in a humidified atmosphere at 5% CO2 in air at 37 °C prior to patch-clamp recordings.

CG-SMG neuron electrophysiology

For patch-clamp recordings, isolated CG-SMG neurons were plated in recording chamber and placed on an upright microscope (Examiner.D1, Zeiss) perfused with normal ACSF (in mM: NaCl 124, KCl 2.5, NaH_2PO_4 1.2, $NaHCO_3$ 24, glucose 25, $MgSO_4$ 1, $CaCl_2$ 2, and bubbled with 95% O_2/5%CO_2). Electrical signals were filtered at 3kHz with Axon MultiClamp 700B (Molecular Devices) and collected at 20 kHz with Axon Digidata 1550A (Molecular Devices). For current clamp recordings, intracellular solution contains (in mM) K-gluconate 145, NaCl 2, KCl 4, HEPES 10, EGTA 0.2, Mg-ATP 4, Na-GTP 0.3 (pH 7.3). Thin wall patch pipettes (OD = 1.5 mm, ID = 1.17 mm, Sutter Instrument) were fabricated on a model P-97 micropipette puller (Shutter Instrument) and fire polished on a microforge to a resistance of 2 – 3 MΩ.

For optogenetic experiments, light beam from an LED light source (X-Cite 120LED, Excelitas Technologies) was delivered through an optical filter (475/30). Light pulses (10 ms) were given at 2 – 20 Hz for 4 sec in experiments as in **Fig.** 4b to evoke action potentials in CG-SMG neurons. For chemogenetic experiments, CNO was applied through a puffing pipette directly located adjacent to the recording neuron. Electrophysiological data were acquired by Clampex (10.7) and analyzed in Clampfit (10.7).

Single-cell RNA sequencing

Five male and five female C57BL/6J mice of 7 weeks old were used to prepare per single-cell RNA sequencing (scRNA-seq) run on the 10x Genomics platform. Across two sequencing runs, a total of 24,873 cells were profiled, which included 1,558 neurons. Upon isoflurane anesthesia, mice were euthanized by cervical dislocation, and perfused with ice-cold HEPES-ACSF (in mM: NaCl 92, KCl 2.5, NaH_2PO_4 1.25, $NaHCO_3$ 30, HEPES 20, glucose 25, $MgSO_4$ 1, $CaCl_2$ 2, kynurenic acid Na salt 1, Na-ascorbate 5, thiourea 2, Na-pyruvate 3, and bubbled with 95% O_2/5%CO_2). Under dissecting microscope, the CG-SMG complex was rapidly extracted to 1ml ice-cold ACSF, and the connective tissue capsule was carefully peeled and removed. After tissue harvest, HEPES-ACSF was replaced by 1 ml enzyme digestion buffer 1 (HEPES-ACSF) containing papain (80 U/ml; Worthington, PAPL, LS003119; pre-activated with 2.5 mM cysteine and a 30-min incubation at 34 °C) and TrypLE™ Express Enzyme (1X, 400 µl/ml; ThermoFisher, 12604013). During enzymatic digestion the tissue was pipetted periodically every 10 min. After incubation at 34 °C with gentle carbonation for 35 min, the CG-SMG tissue was carefully washed one time with 1 ml HEPES-ACSF. One ml of the enzyme digestion buffer 2 (HEPES-ACSF) containing collagenase type 2 (2 mg/ml; Worthington, LS004174), dispase II (2 mg/ml; Sigma, D4693-1G), deoxyribonuclease I (0.2 mg/ml; Worthington, LS002007) and supplemented with 2 mM CaCl2 was applied. After incubation at 34 °C with gentle carbonation for 20 min, the CG-SMG tissue was carefully washed one time with 1 ml HEPES-ACSF. The medium was replaced with 100 µl HEPES-ACSF containing 0.1 µM Calcein AM (ThermoFisher, C1430), 4 µM ethidium homodimer-1 (EthD1, ThermoFisher, E1169), and 0.02 mg/ml deoxyribonuclease I. Tissue was gently triturated into a single-cell suspension with consecutive rounds of trituration with fire-polished glass Pasteur pipettes with tip diameters of around 600, 300 and 150 µm. The suspension was brought up to 200 µl and pipetted through a 40-µm cell strainer (pluriStrainer, 43-10040) into a new microcentrifuge tube and incubated on ice for 5 min. Calcein AM-positive and EthD1-negative singlets were sorted (Sony, MA900) and collected in 4 °C HEPES-ACSF containing 0.05% BSA. The sorted cell suspension was centrifuged with 400 g for 4 min

at 4 °C. The supernatant was discarded, and the cell pellet was resuspended with 55 µl fresh ice-cold HEPES-ACSF and kept on ice while the cell density was counted with a hemocytometer. The final cell suspension volume estimated to retrieve 10,000 single-cell transcriptomes was loaded to the 10X Single Cell G chip (10x Genomics, PN-1000127). The Chromium Single Cell 3' GEM, Library and Gel Bead Kit v3.1 (PN-1000128) and the Single Index Kit T Set A (PN-1000213) were used. The cDNA and library amplification underwent 11 and 12 cycles respectively. The scRNA-seq libraries were sequenced on a NovaSeq S4 lane (paired-end 150). The sequencing reads were mapped to the custom pre-mRNA reference transcriptome[54], and gene-cell matrices were generated via the 10x Genomics Cell Ranger v.6.1.2 pipeline. Subsequent gene expression analyses were conducted in Python (3.8.18) using ScanPy (1.9.2) as previously described[55] unless specified. Extended Data **Fig.** 3a was plotted in R (4.1.1) using Seurat (4.2.1)[56]. Cells were filtered if possessing fewer than 1,500 or more than 45,000 unique transcripts, or more than 10% of mitochondrial transcripts. Differential gene expression analysis was performed between RXFP1+ and SHOX2+ clusters using 'PyDESeq2' (0.4.4)[57]. In Extended Data **Fig.** 3f, genes are ranked by their expression fold change (log_2).

Spatial transcriptomics

SeqFISH gene panel design

A custom seqFISH panel was designed to incorporate CG-SMG cell-type-marker genes based on our scRNA-seq data analysis. The panel contained 371 genes of which 341 were detected using barcoded seqFISH imaging and 30 were identified serially via single-molecule FISH. The panel was custom ordered by Spatial Genomics, Inc.

SeqFISH sample preparation

Adult (8-12 weeks old) C57BL/6J male mice were euthanized by cervical dislocation under isoflurane anesthesia. After dissecting the CG-SMG complex to ice-cold PBS, right, left and medial CG-SMG samples were obtained by surgically separating the connected CG-

SMG region between the celiac artery and the superior mesenteric artery. The tissue was freshly embedded in Tissue-Tek O.C.T. Compound (Sakura, 4583), and then flash-frozen in liquid nitrogen. Cryosections of 10-µm thickness were cut and mounted onto treated coverslips. Immediately post-collection, sections were fixed in fresh 4% paraformaldehyde (PFA, Thermo Scientific, 28908) for 15 min at room temperature. After rinsing three times in 1X PBS for 5 min each, sections were dehydrated using 70% ethanol for 30 sec at room temperature. The sections were air-dried at room temperature for approximately 15 min and stored at -80 °C. SeqFISH experiments were performed using the seqFISH+ protocol with some modifications at Spatial Genomics, Inc. Briefly, the fixed tissue sections underwent permeabilization in 70% ethanol followed by clearing, rinsing, and air-drying steps. The coverslip containing each section was assembled into Spatial Genomics custom flow cells. The flow cells were then hybridized with the seqFISH primary probe panel and incubated in a humidified chamber at 37 °C for 24 hours. After hybridization, samples were washed with buffers for subsequent imaging.

SeqFISH imaging via Gene Positioning System

Imaging was performed using the Gene Positioning System (GenePS, Spatial Genomics, Inc.), which enables automated image acquisition, reagent delivery, and data processing. The ganglion section was selected as a region of interest (ROI) for the experiment based on the brightfield and/or DAPI images. Automated experiment execution was initiated post-ROI selection. Each experiment proceeded through multiple rounds of decode probe hybridization, imaging, and signal removal until all the hybridization rounds were complete.

Image processing and analyses

Raw-image files were processed on instrument to align images across multiple hybridization rounds and detect RNA fluorescent signals. The data were further analyzed using custom Spatial Genomics analysis software to decode the transcript identities and segment cells. Cell segmentation was performed using a machine learning algorithm based

on the cell nuclear DAPI stain or TH stain. The decoded RNA molecules were then assigned to individual cells, generating cell-by-gene count matrices and individual cell center coordinates for each ROI.

Subsequent gene expression analyses were conducted in Python (3.8.18) using ScanPy (1.9.2) as previously described. Cells that had unique gene counts of less than 10 were filtered. Harmony (0.0.9) package was used to integrate different batches of seqFISH datasets. Gene expression count data were normalized per cell and log-transformed for downstream analyses by sc.pp.normalize_total and sc.pp.log1p functions. I then performed dimensionality reduction with principal component analysis (PCA) and uniform manifold approximation and projection (UMAP) analysis, followed by unsupervised clustering using the Leiden algorithm through the sc.tl.leiden function. To identify major cell classes, I used a DAPI-based segmented dataset and compared the expression patterns of known cell-type specific marker genes within each cluster. To reduce the effects of high *TH* expression in non-neuronal cells on clustering results, I prioritized the annotation of non-neuronal cells over neurons and accordingly adjusted the weighing of *TH* expression level in non-neuronal cells. To determine neuron subtypes, I proceeded with 13,105 neurons from TH-based segmentation. To quantify the number of neurons, RXFP1-, SHOX2-, TH-, BMP3-, and DSP-positive neurons are defined as log-normalized expression RXFP1 > 0.6, SHOX2 > 0.6, TH > 0, BMP3 > 0, DSP > 0, respectively.

RNAscope-based multicolor *in situ* hybridization

In situ hybridization was performed with the RNAscope Multiplex Fluorescent Assay version 2 (ACD, 323110). Fresh-frozen lateral and medial CG-SMG ganglia sections from C57BL/6J, RXFP1-Cre, SHOX-Cre and TH-Cre animals were prepared following the manufacturer's protocols. The following probes were applied to visualize gene expression: CRE (ACD, 312281, 474001), RXFP1 (ACD, 458001, 458001-C3), SHOX2 (ACD, 554291-C3), and TH (ACD, 317621-C2). The samples were imaged with confocal microscopy and were manually quantified.

Histology

Ganglia or brain expression

Mice were euthanized with CO2 and perfused with PBS followed by 4% PFA. Ganglia and brain were extracted and post-fixed for 1 hour and overnight at 4 °C in PFA, respectively, followed by rinsing two times with PBS. The samples were blocked (10% donkey serum, 0.2% Triton X-100 in PBS) for 1 hour at room temperature and incubated with primary antibodies overnight at 4°C. The following primary antibodies were used: rabbit anti-CHAT antibody (1:500; Abcam, ab178850), chicken anti-NeuN antibody (1:500; Millipore, ABN91), and chicken anti-TH antibody (1:500; AvesLab, TYH-0020). After washing 3 x 10 min with PBS, the tissue was stained with the secondary antibody (1:500; Jackson Immunoresearch) and DAPI (2 mg/ml) for 4 hours under room temperature. The following secondary antibodies were used: donkey anti-chicken 488 (703-545-155), donkey anti-chicken 647 (703-605-155) and donkey anti-rabbit 647 (711-605-152). After three times washing with PBS, the ganglia were mounted on the glass slide and imaged with confocal microscopy.

Organ innervation

Mice were euthanized with CO2 and perfused with PBS followed by 4% PFA. Tissue samples were extracted and post-fixed overnight at 4 °C in PFA. Approximately 2 cm-length samples from the middle of each segment of the GI tract, such as the duodenum, jejunum, and ileum, were harvested. The entire colon was uniformly divided into four sections and collected, from the proximal to the distal end. The tissue was then longitudinally incised and flattened. For whole-mount visceral organ staining, tissue was blocked (10% donkey serum, 0.2% Triton X-100 in PBS) overnight at 4 °C and incubated with primary antibodies overnight at 4°C. The following primary antibodies were used: goat anti-alpha-smooth muscle actin (1:1000; Novus Biologicals, NB300-978), rabbit anti-glucagon antibody (1:500; Abcam, ab92517), rat anti-mCherry (1:500; Invitrogen, M11217). After washing 5 x 1 hour with 0.1% PBST, the tissue was stained with the

secondary antibody (1:500; Jackson Immunoresearch) and DAPI (2 mg/ml) overnight at room temperature, washed 3 x 1 hour with 0.1% PBST. The following secondary antibodies were used: donkey anti-rat Cy3 (712-165-150), donkey anti-goat 647 (705-605-147), and donkey anti-rabbit 488 (711-545-152). Tissue was then cleared in ScaleS solution overnight at room temperature. Samples were mounted in ScaleS with 0.5-mm spacers (SUNJin Lab, IS011) on slides and imaged with confocal microscopy.

Quantification of targeted cells and innervation density

One CG and one SMG z-stack image of 775 μm x 775 μm were quantified for each animal in ImageJ (1.54k). The average number of targeted cells from these two images was calculated. One z-stack image of each sample area was used to quantify virus-positive cells. The cell number per square millimeter was plotted in Extended Data **Fig.** 7c.

Projected organ innervation images of 581 μm x 581 μm were automatically segmented by the MaxEntropy auto-threshold function in ImageJ. In **Fig.** 3, for each organ from each animal, two images were quantified. Nerve density was calculated as the ratio of Nerve Area to Total Area as described in a recent publication[43].

Statistics and data collection

Data were processed and analyzed by GraphPad Prism 10.2.0 and 10.3.1. No statistical methods were used to predetermine the sample sizes. Randomization was performed when allocating animals to experimental groups. Chemical administration sequences such as vehicle and CNO were randomized. Data collection was not blinded, but data analysis was performed with the experiment conditions blinded. Data are presented as means ± s.e.m. Two-tailed paired or unpaired *t*-test, and one- or two-way ANOVA with post-hoc tests were applied to decide the significance level. No significance (ns) was set at $p > 0.05$. The significant threshold was held at $^{*}P < 0.05$, $^{**}P < 0.01$, $^{***}P < 0.001$.

Data availability

Source data are provided with this paper. scRNA-seq data from CG-SMG cells are available at the Gene Expression Omnibus under accession number GSE278457. The organ innervation and seqFISH data were deposited at Zenodo (#13306861, #13883320).

Code availability

All code used in this manuscript is available at https://github.com/YTwTJ/Organ-Specific-Sympathetic-Innervation-Defines-Visceral-Functions.

Acknowledgments

We thank the members of the Oka laboratory, Yijie Zhang and Takako Ichiki for helpful discussion and comments; Jacob Hauser, Mari Oka and Avedis Tufenkjian for maintaining and genotyping mouse lines. TW thanks Yijie Zhang for helping with data analysis. We thank Qilan Liang and Yiping Chen for generously providing the SHOX2-Cre line; Bei Zhang and Kirsten Frieda for help on seqFISH experiments; James Linton, Felix Horns and Michael Elowitz for sharing the cell sorter; David Anderson and the Single-Cell Profiling and Engineering Center for instrumental support with scRNA-seq experiments; Wenfei Han and Ivan De Araujo for advice on surgical techniques.

SUPPLEMENTAL INFORMATION

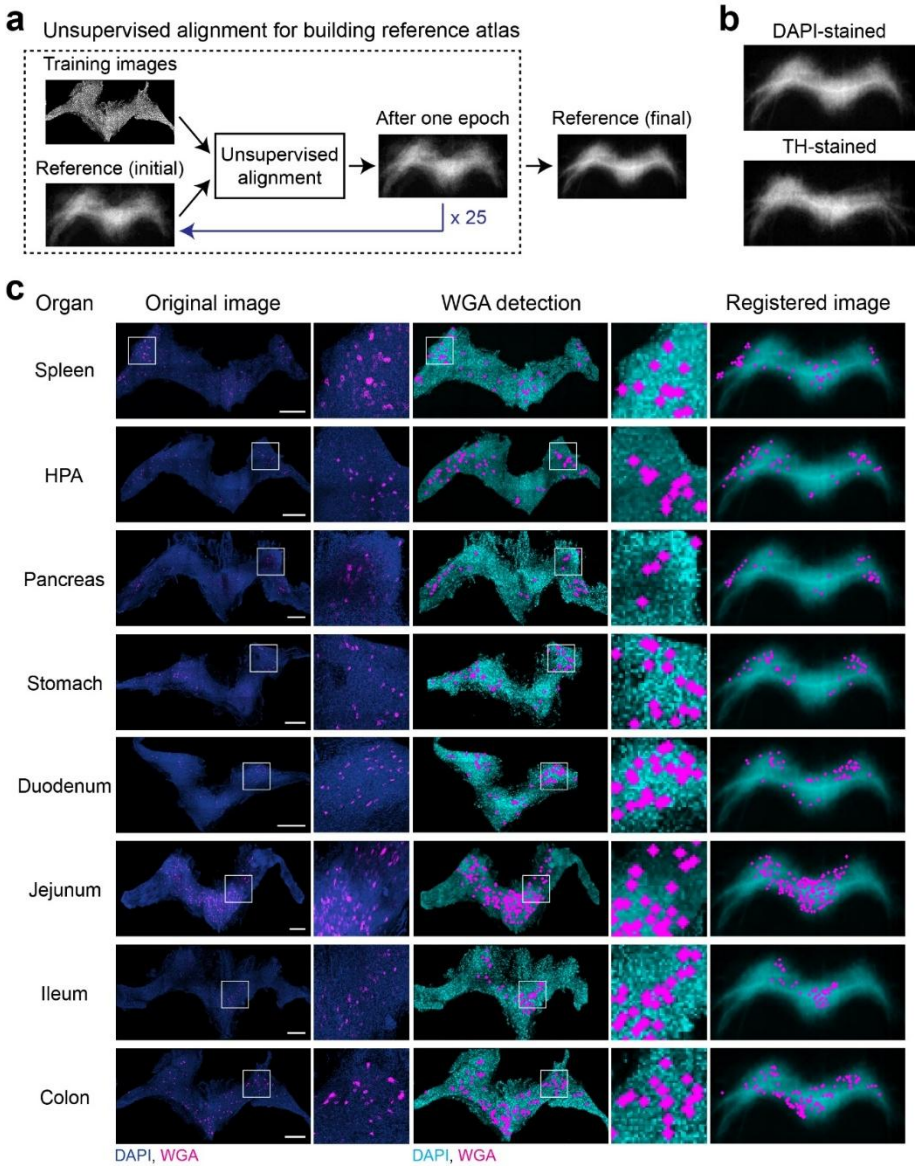

Extended Data Fig. 1 A computational pipeline for topographical mapping of visceral organs. a, A schematic for building reference atlas through unsupervised alignment processing. **b,** Two reference images generated from DAPI-stained (top) or TH-stained (bottom) training images. **c,** Representative original image, auto-detected and registered WGA-positive cells (magenta) with DAPI staining background (blue or cyan) for eight organ sites as indicated (n = 8 mice per group). Scale bar, 500 μm.

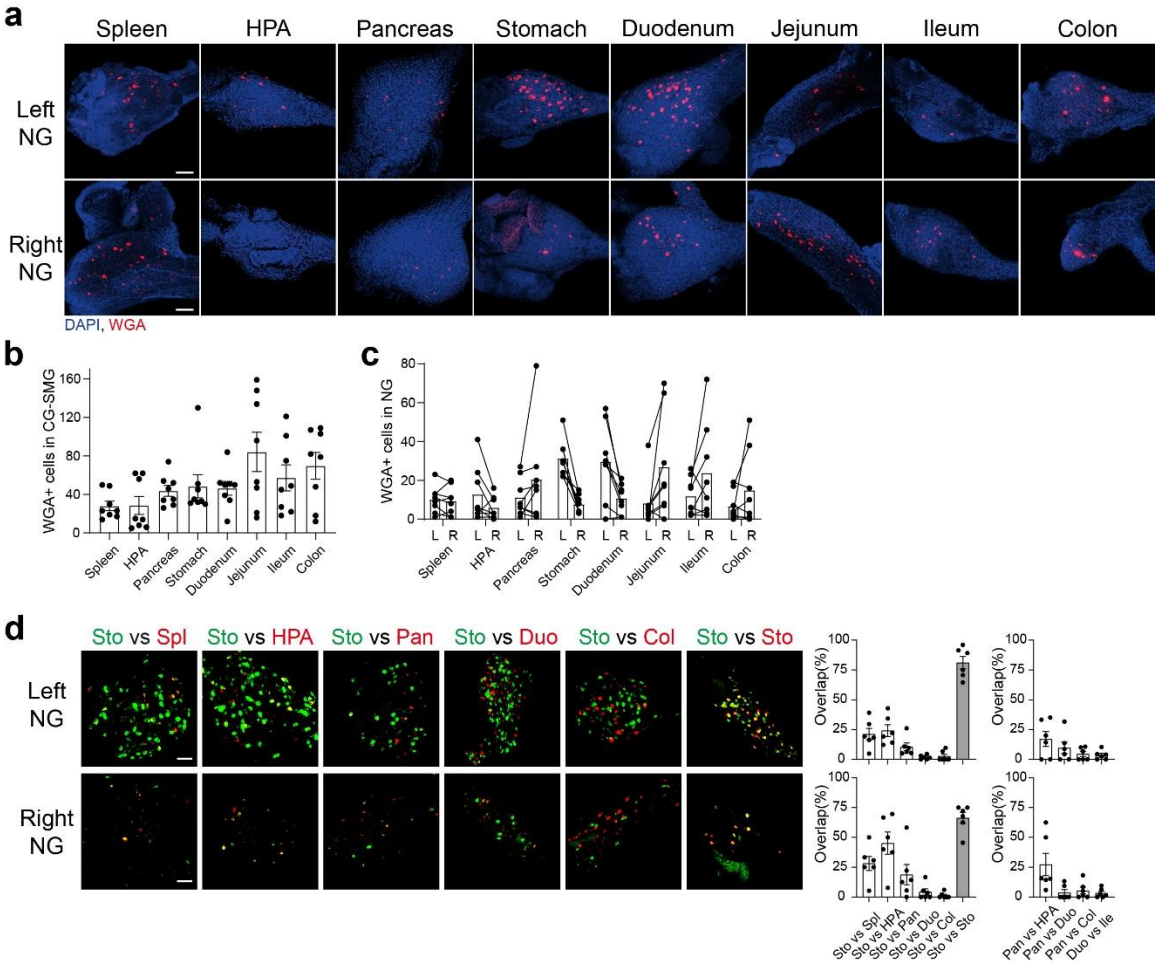

Extended Data Fig. 2 WGA retrograde tracing quantifications. a, Representative WGA-labeled cells (red) in the left and right nodose ganglia (NG) traced from the eight organ sites as indicated (n = 8 mice). **b, c,** Quantifications of WGA-positive cell number in the CG-SMG (**b**), left and right NG (**c**). **d,** Representative images and quantification of WGA-labeled cells in the left (top) and right (bottom) NG from dual-color organ tracing as indicated (n = 6 mice). Scale bar, 100 μm. Data are shown as mean ± s.e.m.

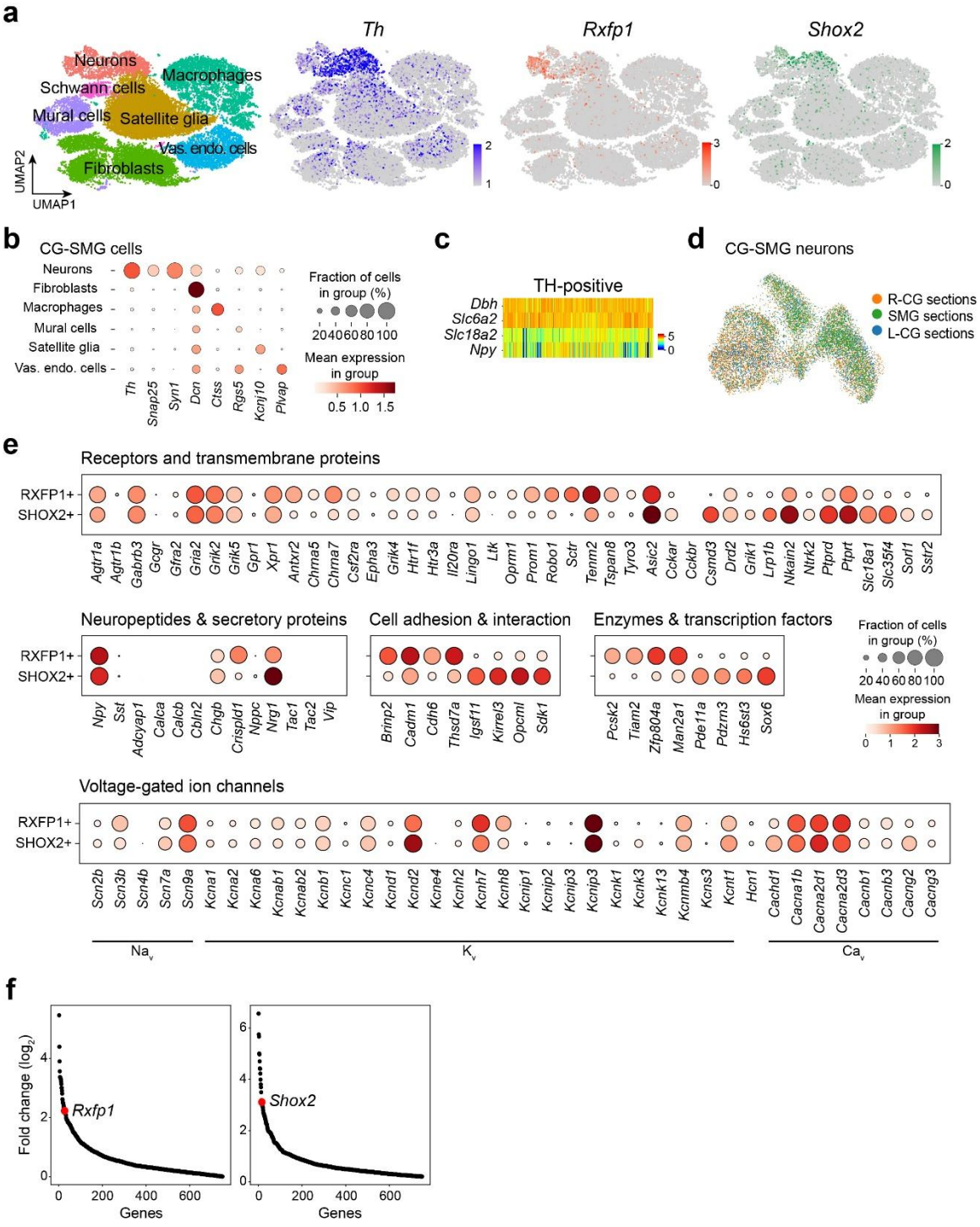

Extended Data Fig. 3 Multi-transcriptomic analyses of CG-SMG cells. a, ScRNA-seq analysis of CG-SMG cells. Left: UMAP embedding of CG-SMG major cell types (n = 24,873 cells). Vas. endo. cells, vascular endothelial cells. Middle and right: UMAP

embedding of log-normalized *Th* (blue), *Rxfp1* (red) and *Shox2* (green) expression. **b,** Dot plot of cell-type-specific expression in CG-SMG major cell classes from seqFISH dataset. Dot size is proportional to the percentage of cells with transcript count >0 expression. Color scale represents normalized average gene expression. **c,** Heatmap of sympathetic neuronal marker gene expression in CG-SMG neurons. **d,** UMAP embedded seqFISH data from different CG-SMG areas with Harmony integration (n = 13,105 cells). **e,** Gene expression comparison between RXFP1+ and SHOX2+ neurons. **f,** Differentially expressed genes in RXFP1+ and SHOX2+ neurons are ranked by their expression fold change ($\log_2$). *Rxfp1* and *Shox2* rank the top 27^{th} and 16^{th}, respectively.

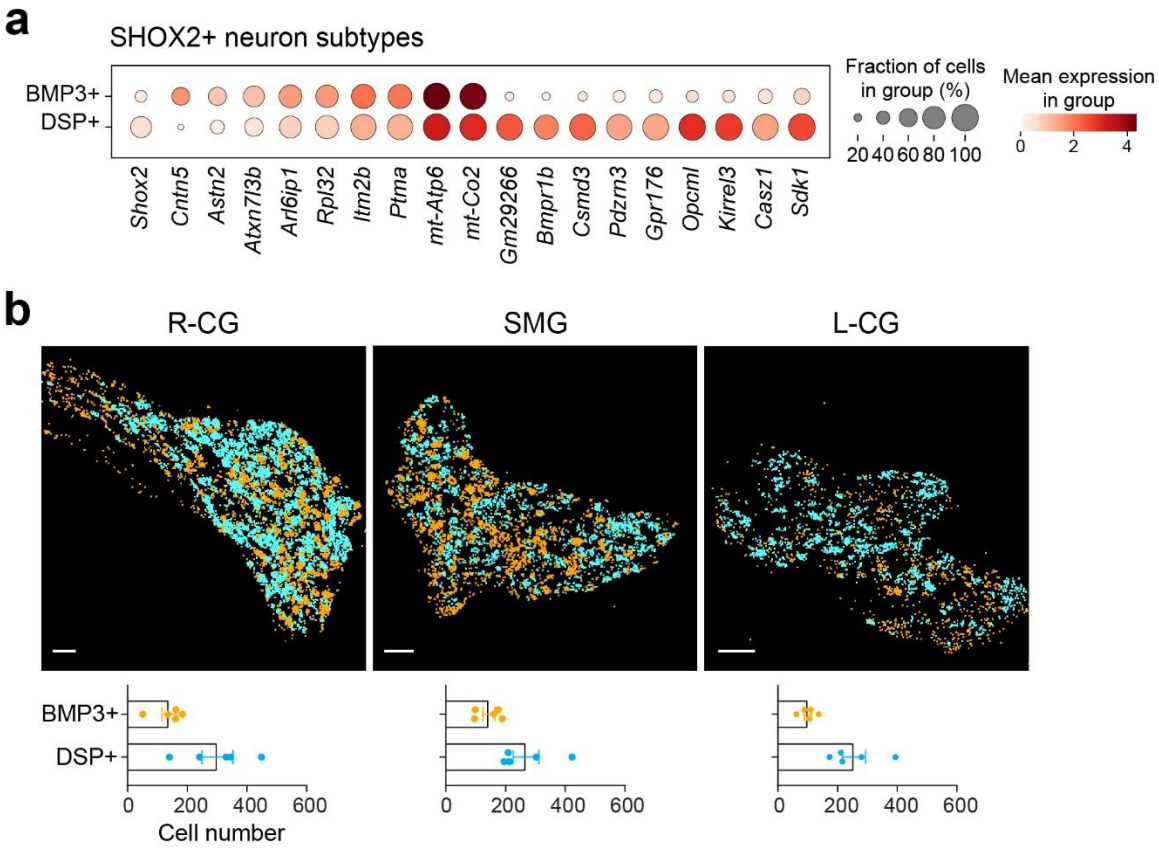

Extended Data Fig. 4 Transcriptomic and spatial analyses of SHOX2+ neuron subtypes. a, Dot plot of differential gene expression in CG-SMG^{BMP3} and CG-SMG^{DSP} neurons. **b,** Representative seqFISH images for the expression of *Bmp3* (orange) and *Dsp* (cyan) in CG-SMG areas (top) and quantification of BMP3- and DSP-positive neurons (bottom, n = 5 sections of 3 mice per R-CG, SMG, L-CG). Scale bar, 100 μm. Data are presented as mean ± s.e.m.

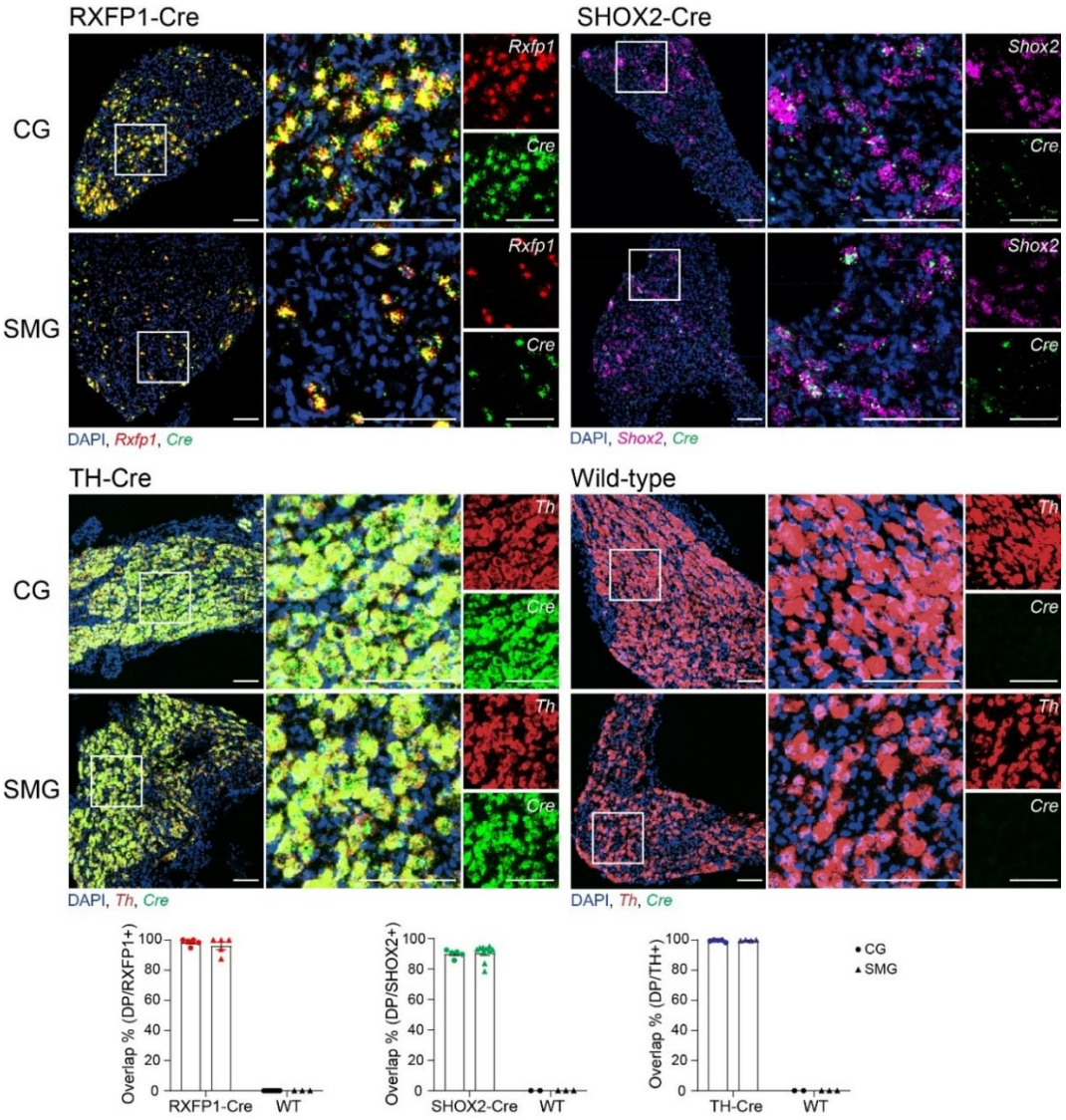

Extended Data Fig. 5 Two-color *in situ* hybridization for validating Cre expression of transgenic lines. Representative images of *Cre* and endogenous gene expression in the CG and SMG samples of RXFP1-Cre, SHOX2-Cre, TH-Cre and wild-type (WT) animals as indicated. Nuclei were visualized with DAPI staining (blue). Data were quantified from more than two mice per group. DP, double-positive. n = 5, 5, 8, 3 slices for RXFP1-Cre CG, RXFP1-Cre SMG, WT CG, and WT SMG. n = 5, 10, 2, 3 slices for SHOX2-Cre CG, SHOX2-Cre SMG, WT CG, and WT SMG. n = 5, 4, 2, 3 slices for TH-Cre CG, TH-Cre SMG, WT CG, and WT SMG. Scale bar, 100 μm. All data are shown as mean ± s.e.m.

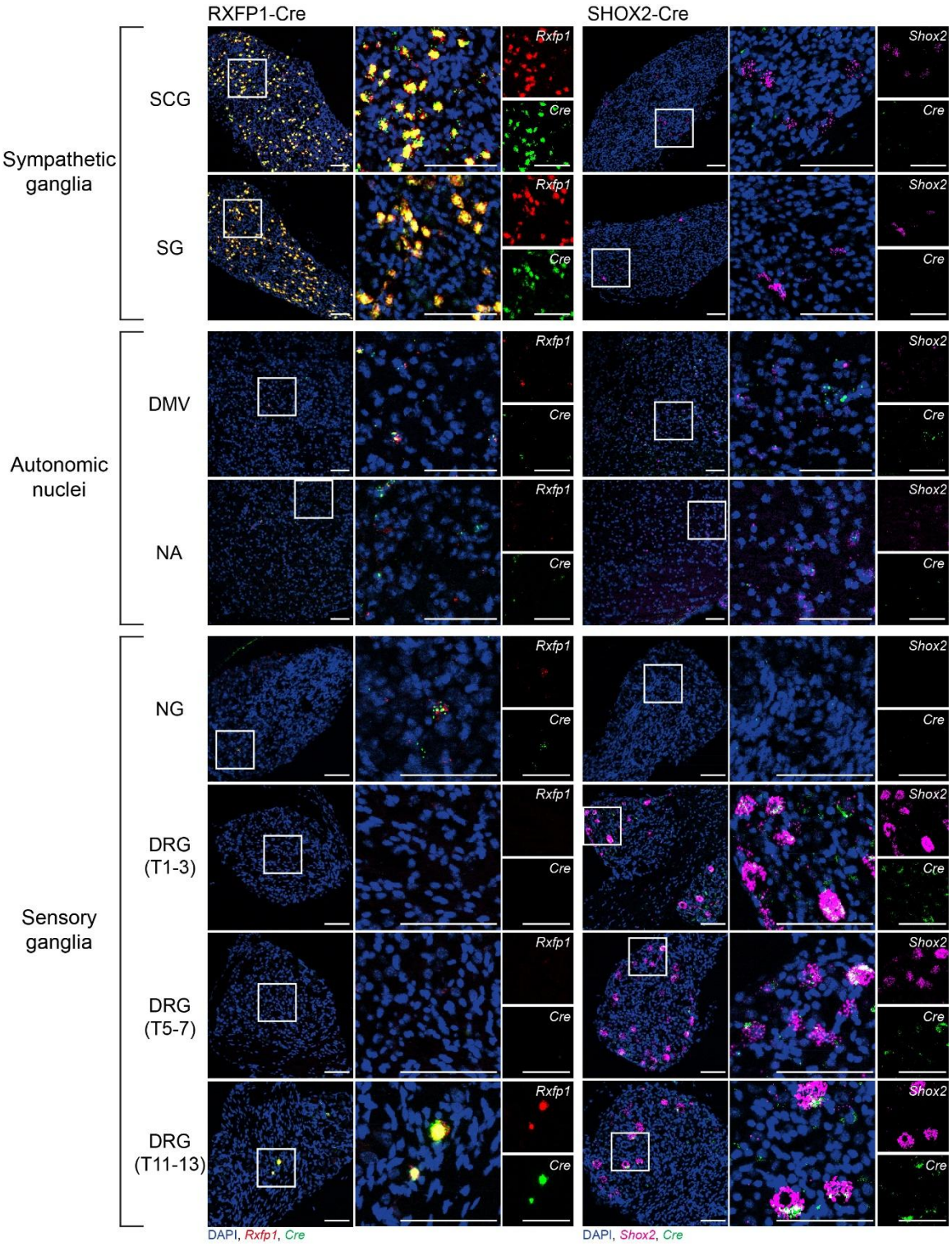
RXFP1-Cre
SHOX2-Cre
Sympathetic ganglia
SCG
SG
Autonomic nuclei
DMV
NA
Sensory ganglia
NG
DRG (T1-3)
DRG (T5-7)
DRG (T11-13)
Rxfp1
Cre
Shox2
DAPI, Rxfp1, Cre
DAPI, Shox2, Cre

Extended Data Fig. 6 Characterization Cre transgenic lines. Representative images of *Cre* and endogenous gene expression in different ganglia and brain nuclei of RXFP1-Cre and SHOX2-Cre animals as indicated. Nuclei were visualized by DAPI staining (blue). Data were collected from more than two mice per group. NG, nodose ganglion; DRG, dorsal root ganglion (T12 or T13); SCG, superior cervical ganglion; SG, stellate ganglion; DMV, dorsal motor nucleus of the vagus; NA, nucleus ambiguous. Scale bar, 100 μm.

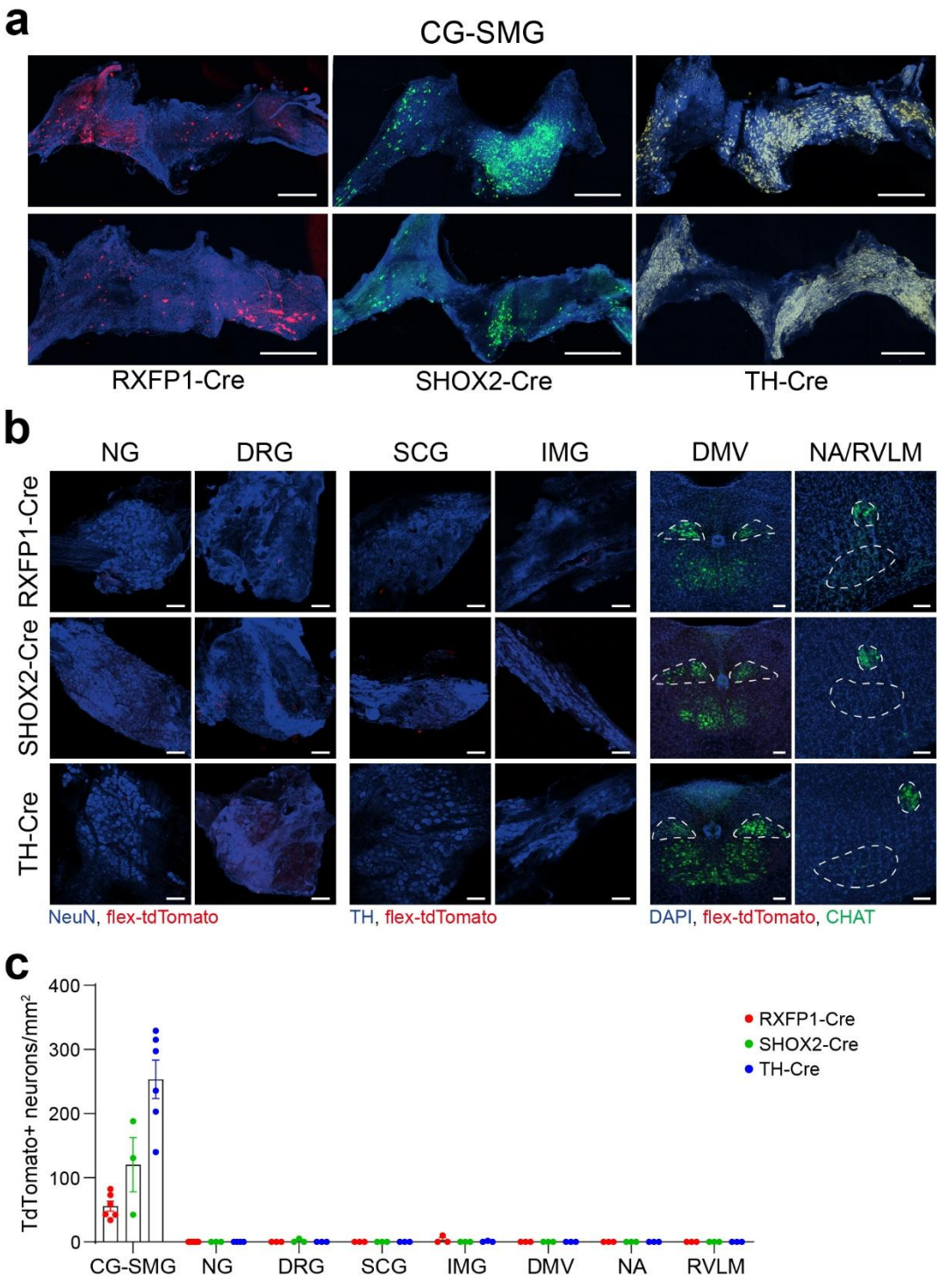

Extended Data Fig. 7 Histological verification for viral targeting. a, Representative CG-SMG images for RXFP1-, SHOX2-, and TH-targeted neurons by AAV-FLEX-

tdTomato with TH staining (blue). Scale bar, 500 μm. **b, c,** Histology (**b**) and quantification (**c**) for negative control of CG-SMG AAV injection. NG, nodose ganglion; DRG, dorsal root ganglion (T12 or T13); SCG, superior cervical ganglion; IMG, inferior mesenteric ganglion; DMV, dorsal motor nucleus of the vagus; NA, nucleus ambiguus; RVLM, rostral ventrolateral medulla. n = 6 RXFP1-Cre, 3 SHOX2-Cre, 6 TH-Cre mice for CG-SMG; 5 RXFP1-Cre, 3 SHOX2-Cre, 4 TH-Cre mice for NG. n = 3 animals per mouse line for the other sample groups. Scale bar, 100 μm. Data are presented as mean ± s.e.m.

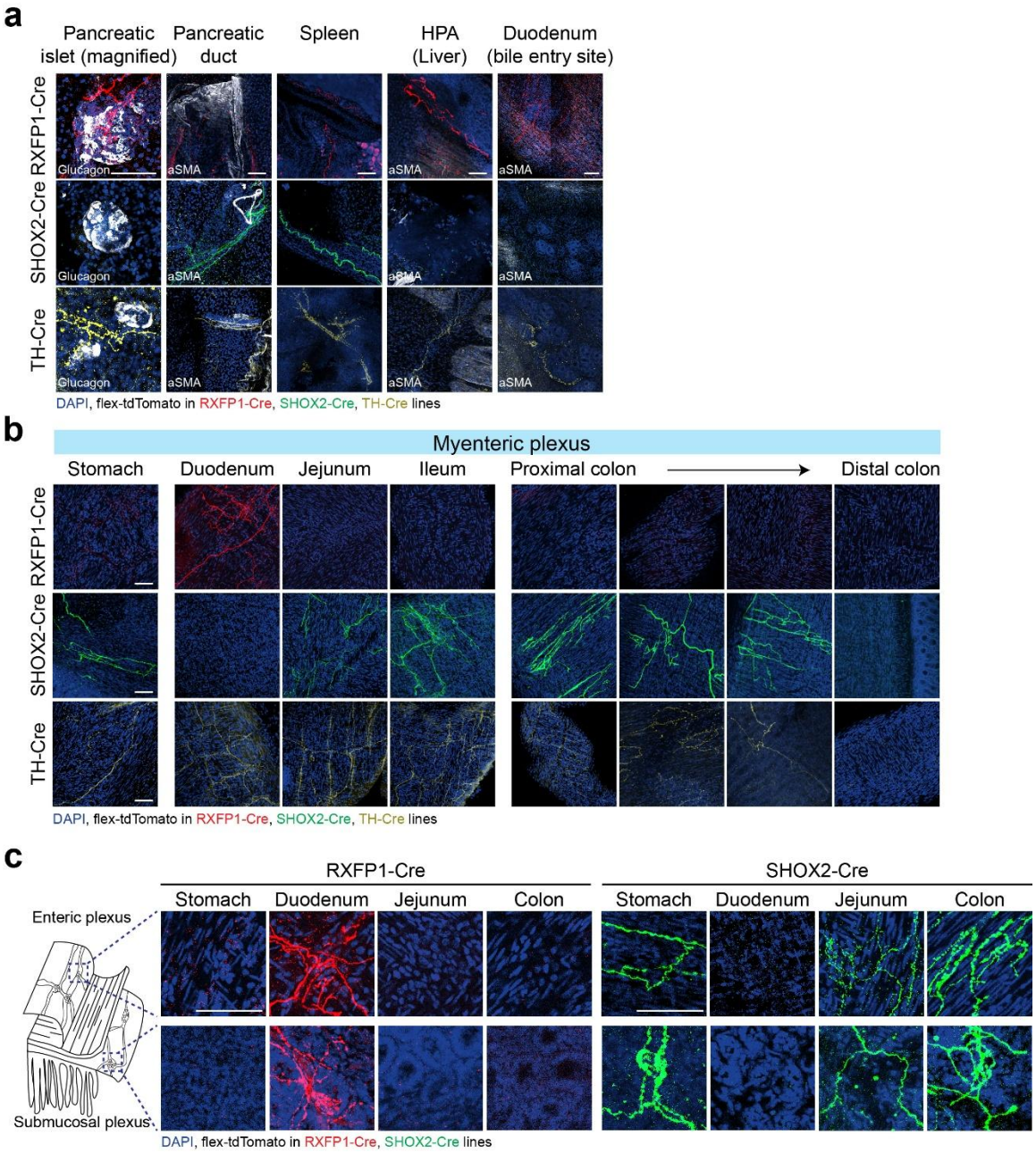

Extended Data Fig. 8 CG-SMG neural innervation of visceral organs. a, Representative images for whole-mount organ innervation of CG-SMG^{RXFP1}, CG-SMG^{SHOX2}, CG-SMGTH neurons. Glucagon or alpha smooth muscle actin (aSMA) staining is indicated on the images. Magnified images for the pancreatic islet are from **Fig.** 3b. **b,** Representative images for the innervation of the myenteric plexus on the GI tract. The same

set of animals were used as in **Fig.** 3b. **c,** Magnified images from **Fig.** 3b and Extended Data **Fig.** 9b for CG-SMG neural terminals in the myenteric and submucosal plexus along the GI tract. Nuclei were visualized by DAPI staining (blue). Scale bar, 100 μm.

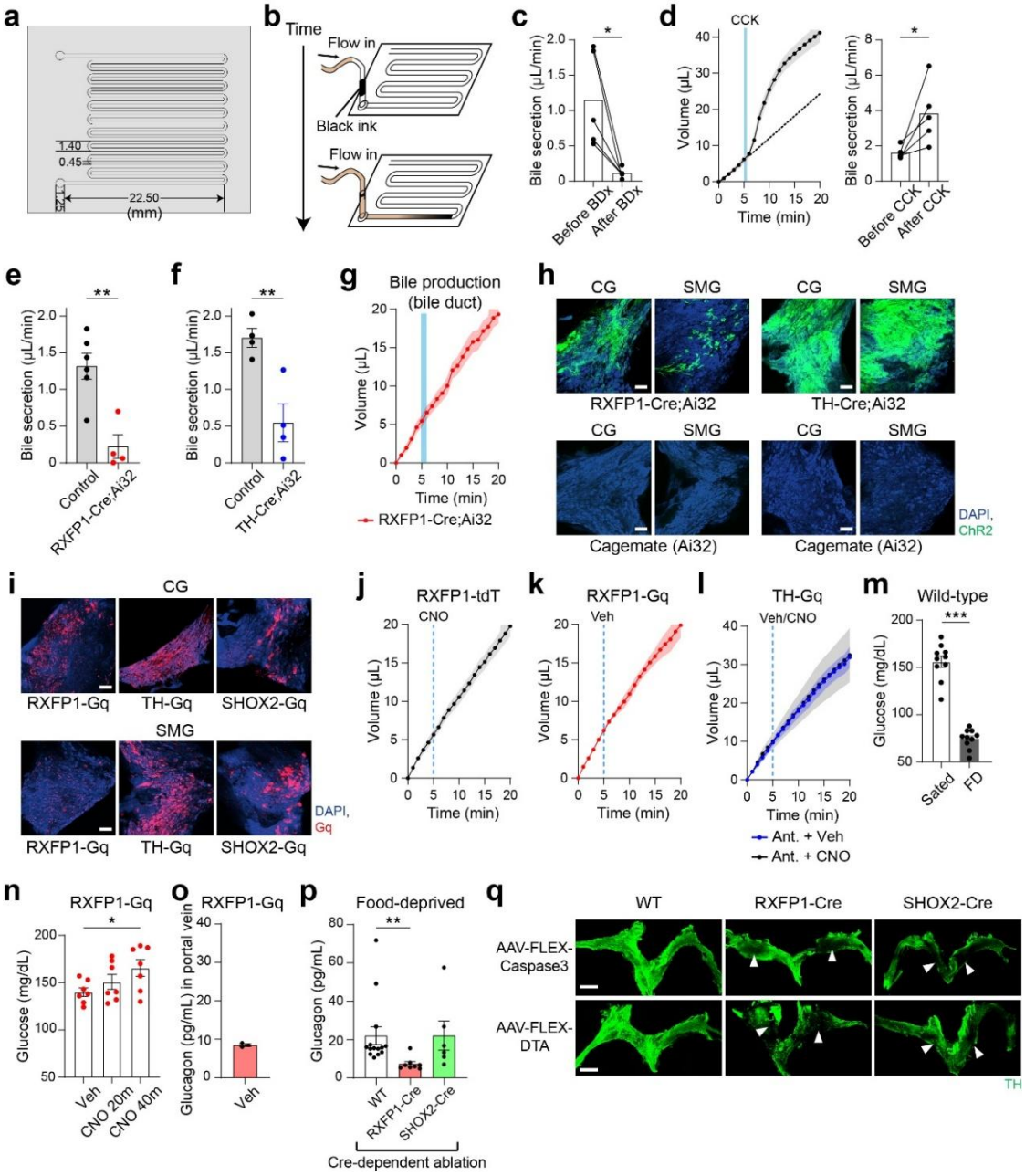

Extended Data Fig. 9 Measurements of secretory processes. a, A top-down view of the microfluidic device. **b,** A diagram of bile flow in the microfluidic chamber with tip stained by the black ink for automated fluid volume detection. **c,** Average bile flow rate before and after bile duct transection (BDx, n = 5 mice). **d,** Cholecystokinin (CCK) increased bile secretion (n = 5 mice). The dashed line is the linear regression fitted curve based on the initial 5 minutes of data. **e,f,** Quantified average bile flow rate after optogenetic activation

of (**e**) CG-SMG^{RXFP1} or (**f**) CG-SMGTH neurons (n = 4, 6 for RXFP1-Cre;Ai32, and cagemate control mice, dataset from **Fig.** 4e; n = 4, 4 for TH-Cre;Ai32, and cagemate control mice). **g,** When bile was measured directly from the bile duct instead of the duodenum, bile production rate was unchanged, regardless of CG-SMG^{RXFP1} neuron activation (n = 4 mice). Light pulses of 2 ms at 20 Hz were applied at CG-SMG for 1 min as indicated by the blue shade. **h, i,** Representative histological images for optogenetic (**h**) and chemogenetic (**i**) experiments as indicated. Robust ChR2-EYFP (green) or Gq-mCherry (red) expression was confirmed with sympathetic neuron marker TH staining (blue). Scale bar, 100 μm. **j,** The control group from **Fig.** 4f is plotted. **k,** Vehicle administration had no effects on bile secretion (n = 2 mice). **l,** Application of labetalol hydrochloride, a norepinephrine receptor antagonist (Ant.), abolished the inhibition effects of CG-SMG neurons on bile secretion (n = 4 mice per group). **m,** Systemic glucose level under sated and 24-hour food-deprived (FD) states (n = 10 mice each). **n,** Effects of activating CG-SMG^{RXFP1} neurons on glucose homeostasis. Systemic glucose level was measured 20 min after intraperitoneal PBS (Veh) injection, as well as 20 min (CNO 20m) or 40 min (CNO 40m) after intraperitoneal CNO administration (n = 7 mice). **o,** Vehicle administration had no effects on glucagon release (n = 3 mice). **p,** Functional necessity of CG-SMG neurons on glucagon release to the hepatic portal vein. Neurons were ablated using AAV-FLEX-Caspase3 or AAV-FLEX-DTA. Compared to wild-type control, RXFP1-ablated animals exhibited significantly lower glucagon levels under fasting state. SHOX2-ablated animals had intact glucagon release. n = 14 mice for WT, 8 mice for RXFP1-Cre, 6 mice for SHOX2-Cre groups. **q,** Representative histological confirmation for ablation experiments with TH antibody staining (green). Arrows point to regions with ablated cells. Scale bar, 500 μm. $^{*}P < 0.05$, $^{**}P < 0.01$, $^{***}P < 0.001$ by two-tailed paired or unpaired *t*-test, or one-way ANOVA with Dunnett's multiple comparisons test.

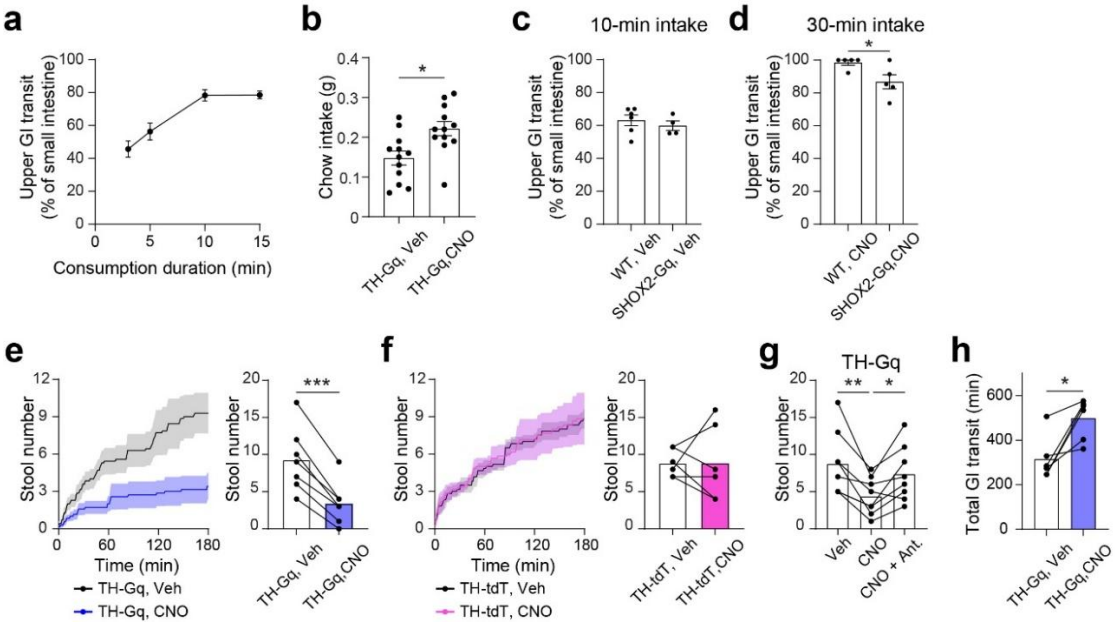

Extended Data Fig. 10 Measurements of GI transit. a, Quantification of colored food transit after different feeding durations as indicated (n = 5 mice per group). **b,** Chemogenetic activation of CG-SMGTH neurons increased food consumption within the initial 10-min feeding after deprivation (n = 12 mice). **c,** Vehicle administration had no effects on food transit (n = 6 mice for WT, and 4 mice for SHOX2-Gq groups). **d,** At 30-min time point, activating CG-SMG^{SHOX2} neurons significantly slower food transit compared to wild-type control animals (n = 5 mice per group). **e,** Inhibition effects of chemogenetic stimulation of CG-SMGTH neurons on stool expulsion. The number of stools after either intraperitoneal PBS (Veh) or CNO injection is plotted (left) and quantified (right, n = 7 mice). **f,** Spontaneous stool defecation of TH-Cre control animals with AAV-FLEX-tdTomato injection to CG-SMG (n = 6 mice). **g,** Chemogenetic stimulation of CG-SMGTH neurons significantly suppressed spontaneous stool expulsion, which was reversed by the application of labetalol hydrochloride (n = 8 mice). **h,** Chemogenetic activation of CG-SMGTH neurons significantly delayed the total GI transit (n = 6 mice). $^{*}P < 0.05$, $^{**}P < 0.01$, $^{***}P < 0.001$ by two-tailed paired *t*-test or one-way ANOVA with Dunnett's multiple comparisons test. Data are presented as mean ± s.e.m.

REFERENCES

1.Sammons, M. *et al.* Brain-body physiology: Local, reflex, and central communication. *Cell* **187**, 5877–5890 (2024).

2.Sternson, S. M. & Eiselt, A.-K. Three Pillars for the Neural Control of Appetite. *Annu Rev Physiol* **79**, 401–423 (2017).

3.Lin, E. E., Scott-Solomon, E. & Kuruvilla, R. Peripheral Innervation in the Regulation of Glucose Homeostasis. *Trends Neurosci* **44**, 189–202 (2021).

4.Wachsmuth, H. R., Weninger, S. N. & Duca, F. A. Role of the gut-brain axis in energy and glucose metabolism. *Exp Mol Med* **54**, 377–392 (2022).

5.Langhans, W., Watts, A. G. & Spector, A. C. The elusive cephalic phase insulin response: triggers, mechanisms, and functions. *Physiol Rev* **103**, 1423–1485 (2023).

6.Ml, A. & Bb, L. Toward a Wiring Diagram Understanding of Appetite Control. *Neuron* **95**, (2017).

7.Augustine, V., Lee, S. & Oka, Y. Neural Control and Modulation of Thirst, Sodium Appetite, and Hunger. *Cell* **180**, 25–32 (2020).

8.Abraira, V. E. & Ginty, D. D. The sensory neurons of touch. *Neuron* **79**, 618–639 (2013).

9.Travagli, R. A. & Anselmi, L. Vagal neurocircuitry and its influence on gastric motility. *Nat Rev Gastroenterol Hepatol* **13**, 389–401 (2016).

10.Yu, C. D., Xu, Q. J. & Chang, R. B. Vagal sensory neurons and gut-brain signaling. *Curr Opin Neurobiol* **62**, 133–140 (2020).

11.Kim, M., Heo, G. & Kim, S.-Y. Neural signalling of gut mechanosensation in ingestive and digestive processes. *Nat Rev Neurosci* **23**, 135–156 (2022).

12.Prescott, S. L. & Liberles, S. D. Internal senses of the vagus nerve. *Neuron* **110**, 579–599 (2022).

13.Barman, S. M. & Yates, B. J. Deciphering the Neural Control of Sympathetic Nerve Activity: Status Report and Directions for Future Research. *Front Neurosci* **11**, 730 (2017).

14.Langley, J. N. On the Regeneration of Pre-Ganglionic and of Post-Ganglionic Visceral Nerve Fibres. *The Journal of Physiology* **22**, 215–230 (1897).

15.Langley, J. N. *The Autonomic Nervous System (Pt. I)*. Pp. viii+, 80 (Heffer, Oxford, England, 1921).

16.Gibbons, C. H. Basics of autonomic nervous system function. *Handb Clin Neurol* **160**, 407–418 (2019).

17.Guyenet, P. G. The sympathetic control of blood pressure. *Nat Rev Neurosci* **7**, 335–346 (2006).

18.Goldstein, D. S. Differential responses of components of the autonomic nervous system. *Handb Clin Neurol* **117**, 13–22 (2013).

19.Nakamura, K., Nakamura, Y. & Kataoka, N. A hypothalamomedullary network for physiological responses to environmental stresses. *Nat Rev Neurosci* **23**, 35–52 (2022).

20.Gibbins, I. Functional organization of autonomic neural pathways. *Organogenesis* **9**, 169–175 (2013).

21.Jänig, W. & McLachlan, E. M. Characteristics of function-specific pathways in the sympathetic nervous system. *Trends Neurosci* **15**, 475–481 (1992).

22.Coverdell, T. C., Abbott, S. B. G. & Campbell, J. N. Molecular cell types as functional units of the efferent vagus nerve. *Seminars in Cell & Developmental Biology* **156**, 210–218 (2024).

23.Tao, J. *et al.* Highly selective brain-to-gut communication via genetically defined vagus neurons. *Neuron* **109**, 2106-2115.e4 (2021).

24.Veerakumar, A., Yung, A. R., Liu, Y. & Krasnow, M. A. Molecularly defined circuits for cardiovascular and cardiopulmonary control. *Nature* **606**, 739–746 (2022).

25.Mapps, A. A. *et al.* Diversity of satellite glia in sympathetic and sensory ganglia. *Cell Rep* **38**, 110328 (2022).

26.Sharma, S. *et al.* Tiered sympathetic control of cardiac function revealed by viral tracing and single cell transcriptome profiling. *Elife* **12**, e86295 (2023).

27.Ziegler, K. A. *et al.* Immune-mediated denervation of the pineal gland underlies sleep disturbance in cardiac disease. *Science* **381**, 285–290 (2023).

28.Wang, T., Teng, B., Yao, D. R., Gao, W. & Oka, Y. Organ-specific sympathetic innervation defines visceral functions. *Nature* **637**, 895–902 (2025).

29.Veerakumar, A., Yung, A. R., Liu, Y. & Krasnow, M. A. Molecularly defined circuits for cardiovascular and cardiopulmonary control. *Nature* **606**, 739–746 (2022).

30.Tao, J. *et al.* Highly selective brain-to-gut communication via genetically defined vagus neurons. *Neuron* **109**, 2106-2115.e4 (2021).

31.LeBouef, T., Yaker, Z. & Whited, L. Physiology, Autonomic Nervous System. in *StatPearls* (StatPearls Publishing, Treasure Island (FL), 2025).

32.Deuchars, S. A. & Lall, V. K. Sympathetic preganglionic neurons: properties and inputs. *Compr Physiol* **5**, 829–869 (2015).

33.Llewellyn-Smith, I. J. Sympathetic Preganglionic Neurons. in *Central Regulation of Autonomic Functions* (eds Llewellyn-Smith, I. J. & Verberne, A. J. M.) 0 (Oxford University Press, 2011). doi:10.1093/acprof:oso/9780195306637.003.0006.

34.Jordan, D. Parasympathetic Preganglionic Neurons. in *Central Regulation of Autonomic Functions* (eds Llewellyn-Smith, I. J. & Verberne, A. J. M.) 0 (Oxford University Press, 2011). doi:10.1093/acprof:oso/9780195306637.003.0007.

35.Langley, J. N. Sketch of the progress of discovery in the eighteenth century as regards the autonomic nervous system. *J Physiol* **50**, 225–258 (1916).

36.Reuss, S. & Moore, R. Y. Neuropeptide Y-containing neurons in the rat superior cervical ganglion: projections to the pineal gland. *J Pineal Res* **6**, 307–316 (1989).

37.Wojtkiewicz, J. *et al.* Immunohistochemical characterization of superior cervical ganglion neurons supplying porcine parotid salivary gland. *Neurosci Lett* **500**, 57–62 (2011).

38.Zhu, Y. *et al.* Sympathetic neuropeptide Y protects from obesity by sustaining thermogenic fat. *Nature* **634**, 243–250 (2024).

39.Uno, H. Sympathetic innervation of the sweat glands and piloarrector muscles of macaques and human beings. *J Invest Dermatol* **69**, 112–120 (1977).

40.van der Velden, V. H. & Hulsmann, A. R. Autonomic innervation of human airways: structure, function, and pathophysiology in asthma. *Neuroimmunomodulation* **6**, 145–159 (1999).

41.Zeisel, A. *et al.* Molecular Architecture of the Mouse Nervous System. *Cell* **174**, 999-1014.e22 (2018).

42.Ernsberger, U., Reissmann, E., Mason, I. & Rohrer, H. The expression of dopamine beta-hydroxylase, tyrosine hydroxylase, and Phox2 transcription factors in sympathetic neurons: evidence for common regulation during noradrenergic induction and diverging regulation later in development. *Mech Dev* **92**, 169–177 (2000).

43.Huesing, C. *et al.* Organization of sympathetic innervation of interscapular brown adipose tissue in the mouse. *J Comp Neurol* **530**, 1363–1378 (2022).

44.Goldstein, M., Fuxe, K. & Hökfelt, T. Characterization and tissue localization of catecholamine synthesizing enzymes. *Pharmacol Rev* **24**, 293–309 (1972).

45.Bohn, M. C., Goldstein, M. & Black, I. B. Expression of phenylethanolamine N-methyltransferase in rat sympathetic ganglia and extra-adrenal chromaffin tissue. *Dev Biol* **89**, 299–308 (1982).

46.Cahill, A. L., Eertmoed, A. L., Mangoura, D. & Perlman, R. L. Differential regulation of phenylethanolamine N-methyltransferase expression in two distinct subpopulations of bovine chromaffin cells. *J Neurochem* **67**, 1217–1224 (1996).

47.Peter, D. *et al.* Differential expression of two vesicular monoamine transporters. *J Neurosci* **15**, 6179–6188 (1995).

48.Schäfer, M. K., Schütz, B., Weihe, E. & Eiden, L. E. Target-independent cholinergic differentiation in the rat sympathetic nervous system. *Proc Natl Acad Sci U S A* **94**, 4149–4154 (1997).

49.Sieber-Blum, M. & Ren, Z. Norepinephrine transporter expression and function in noradrenergic cell differentiation. *Mol Cell Biochem* **212**, 61–70 (2000).

50.Li, Z., Caron, M. G., Blakely, R. D., Margolis, K. G. & Gershon, M. D. Dependence of Serotonergic and Other Nonadrenergic Enteric Neurons on Norepinephrine Transporter Expression. *J. Neurosci.* **30**, 16730–16740 (2010).

51.Pfeil, U. *et al.* Expression of the high-affinity choline transporter, CHT1, in the rat trachea. *Am J Respir Cell Mol Biol* **28**, 473–477 (2003).

52.Hoover, D. B., Ganote, C. E., Ferguson, S. M., Blakely, R. D. & Parsons, R. L. Localization of cholinergic innervation in guinea pig heart by immunohistochemistry for high-affinity choline transporters. *Cardiovascular Research* **62**, 112–121 (2004).

53.Okuda, T. & Haga, T. High-affinity choline transporter. *Neurochem Res* **28**, 483–488 (2003).

54.Chien, H.-J. *et al.* Human pancreatic afferent and efferent nerves: mapping and 3-D illustration of exocrine, endocrine, and adipose innervation. *Am J Physiol Gastrointest Liver Physiol* **317**, G694–G706 (2019).

55.Keast, J. R. Visualization and immunohistochemical characterization of sympathetic and parasympathetic neurons in the male rat major pelvic ganglion. *Neuroscience* **66**, 655–662 (1995).

56.Espinosa-Medina, I. *et al.* The sacral autonomic outflow is sympathetic. *Science* **354**, 893–897 (2016).

57.Horn, J. P. The sacral autonomic outflow is parasympathetic: Langley got it right. *Clin Auton Res* **28**, 181–185 (2018).

58.Brumovsky, P. R. Dorsal root ganglion neurons and tyrosine hydroxylase – An intriguing association with implications for sensation and pain. *Pain* **157**, 314–320 (2016).

59.Wang, Y. *et al.* The role of somatosensory innervation of adipose tissues. *Nature* **609**, 569–574 (2022).

60.Lin, Y. S., Nosaka, S., Amakata, Y. & Maeda, T. Comparative study of the mammalian liver innervation: an immunohistochemical study of protein gene product 9.5, dopamine beta-hydroxylase and tyrosine hydroxylase. *Comp Biochem Physiol A Physiol* **110**, 289–298 (1995).

61.Parker, T. L., Kesse, W. K., Mohamed, A. A. & Afework, M. The innervation of the mammalian adrenal gland. *J Anat* **183**, 265–276 (1993).

62.McDougal, D. H. & Gamlin, P. D. Autonomic control of the eye. *Compr Physiol* **5**, 439–473 (2015).

63.Li, Y. & Dahlström, A. Peripheral projections of NESP55 containing neurons in the rat sympathetic ganglia. *Auton Neurosci* **141**, 1–9 (2008).

64.Jin, K. *et al.* Identification of Lacrimal Gland Postganglionic Innervation and Its Regulation of Tear Secretion. *Am J Pathol* **190**, 1068–1079 (2020).

65.Kummer, W., Fischer, A., Kurkowski, R. & Heym, C. The sensory and sympathetic innervation of guinea-pig lung and trachea as studied by retrograde neuronal tracing and double-labelling immunohistochemistry. *Neuroscience* **49**, 715–737 (1992).

66.Rajendran, P. S. *et al.* Identification of peripheral neural circuits that regulate heart rate using optogenetic and viral vector strategies. *Nat Commun* **10**, 1944 (2019).

67.Barrett, M. S., Hegarty, D. M., Habecker, B. A. & Aicher, S. A. Distinct morphology of cardiac- and brown adipose tissue-projecting neurons in the stellate ganglia of mice. *Physiol Rep* **10**, e15334 (2022).

68.Kuntz, A. & Jacobs, M. W. Components of periarterial extensions of celiac and mesenteric plexuses. *Anat Rec* **123**, 509–520 (1955).

69.Quinson, N., Robbins, H. L., Clark, M. J. & Furness, J. B. Locations and innervation of cell bodies of sympathetic neurons projecting to the gastrointestinal tract in the rat. *Arch Histol Cytol* **64**, 281–294 (2001).

70.Liu, K. *et al.* Metabolic stress drives sympathetic neuropathy within the liver. *Cell Metab* **33**, 666-675.e4 (2021).

71.Ding, X. *et al.* Panicle-Shaped Sympathetic Architecture in the Spleen Parenchyma Modulates Antibacterial Innate Immunity. *Cell Rep* **27**, 3799-3807.e3 (2019).

72.Smith-Edwards, K. M. *et al.* Sympathetic Input to Multiple Cell Types in Mouse and Human Colon Produces Region-Specific Responses. *Gastroenterology* **160**, 1208-1223.e4 (2021).

73.Mazur, U., Lepiarczyk, E., Janikiewicz, P. & Bossowska, A. Somatostatin immunoreactivity within the urinary bladder nerve fibers and paracervical ganglion urinary bladder projecting neurons in the female pig. *J Chem Neuroanat* **117**, 102007 (2021).

74.Osborn, J. W., Tyshynsky, R. & Vulchanova, L. Function of Renal Nerves in Kidney Physiology and Pathophysiology. *Annu Rev Physiol* **83**, 429–450 (2021).

75.Torres, H. *et al.* Sympathetic innervation of the mouse kidney and liver arising from prevertebral ganglia. *Am J Physiol Regul Integr Comp Physiol* **321**, R328–R337 (2021).

76.François, M. *et al.* Sympathetic innervation of the interscapular brown adipose tissue in mouse. *Ann N Y Acad Sci* **1454**, 3–13 (2019).

77.Huesing, C. *et al.* Sympathetic innervation of inguinal white adipose tissue in the mouse. *J Comp Neurol* **529**, 1465–1485 (2021).

78.Vera, P. L., Haase, E. B. & Schramm, L. P. Origins of the sympathetic innervation of the cervical end of the uterus in the rat. *Brain Res* **747**, 140–143 (1997).

79.Houdeau, E., Rousseau, A., Meusnier, C., Prud'Homme, M. J. & Rousseau, J. P. Sympathetic innervation of the upper and lower regions of the uterus and cervix in the rat have different origins and routes. *J Comp Neurol* **399**, 403–412 (1998).

80.Tamamaki, N. & Nojyo, Y. Intracranial trajectories of sympathetic nerve fibers originating in the superior cervical ganglion in the rat: WGA-HRP anterograde labeling study. *Brain Res* **437**, 387–392 (1987).

81.Hirakawa, N., Morimoto, M. & Totoki, T. Sympathetic innervation of the young canine heart using antero- and retrograde axonal tracer methods. *Brain Res Bull* **31**, 673–680 (1993).

82.Demer, J. L., Poukens, V., Miller, J. M. & Micevych, P. Innervation of extraocular pulley smooth muscle in monkeys and humans. *Invest Ophthalmol Vis Sci* **38**, 1774–1785 (1997).

83.Beckers, H. J., Klooster, J., Vrensen, G. F. & Lamers, W. P. Facial parasympathetic innervation of the rat choroid, lacrimal glands and ciliary ganglion. An ultrastructural pterygopalatine tracing and immunohistochemical study. *Ophthalmic Res* **25**, 319–330 (1993).

84.van der Werf, F., Baljet, B., Prins, M. & Otto, J. A. Innervation of the lacrimal gland in the cynomolgous monkey: a retrograde tracing study. *J Anat* **188 (Pt 3)**, 591–601 (1996).

85.Dartt, D. A. Neural regulation of lacrimal gland secretory processes: relevance in dry eye diseases. *Prog Retin Eye Res* **28**, 155–177 (2009).

86.Sheu, S.-H., Tapia, J. C., Tsuriel, S. & Lichtman, J. W. Similar synapse elimination motifs at successive relays in the same efferent pathway during development in mice. *Elife* **6**, e23193 (2017).

87.Zubair, A. & Khan, Y. S. Neuroanatomy, Otic Ganglion. in *StatPearls* (StatPearls Publishing, Treasure Island (FL), 2025).

88.Kalia, M. & Sullivan, J. M. Brainstem projections of sensory and motor components of the vagus nerve in the rat. *J Comp Neurol* **211**, 248–265 (1982).

89.Fox, E. A. & Powley, T. L. Longitudinal columnar organization within the dorsal motor nucleus represents separate branches of the abdominal vagus. *Brain Res* **341**, 269–282 (1985).

90.Bieger, D. & Hopkins, D. A. Viscerotopic representation of the upper alimentary tract in the medulla oblongata in the rat: the nucleus ambiguus. *J Comp Neurol* **262**, 546–562 (1987).

91.Dergacheva, O., Griffioen, K. J., Neff, R. A. & Mendelowitz, D. Respiratory modulation of premotor cardiac vagal neurons in the brainstem. *Respir Physiol Neurobiol* **174**, 102–110 (2010).

92.Browning, K. N., Coleman, F. H. & Travagli, R. A. Characterization of pancreas-projecting rat dorsal motor nucleus of vagus neurons. *Am J Physiol Gastrointest Liver Physiol* **288**, G950-955 (2005).

93.Wang, L. & Taché, Y. The parasympathetic and sensory innervation of the proximal and distal colon in male mice. *Front Neuroanat* **18**, 1422403 (2024).

94.Gourine, A. V. & Ackland, G. L. Cardiac Vagus and Exercise. *Physiology (Bethesda)* **34**, 71–80 (2019).

95.Moreira, T. S., Antunes, V. R., Falquetto, B. & Marina, N. Long-term stimulation of cardiac vagal preganglionic neurons reduces blood pressure in the spontaneously hypertensive rat. *J Hypertens* **36**, 2444–2452 (2018).

96.Fonseca, R. C. *et al.* Vagus nerve regulates the phagocytic and secretory activity of resident macrophages in the liver. *Brain Behav Immun* **81**, 444–454 (2019).

97.Machhada, A. *et al.* Optogenetic Stimulation of Vagal Efferent Activity Preserves Left Ventricular Function in Experimental Heart Failure. *JACC Basic Transl Sci* **5**, 799–810 (2020).

98.Dyavanapalli, J. Novel approaches to restore parasympathetic activity to the heart in cardiorespiratory diseases. *Am J Physiol Heart Circ Physiol* **319**, H1153–H1161 (2020).

99.Zasadny, F. M., Dyavanapalli, J., Dowling, N. M., Mendelowitz, D. & Kay, M. W. Cholinergic stimulation improves electrophysiological rate adaptation during pressure overload-induced heart failure in rats. *Am J Physiol Heart Circ Physiol* **319**, H1358–H1368 (2020).

100.Strain, M. M. *et al.* Dorsal motor vagal neurons can elicit bradycardia and reduce anxiety-like behavior. *iScience* **27**, 109137 (2024).

101.Burnstock, G. Innervation of bladder and bowel. *Ciba Found Symp* **151**, 2–18; discussion 18-26 (1990).

102.de Groat, W. C., Griffiths, D. & Yoshimura, N. Neural control of the lower urinary tract. *Compr Physiol* **5**, 327–396 (2015).

103.Sharabi, A. F. & Carey, F. J. Anatomy, Abdomen and Pelvis, Splanchnic Nerves. in *StatPearls* (StatPearls Publishing, Treasure Island (FL), 2025).

104.Kobori, N., Moore, A. N., Redell, J. B. & Dash, P. K. Caudal DMN neurons innervate the spleen and release CART peptide to regulate neuroimmune function. *J Neuroinflammation* **20**, 158 (2023).

105.Anderson, C., McKinley, M., Martelli, D. & McAllen, R. Letter to the editor: Parasympathetic innervation of the rodent spleen? *Am J Physiol Heart Circ Physiol* **309**, H2158 (2015).

106.Gautron, L. The parasympathetic innervation of the spleen: are we chasing a ghost? *J Anat* **240**, 772–774 (2022).

107.Norvell, J. E. & Anderson, J. M. Assessment of possible parasympathetic innervation of the kidney. *J Auton Nerv Syst* **8**, 291–294 (1983).

108.Cheng, X. *et al.* Anatomical Evidence for Parasympathetic Innervation of the Renal Vasculature and Pelvis. *J Am Soc Nephrol* **33**, 2194–2210 (2022).

109.N'Guetta, P.-E. Y. *et al.* Comprehensive mapping of sensory and sympathetic innervation of the developing kidney. *Cell Rep* **43**, 114860 (2024).

110.Gibbins, I. L. Vasoconstrictor, vasodilator and pilomotor pathways in sympathetic ganglia of guinea-pigs. *Neuroscience* **47**, 657–672 (1992).

111.Gordan, R., Gwathmey, J. K. & Xie, L.-H. Autonomic and endocrine control of cardiovascular function. *World J Cardiol* **7**, 204–214 (2015).

112.Gibbins, I. L. Vasomotor, pilomotor and secretomotor neurons distinguished by size and neuropeptide content in superior cervical ganglia of mice. *J Auton Nerv Syst* **34**, 171–183 (1991).

113.Li, C. & Horn, J. P. Physiological classification of sympathetic neurons in the rat superior cervical ganglion. *J Neurophysiol* **95**, 187–195 (2006).

114.Izumi, H. Reflex parasympathetic vasodilatation in facial skin. *Gen Pharmacol* **26**, 237–244 (1995).

115.Canning, B. J. Reflex regulation of airway smooth muscle tone. *J Appl Physiol (1985)* **101**, 971–985 (2006).

116.Proctor, G. B. & Carpenter, G. H. Regulation of salivary gland function by autonomic nerves. *Auton Neurosci* **133**, 3–18 (2007).

117.Martinez-Sanchez, N. *et al.* The sympathetic nervous system in the 21st century: Neuroimmune interactions in metabolic homeostasis and obesity. *Neuron* **110**, 3597–3626 (2022).

118.Ren, W., Hua, M., Cao, F. & Zeng, W. The Sympathetic-Immune Milieu in Metabolic Health and Diseases: Insights from Pancreas, Liver, Intestine, and Adipose Tissues. *Adv Sci (Weinh)* **11**, e2306128 (2024).

119.Udit, S., Blake, K. & Chiu, I. M. Somatosensory and autonomic neuronal regulation of the immune response. *Nat Rev Neurosci* **23**, 157–171 (2022).

120.Klein Wolterink, R. G. J., Wu, G. S., Chiu, I. M. & Veiga-Fernandes, H. Neuroimmune Interactions in Peripheral Organs. *Annu Rev Neurosci* **45**, 339–360 (2022).

121.Hanoun, M., Maryanovich, M., Arnal-Estapé, A. & Frenette, P. S. Neural regulation of hematopoiesis, inflammation, and cancer. *Neuron* **86**, 360–373 (2015).

122.Shwartz, Y. *et al.* Cell Types Promoting Goosebumps Form a Niche to Regulate Hair Follicle Stem Cells. *Cell* **182**, 578-593.e19 (2020).

123.Zhang, B. & Chen, T. Local and systemic mechanisms that control the hair follicle stem cell niche. *Nat Rev Mol Cell Biol* **25**, 87–100 (2024).

124.Niu, X. *et al.* Mapping of Extrinsic Innervation of the Gastrointestinal Tract in the Mouse Embryo. *J Neurosci* **40**, 6691–6708 (2020).

125.Guillot, J. *et al.* Sympathetic axonal sprouting induces changes in macrophage populations and protects against pancreatic cancer. *Nat Commun* **13**, 1985 (2022).

126.Salamon, R. J. *et al.* Parasympathetic and sympathetic axons are bundled in the cardiac ventricles and undergo physiological reinnervation during heart regeneration. *iScience* **26**, 107709 (2023).

127.Liu, S. *et al.* Somatotopic Organization and Intensity Dependence in Driving Distinct NPY-Expressing Sympathetic Pathways by Electroacupuncture. *Neuron* **108**, 436-450.e7 (2020).

128.Kumari, R. *et al.* Sympathetic NPY controls glucose homeostasis, cold tolerance, and cardiovascular functions in mice. *Cell Reports* **43**, (2024).

129.Sharkey, K. A., Williams, R. G. & Dockray, G. J. Sensory substance P innervation of the stomach and pancreas. Demonstration of capsaicin-sensitive sensory neurons in the rat by combined immunohistochemistry and retrograde tracing. *Gastroenterology* **87**, 914–921 (1984).

130.Quinson, N., Robbins, H. L., Clark, M. J. & Furness, J. B. Locations and innervation of cell bodies of sympathetic neurons projecting to the gastrointestinal tract in the rat. *Arch Histol Cytol* **64**, 281–294 (2001).

131.Torres, H. *et al.* Sympathetic innervation of the mouse kidney and liver arising from prevertebral ganglia. *Am J Physiol Regul Integr Comp Physiol* **321**, R328–R337 (2021).

132.Chan, K. L., Poller, W. C., Swirski, F. K. & Russo, S. J. Central regulation of stress-evoked peripheral immune responses. *Nat Rev Neurosci* **24**, 591–604 (2023).

133.Scott-Solomon, E., Boehm, E. & Kuruvilla, R. The sympathetic nervous system in development and disease. *Nat Rev Neurosci* **22**, 685–702 (2021).

134.Muller, P. A. *et al.* Microbiota modulate sympathetic neurons via a gut-brain circuit. *Nature* **583**, 441–446 (2020).

135.Eng, C.-H. L. *et al.* Transcriptome-scale super-resolved imaging in tissues by RNA seqFISH+. *Nature* **568**, 235–239 (2019).

136.Furlan, A. *et al.* Visceral motor neuron diversity delineates a cellular basis for nipple- and pilo-erection muscle control. *Nat Neurosci* **19**, 1331–1340 (2016).

137.Mapps, A. A. *et al.* Diversity of satellite glia in sympathetic and sensory ganglia. *Cell Rep* **38**, 110328 (2022).

138.Lindh, B. *et al.* Topography of NPY-, somatostatin-, and VIP-immunoreactive, neuronal subpopulations in the guinea pig celiac-superior mesenteric ganglion and their projection to the pylorus. *J Neurosci* **6**, 2371–2383 (1986).

139.Lindh, B., Hökfelt, T. & Elfvin, L. G. Distribution and origin of peptide-containing nerve fibers in the celiac superior mesenteric ganglion of the guinea-pig. *Neuroscience* **26**, 1037–1071 (1988).

140.Miolan, J. P. & Niel, J. P. The mammalian sympathetic prevertebral ganglia: integrative properties and role in the nervous control of digestive tract motility. *J Auton Nerv Syst* **58**, 125–138 (1996).

141.Kaestner, C. L., Smith, E. H., Peirce, S. G. & Hoover, D. B. Immunohistochemical analysis of the mouse celiac ganglion: An integrative relay station of the peripheral nervous system. *J Comp Neurol* **527**, 2742–2760 (2019).

142.Sun, C., Zhang, T., Liu, C., Gu, S. & Chen, Y. Generation of Shox2-Cre allele for tissue specific manipulation of genes in the developing heart, palate, and limb. *Genesis* **51**, 515–522 (2013).

143.Hama, H. *et al.* ScaleS: an optical clearing palette for biological imaging. *Nat Neurosci* **18**, 1518–1529 (2015).

144.Browning, K. N. & Travagli, R. A. Central Nervous System Control of Gastrointestinal Motility and Secretion and Modulation of Gastrointestinal Functions. *Compr Physiol* **4**, 1339–1368 (2014).

145.Beckh, K. & Arnold, R. Regulation of bile secretion by sympathetic nerves in perfused rat liver. *Am J Physiol* **261**, G775-780 (1991).

146.Ali, A. E., Rutishauser, S. C. & Case, R. M. Pancreatic and biliary secretion in the anesthetized Syrian golden hamster in response to secretin, cholecystokinin-octapeptide, bombesin, and carbachol. *Pancreas* **5**, 314–322 (1990).

147.Marliss, E. B. *et al.* Glucagon release induced by pancreatic nerve stimulation in the dog. *J Clin Invest* **52**, 1246–1259 (1973).

148.Ahrén, B., Veith, R. C. & Taborsky, G. J. Sympathetic nerve stimulation versus pancreatic norepinephrine infusion in the dog: 1). Effects on basal release of insulin and glucagon. *Endocrinology* **121**, 323–331 (1987).

149.Rao, M. & Gershon, M. D. The bowel and beyond: the enteric nervous system in neurological disorders. *Nat Rev Gastroenterol Hepatol* **13**, 517–528 (2016).

150.Servin-Vences, M. R. *et al.* PIEZO2 in somatosensory neurons controls gastrointestinal transit. *Cell* **186**, 3386-3399.e15 (2023).

151.Chang, R. B., Strochlic, D. E., Williams, E. K., Umans, B. D. & Liberles, S. D. Vagal Sensory Neuron Subtypes that Differentially Control Breathing. *Cell* **161**, 622–633 (2015).

152.Wolfson, R. L. *et al.* DRG afferents that mediate physiologic and pathologic mechanosensation from the distal colon. *Cell* **186**, 3368-3385.e18 (2023).

153.Cannon, W. B. *The Wisdom of the Body, 2nd Ed*. (Norton & Co., Oxford, England, 1939).

154.Seals, D. R. & Victor, R. G. Regulation of muscle sympathetic nerve activity during exercise in humans. *Exerc Sport Sci Rev* **19**, 313–349 (1991).

155.Morrison, S. F. Differential control of sympathetic outflow. *American Journal of Physiology-Regulatory, Integrative and Comparative Physiology* **281**, R683–R698 (2001).

156.Gonsalvez, D. G., Kerman, I. A., McAllen, R. M. & Anderson, C. R. Chemical Coding for Cardiovascular Sympathetic Preganglionic Neurons in Rats. *J Neurosci* **30**, 11781–11791 (2010).

157.Wang, M., Wang, Q. & Whim, M. D. Fasting induces a form of autonomic synaptic plasticity that prevents hypoglycemia. *Proc Natl Acad Sci U S A* **113**, E3029–E3038 (2016).

158.Pool, A.-H. *et al.* The cellular basis of distinct thirst modalities. *Nature* **588**, 112–117 (2020).

159.VoxelMorph: A Learning Framework for Deformable Medical Image Registration | IEEE Journals & Magazine | IEEE Xplore. https://ieeexplore.ieee.org/document/8633930.

160.Dalca, A., Rakic, M., Guttag, J. & Sabuncu, M. Learning Conditional Deformable Templates with Convolutional Networks. in *Advances in Neural Information Processing Systems* vol. 32 (Curran Associates, Inc., 2019).

161.Carrier, G. O. & Ikeda, S. R. TTX-sensitive Na+ channels and Ca2+ channels of the L- and N-type underlie the inward current in acutely dispersed coeliac-mesenteric ganglia neurons of adult rats. *Pflugers Arch* **421**, 7–16 (1992).

162.Pool, A.-H., Poldsam, H., Chen, S., Thomson, M. & Oka, Y. Recovery of missing single-cell RNA-sequencing data with optimized transcriptomic references. *Nat Methods* **20**, 1506–1515 (2023).

163.Wolf, F. A., Angerer, P. & Theis, F. J. SCANPY: large-scale single-cell gene expression data analysis. *Genome Biology* **19**, 15 (2018).

164.Butler, A., Hoffman, P., Smibert, P., Papalexi, E. & Satija, R. Integrating single-cell transcriptomic data across different conditions, technologies, and species. *Nat Biotechnol* **36**, 411–420 (2018).

165.Love, M. I., Huber, W. & Anders, S. Moderated estimation of fold change and dispersion for RNA-seq data with DESeq2. *Genome Biology* **15**, 550 (2014).

Chapter 4

FUTURE DIRECTIONS AND CHALLENGES

SUMMARY

The autonomic nervous system (ANS) plays a pivotal role in regulating organ functions through descending brain-to-body signaling. Historically, the ANS was considered to mediate simple motor functions with limited neurochemical diversity. However, recent advances in neurotechnology have shown that brain-to-body communication is more complex and dynamic than previously appreciated. This chapter synthesizes current knowledge about the molecular and functional diversity of autonomic motor neurons. I present a comparative analysis of the cellular architecture of the ANS and the suggested roles of distinct neuron populations. Additionally, I explore the emerging view that the ANS interacts with diverse systems involving metabolism, immunology and ageing, which extends its role beyond simple brain-organ motor modulation. Finally, I emphasize the need for cell-type-specific and longitudinal studies of the ANS to uncover novel mechanisms underlying body-brain interactions and to identify new translational opportunities for therapeutic interventions.

Wang, T., et al. (2025). “Molecular and functional diversity of the autonomic nervous system”. In: *Nature Reviews Neuroscience* 26(10), pp. 607–622. doi: 10.1038/s41583-025-00941-2.

GENETICALLY DEFINED AUTONOMIC CIRCUITS

Foundational insights into autonomic functions were obtained by early studies in the 20th century mainly with histological and electrophysiological techniques. These approaches were analogous to the early stages of central nervous system research, where neurons were classified as excitatory and inhibitory neurons. The subsequent maturation of molecular and genetic tools allowed further defining different neuron classes[1–4].

In this section, I highlight distinct classes of autonomic motor neurons, their organ innervation patterns, and how these findings refine our understanding of autonomic architecture (**Fig. 1**). The growing availability of transcriptomic datasets offers an unprecedented opportunity to analyze the cellular organization of the ANS at a granular level. However, these datasets are often scattered across different resources and stored in inconsistent formats, making comparative analysis challenging. To address this issue, we have developed an online portal (available at ans-cell-atlas.com) for an integrated view of published datasets, facilitating easier access and comparison for researchers.

Sympathetic neuron types and pathways

Historically, sympathetic postganglionic neurons were characterized based on the expression of a limited set of neuropeptides and neurotransmitters, such as NPY and somatostatin (SST)[5–7]. However, these markers either failed to distinguish specific subpopulations or were observed only in limited species. Electrophysiological studies identified distinct firing patterns or presynaptic stimulation thresholds implying different functional groups exist in the same ganglion[8,9]. Similarly, sympathetic postganglionic neurons were classified based on different functions, such as vasoconstrictor, vasodilator, pilomotor, and secretomotor neurons[10,11]. Despite these broad categories, the prevailing view is that sympathetic postganglionic neurons are largely homogeneous in terms of neurotransmitter profiles and functionality.

Development of contemporary tools has challenged this notion and revealed substantial molecular and anatomical diversity among sympathetic postganglionic neurons. Multiple subpopulations have been identified within sympathetic ganglia, including the SCG[12–14], SG[15–18], and CG-SMG[18–20]. These subpopulations express unique combinations of neuropeptides, ion channels, and transcription factors, implying specialized functional roles. For example, one study combined retrograde labeling with single-cell RNA sequencing to identify a subset of heart-innervating neurons in the SG that express NPY[17]. On a separate research, oxytocin-expressing neurons serve as an endogenous regulator of white adipose tissue and metabolism[21]. More recent unbiased cellular atlases of sympathetic ganglia have identified two separate neuron populations in the CG-SMG projecting to the GI tract and secretory tissues, independently suppressing GI transit and bile secretion[19].

Another area that remains poorly understood is the neural connectivity between pre- and post-ganglionic neuron types[22,23]. One study revealed that two preganglionic neuron subsets, CARTPT+ and OXTR+, selectively target the CG-SMG and adrenal gland, respectively[24]. These results suggest parallel molecularly distinct preganglionic-postganglionic-organs projections. It would be interesting to investigate if the same principle applies to other organs.

Parasympathetic neuron types and pathways

Parasympathetic postganglionic neurons are located near or within their target organs, leading to distinct anatomical and developmental features compared to their sympathetic counterparts. While these neurons are broadly cholinergic, some cranial parasympathetic neurons also exhibit nitrergic properties[7]. The molecular diversity of parasympathetic postganglionic neurons across different organs warrants further investigation.

At the preganglionic level, early anatomical studies revealed that efferents from the DMV and NA are spatially organized according to target tissues[25,26]. For example, viscerotopic map was observed in the DMV in rodents[27]. Electrophysiological studies further showed

that organ-specific DMV neurons exhibit distinct morphological and biophysical properties, supporting functional specialization among parasympathetic preganglionic subpopulations[28]. In one example, cannabinoids were found to suppress both excitatory and inhibitory synaptic inputs onto stomach-projecting DMV neurons via presynaptic CB1 receptor[29].

Advanced molecular profiling expanded this veiw[30–34], by identifying diverse neuron types with distinct expression patterns of receptors, transmembrane proteins, and neuropeptides. Within the NA, several neuronal clusters have been identified, two of which project to the heart. Interestingly, these NA populations terminate on different cardiac cell types[35]. One of these neuron classes also projects the lungs, and mediates the dive reflex, a physiological response to submersion in water. Two other non-overlapping NA populations innervate the esophagus and larynx, respectively[33]. DMV neurons exhibit a similar logic: two distinct subtypes both innervate the stomach but synapse on different gastric enteric neuron types[31]. Functional manipulation studies in parasympathetic neurons were recently reviewed[30]. Together, these findings show that ANS harbors molecularly diverse neuron populations and pathways for functional specializations.

Although individual ANS relays and pathways have been characterized, emerging evidence points to more direct crosstalk between the parasympathetic and sympathetic systems[36–40]. One such example was observed where parasympathetic preganglionic or enteric neurons innervating sympathetic ganglia. Similarly, preganglionic neurons in the spinal cord and hindbrain integrate input from brain centers, peripheral sensory neurons, and local reflex arcs in ways that are not yet fully understood[41].

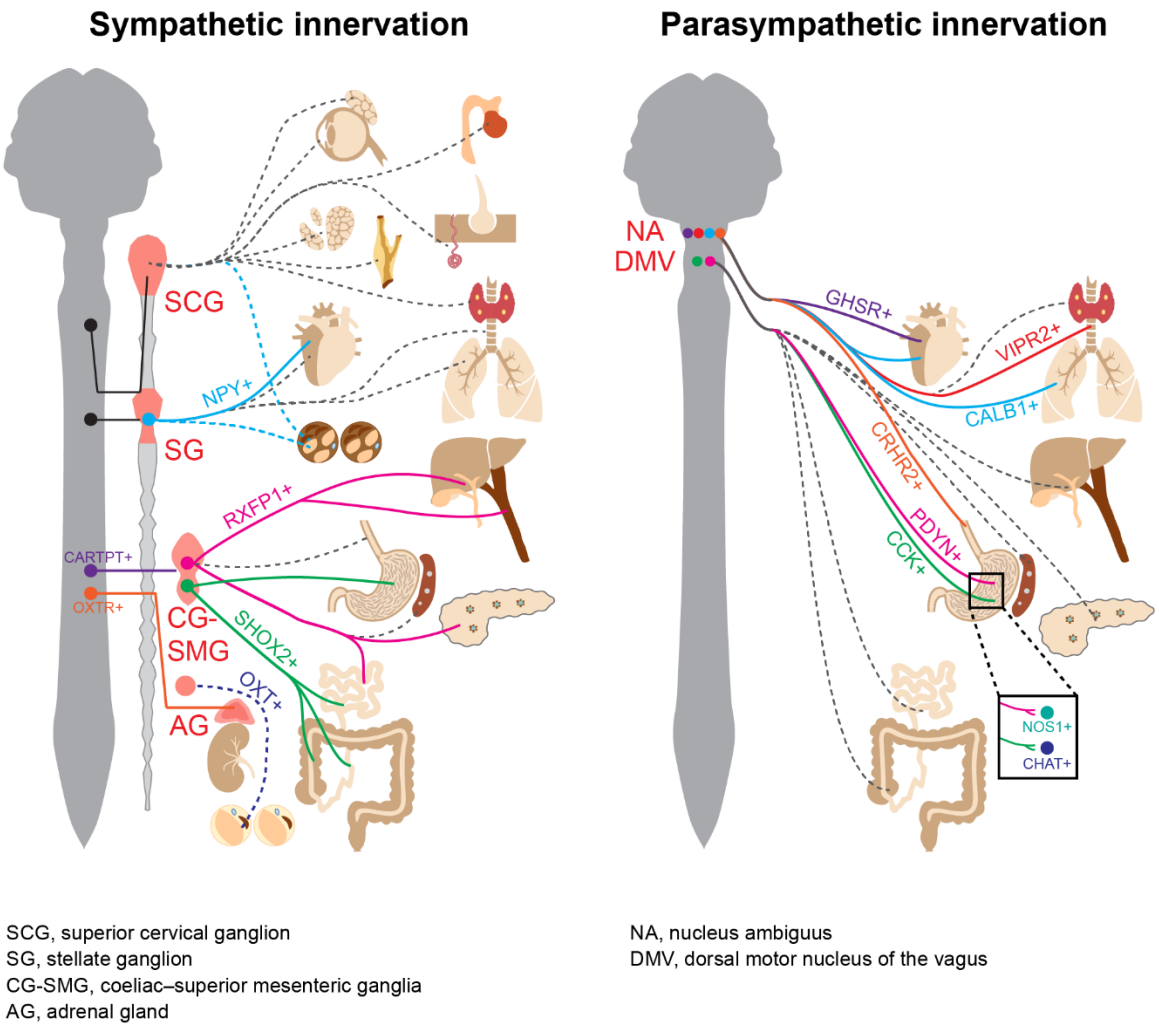

Fig. 1 Genetically defined autonomic innervation. Illustration depicting molecularly defined sympathetic (left) and parasympathetic (right) circuits. Distinct autonomic nervous system neuronal populations in the spinal cord and sympathetic ganglia are highlighted as colour-coded circles, along with their corresponding marker genes. In addition to well-established anatomical connections (dashed lines), genetic tracing in rodents has revealed unique organ- and tissue-specific innervation patterns (solid lines). Certain autonomic projections have been molecularly delineated in organs, but their connectivity to the ganglia remains to be confirmed (colour-coded dashed lines). ARG, aorticorenal ganglion; CG-SMG, coeliac-superior mesenteric ganglia; DMV, dorsal motor nucleus of the vagus; NAm, nucleus ambiguus; SCG, superior cervical ganglion; SG, stellate ganglion.

INTEGRATION OF AUTONOMIC CONTROL ACROSS ORGANS

In neural systems, functional diversity is orchestrated across multiple levels, ranging from the molecular identities and firing properties of individual neurons to their anatomical projections and the large-scale network interactions that drive complex physiological processes[42–47]. Emerging evidence suggests that the ANS also utilizes multi-layered mechanisms to precisely modulate signals for each target organ. In this section, I provide a systematic overview of how autonomic modulation is organized (**Fig. 2**).

Anatomical connection

While parasympathetic ganglia reside proximal to the target organs, sympathetic neurons are housed in paravertebral chains or prevertebral ganglia located near major arteries. Sympathetic postganglionic neurons send long projections to the target organ. A key dimension of diversity arises from the anatomical wiring (**Fig. 1a**). It was shown that each ganglion innervates multiple organs, and single organ receives inputs from several ganglia. For example, SCG projects to iris dilator muscles, lacrimal glands and salivary glands. Conversely, organs such as inguinal white adipose tissue (iWAT), lung, and heart are innervated by several chain ganglia along the spinal column[48–50].

Within a single autonomic ganglion or central nucleus, multiple neuron types are present, raising the question how individual populations are connected to distinct tissue or cell types (**Fig. 2, Neuron-cell projection**). Two conceptual models have been proposed on the autonomic wiring diagram. In the “one-to-all” model, all subpopulations within a ganglion or nucleus project indiscriminately to all tissues or cell types in a given organ, implying broad functional overlap[51]. In contrast, the “one-to-specific” model posits that distinct subpopulations preferentially connect to specific tissues or cell types[52,53]. Recent multi-color retrograde tracing data , at least in part, supported the one-to-specific model: distinct subsets of CG-SMG neurons innervate separate intestinal segments[19,54], while different SG neurons project either to the heart or iBAT[55]. Another study shows that NPY+ sympathetic nerve subset localizes primarily around blood vessels in both brown and white adipose

tissue, where NPY promotes mural cells proliferate into thermogenic adipocytes[56]. Similarly, two DMV neuron populations innervate distinct gastric enteric neuron classes[31]. These different anatomical routes underpin the nuanced and organ-specific capabilities of autonomic regulation.

These findings raise intriguing questions about organ-specific axonal targeting[57,58]. Integrating anatomical datasets with gene expression analyses of neuron-cell pairs may uncover local factors, such as axonal guidance molecules[59,60] and trophic signals[61], that shape the developing autonomic motor neurons, directing their migratory paths and terminal fates.

Stimulus-neuronal activity relationship

Sympathetic activity broadly correlate with adverse conditions such as stress, anxiety, obesity, and aging[62,63], whereas parasympathetic activity predominates under more relaxed states[64]. Direct observation of neuronal activity using electrophysiology and immediate early gene expression have confirmed that certain stimuli indeed activate autonomic motor neurons. Parasympathetic preganglionic neurons were stimulated by feeding or diving reflex[65,66], while the sympathetic system was linked to hunger and hypoxia[67,68]. CG-SMG neurons showed robust immediate early gene expression following acute cold exposure or chronic depletion of gut microbiota in mice[54,69]. Noradrenergic nerve fibers in the adipose tissue are modulated under low temperature[70], or long-term metabolic challenges such as high-fat-diet-induced obesity[56]. Despite the accumulating evidence, it remains unclear whether individual autonomic motor neurons are tuned to a specific or broad set of stimuli (**Fig. 2, Neuronal activity**). To address this bottleneck, real-time cellular resolution recording in awake animals will be required although it calls for significant technical innovations.

Neurotransmitter coding

Another factor of autonomic diversity stems from the neurochemical coding at synaptic signaling. While sympathetic postganglionic neurons primarily release norepinephrine as the neurotransmitter, they can also produce an array of neuromodulators such as GABA, serotonin, NPY, galanin, SST and substance P[8,71–73]. The different combinations of neuromodulator expression were reported in various sympathetic ganglia across species. Moreover, the levels of NPY expression in SG neurons subtypes correlate with different firing properties[17]. Parasympathetic preganglionic neurons mainly secret acetylcholine and may co-release vasoactive intestinal polypeptide (VIP) and nitric oxide (NO)[74]. Growing molecular analyses have identified additional secretory protein expression that may play a role in synaptic transmission (**Fig. 2, Synaptic signaling**). These non-adrenergic, non-cholinergic (NANC) transmitters are released onto target organs, contributing to functional diversity at the level of neurotransmission[74–77].

Postsynaptic tissues likewise express distinct sets of adrenergic and cholinergic receptors, yielding diverse responses to the same upstream autonomic input[78]. Different adrenergic receptor subtypes have preferential affinities for norepinephrine versus epinephrine, resulting in varying intracellular signaling cascades through specific G protein-coupled pathways[79]. Cholinergic receptors include both muscarinic receptors that function via G protein signaling and nicotinic receptors that act as ligand-gated ion channels[80]. Indeed, the human tissue RNA expression database indicates that various tissues display unique combinations of adrenergic and cholinergic receptors[81,82]. Consequently, identical sympathetic neuronal input may activate heart muscle cells through Gs-coupled adrenergic receptors, while inhibiting lymph node cells via Gi-coupled signaling. Similarly, parasympathetic signals slow heart rate even as they stimulate salivary gland secretion. Local tissue conditions, such as regional blood flow or proximity to nerve terminals, further influence the effective concentration of neurotransmitters.

These aspects of autonomic control are not static. Rather, they shift under different physiological states, adapt to pathological conditions, or become dysregulated, and change throughout the lifespan. For example, a heart attack retracts specific sympathetic

postganglionic axons and alters cardiac-projecting neurons[14,83], whereas chronic stress over-activates sympathetic pathways[84]. Such dynamic autonomic plasticity emphasizes the importance of longitudinal research at multiple time scales[85].

EXPANDING THE FUNCTIONAL ROLES OF AUTONOMIC NEURONS

Beyond its primary roles in organ-level motor control, the ANS interacts with many other biological systems including immune responses[86–88], metabolic balance[89,90], tissue regeneration[91–93], and disease progression[58,94–97]. For instance, brain-to-spleen sympathetic nerves were shown to suppress acute systemic inflammation via β2-adrenergic receptors[98,99]. The same signaling promotes the migration of hematopoietic stem and progenitor cells in the bone marrow[100,101]. In cancer therapy, blocking β1-adrenergic signals restores the activity of exhausted CD8+ T cells, boosting immunotherapeutic outcomes[102,103]. More recently, a study suggested that pro- and anti-inflammatory responses are mediated by separate ascending pathways[104], but the subsequently descending mechanisms remain unclear. Future work linking neuronal ensembles underlying this autonomic modulation of immunity will bridge the gaps in our understanding of autonomic control beyond the direct regulation of individual end organs.

There are potential functional links between autonomic signals and metabolism[90]. Sympathetic neuron–associated macrophages clear norepinephrine, preventing fat breakdown. Disrupting macrophage functions led to changes in sympathetic innervation and obesity susceptibility[105,106]. Within white visceral fat depot, ARG nerves stimulated nearby innate lymphoid cells through β2-adrenergic signaling, affecting both innate immunity and adipose functions[107]. These observations highlight a wide range of autonomic routes regulating metabolism, not simply by targeting organs like the liver and pancreas, but also through other organs or local cellular intermediaries.

Autonomic involvement in tissue repair and regeneration has recently been reported[108,109]. Acute stress caused hair greying in mice by stimulating melanocyte stem cells that express β2-adrenergic receptors, independently of immune signals or adrenal stress hormones[108]. Although the relevance of autonomic signaling in different research domains has been shown, the underlying neural substrates and circuits remain to be identified. The examples above represent only a glimpse of the complex and dynamic interactions between the ANS and other physiological systems. Future research will continue to uncover the breadth of these functional relationships.

Clinically, peripheral modulation of the ANS is already used to treat several conditions[110]. For example, surgical resection of the stellate ganglion or thoracic sympathetic chain is an established treatment for certain cardiac arrhythmias and is included in clinical guidelines[111,112]. Similarly, vagus nerve stimulation (VNS), which activates both afferent and efferent fibers, is approved for disorders such as epilepsy[113], cluster headaches[114], and migraines[115]. Expanding applications of VNS are being explored for heart failure[116], myocardial infarction[117], and other chronic diseases[97].

However, these interventions often affect broad populations of neurons, leading to unintended side effects. This highlights a major limitation of current neuromodulation therapies: they lack specificity for the particular autonomic pathways or cell types responsible for disease. To overcome this challenge, there is an urgent need to define the molecular and functional diversity within the ANS. As emphasized in this review, a deeper understanding of autonomic circuits will pave the way for next-generation therapies that precisely target disease-relevant neurons and minimize off-target effects.

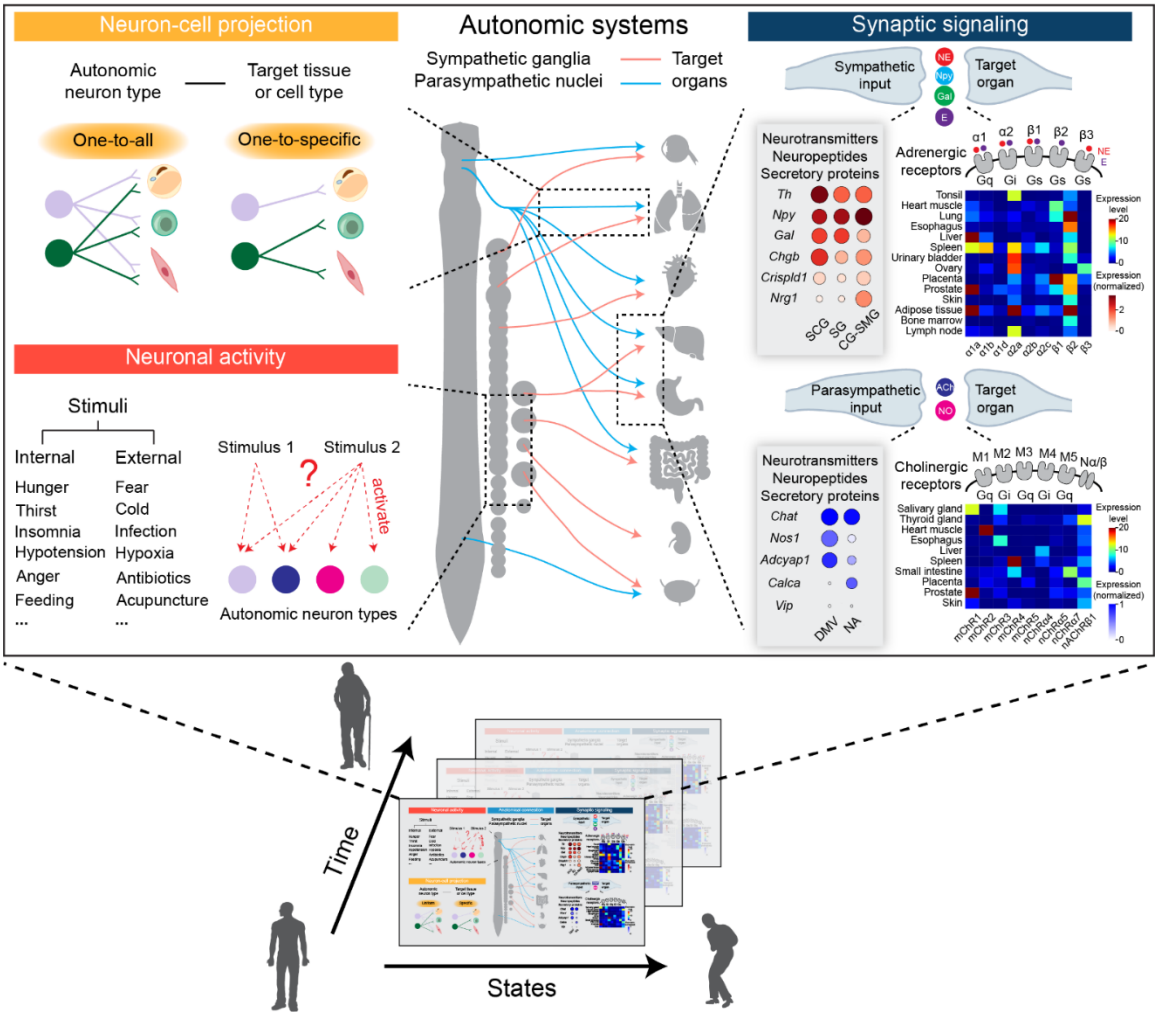

Fig. 2 Multidimensional autonomic regulation of organ functions. A conceptual overview illustrating how autonomic modulation operates at multiple layers, across synaptic signalling, neuronal activity, anatomical connections and physiological conditions. These interrelated processes adapt to varying physiological conditions and across time. Left: anatomical wiring links neuron populations to specific organs and tissue types, enabling dynamic and coordinated physiological control. Middle: neuronal activity patterns integrate sensory information, shaping the timing and amplitude of responses in target tissues. Right: at the synaptic level, diverse neurotransmitters and neuromodulators as well as receptors fine-tune signal transmission. Neurotransmitters and neuromodulators, including norepinephrine (NE), epinephrine (E), neuropeptide Y (NPY), galanin (Gal),

acetylcholine (ACh) and nitric oxide (NO), mediate chemical communication between neurons and target cells. The dot plots show gene expression of representative neurotransmitters and modulators across sympathetic ganglia and parasympathetic nuclei in mice, based on publicly available single-cell transcriptomics at Gene Expression Omnibus (GEO) database: superior cervical ganglion (SCG) (GSE175421), stellate ganglion (SG) (GSE231924), coeliac-superior mesenteric ganglia (CG-SMG) (GSE278457), dorsal motor nucleus of the vagus (DMV) (GSE172411) and nucleus ambiguus (NAm) (GSE198709, GSE202760 and GSE211538). The heat maps illustrate the diverse expression of selected neurotransmitter receptors across peripheral tissues in humans, based on transcriptomic data from the Human Protein Atlas at https://www.proteinatlas.org/humanproteome/tissue/data#hpa_tissues_rna.

CONCLUSIONS

In this review, I highlighted three major advances in our understanding of the ANS. First, recent studies have revealed substantial molecular and functional diversity of autonomic motor neurons at both preganglionic and postganglionic levels. This redefines autonomic pathways as highly specialized circuits that originate in the central nervous system, pass through diverse autonomic ganglia, and innervate distinct peripheral targets.

Second, I emphasize the extensive intra- and inter-system interactions of the ANS. While the sympathetic and parasympathetic divisions are often viewed as opposing forces, growing evidence shows that they frequently act in coordination, which needs to be embraced as a fundamental characteristic. In addition to the neuronal pathways, systemic factors such as sympathetic adrenal signals also modulate organ functions. The ANS interacts with broad regulatory systems in the body, adding further complexity.

Third, the ANS is a dynamic system that adapts to the physiological and pathological states. Autonomic circuits are flexibly recruited and modulated across time and context, yet the mechanisms underlying such plasticity remain poorly understood.

Together, these insights call for a shift in how we conceptualize and study the ANS—not as a set of fixed, antagonistic pathways, but as a diverse, integrated, and adaptable system.

EXPERIMENTAL MODELS AND METHOD DETAILS

Data availability

We developed an online portal (available at https://ans-cell-atlas.com/) for an integrated view of published single-cell transcriptomics at the GEO database. All source code is available via GitHub at https://github.com/YTwTJ/Molecular-and-Functional-Diversity-of-the-Autonomic-Nervous-System. In **Fig.** 3, dot plots are generated from GEO datasets: SCG (GSE175421), stellate ganglion (GSE231924), CG-SMG (GSE278457), DMV (GSE172411) and nucleus ambiguus (GSE198709, GSE202760 and GSE211538). In **Fig.** 3, heat maps plot transcriptomic data available via the Human Protein Atlas at https://www.proteinatlas.org/humanproteome/tissue/data#hpa_tissues_rna.

REFERENCES

1.Lein, E. S. *et al.* Genome-wide atlas of gene expression in the adult mouse brain. *Nature* **445**, 168–176 (2007).

2.Sternson, S. M., Atasoy, D., Betley, J. N., Henry, F. E. & Xu, S. An Emerging Technology Framework for the Neurobiology of Appetite. *Cell Metab* **23**, 234–253 (2016).

3.Luo, L., Callaway, E. M. & Svoboda, K. Genetic Dissection of Neural Circuits: A Decade of Progress. *Neuron* **98**, 256–281 (2018).

4.Zeng, H. What is a cell type and how to define it? *Cell* **185**, 2739–2755 (2022).

5.Miolan, J. P. & Niel, J. P. The mammalian sympathetic prevertebral ganglia: integrative properties and role in the nervous control of digestive tract motility. *J Auton Nerv Syst* **58**, 125–138 (1996).

6.Kaestner, C. L., Smith, E. H., Peirce, S. G. & Hoover, D. B. Immunohistochemical analysis of the mouse celiac ganglion: An integrative relay station of the peripheral nervous system. *J Comp Neurol* **527**, 2742–2760 (2019).

7.Ernsberger, U., Deller, T. & Rohrer, H. The diversity of neuronal phenotypes in rodent and human autonomic ganglia. *Cell Tissue Res* **382**, 201–231 (2020).

8.Jobling, P. & Gibbins, I. L. Electrophysiological and morphological diversity of mouse sympathetic neurons. *J Neurophysiol* **82**, 2747–2764 (1999).

9.Li, C. & Horn, J. P. Physiological classification of sympathetic neurons in the rat superior cervical ganglion. *J Neurophysiol* **95**, 187–195 (2006).

10.Jänig, W. & McLachlan, E. M. Characteristics of function-specific pathways in the sympathetic nervous system. *Trends Neurosci* **15**, 475–481 (1992).

11.Gibbins, I. L. Vasoconstrictor, vasodilator and pilomotor pathways in sympathetic ganglia of guinea-pigs. *Neuroscience* **47**, 657–672 (1992).

12.Aubert, M. *et al.* Gene editing and elimination of latent herpes simplex virus in vivo. *Nat Commun* **11**, 4148 (2020).

13.Mapps, A. A. *et al.* Diversity of satellite glia in sympathetic and sensory ganglia. *Cell Rep* **38**, 110328 (2022).

14.Ziegler, K. A. *et al.* Immune-mediated denervation of the pineal gland underlies sleep disturbance in cardiac disease. *Science* **381**, 285–290 (2023).

15.van Weperen, V. Y. H. *et al.* Single-cell transcriptomic profiling of satellite glial cells in stellate ganglia reveals developmental and functional axial dynamics. *Glia* **69**, 1281–1291 (2021).

16.Davis, H., Paterson, D. J. & Herring, N. Post-Ganglionic Sympathetic Neurons can Directly Sense Raised Extracellular Na+ via SCN7a/Nax. *Front Physiol* **13**, 931094 (2022).

17.Sharma, S. *et al.* Tiered sympathetic control of cardiac function revealed by viral tracing and single cell transcriptome profiling. *Elife* **12**, e86295 (2023).

18.Sivori, M. *et al.* The pelvic organs receive no parasympathetic innervation. *Elife* **12**, RP91576 (2024).

19.Wang, T., Teng, B., Yao, D. R., Gao, W. & Oka, Y. Organ-specific sympathetic innervation defines visceral functions. *Nature* **637**, 895–902 (2025).

20.Kanda, H., Yamanaka, H., Dai, Y. & Noguchi, K. The neuronal and glial cell diversity in the celiac ganglion revealed by single-nucleus RNA sequencing. *Sci Rep* **15**, 5510 (2025).

21.Li, E. *et al.* Control of lipolysis by a population of oxytocinergic sympathetic neurons. *Nature* **625**, 175–180 (2024).

22.Beaudet, M. M., Braas, K. M. & May, V. Pituitary adenylate cyclase activating polypeptide (PACAP) expression in sympathetic preganglionic projection neurons to the superior cervical ganglion. *J Neurobiol* **36**, 325–336 (1998).

23.Deuchars, S. A. & Lall, V. K. Sympathetic preganglionic neurons: properties and inputs. *Compr Physiol* **5**, 829–869 (2015).

24.Harima, Y. *et al.* Parallel labeled-line organization of sympathetic outflow for selective organ regulation in mice. *Nat Commun* **15**, 10478 (2024).

25.Fox, E. A. & Powley, T. L. Longitudinal columnar organization within the dorsal motor nucleus represents separate branches of the abdominal vagus. *Brain Res* **341**, 269–282 (1985).

26.Bieger, D. & Hopkins, D. A. Viscerotopic representation of the upper alimentary tract in the medulla oblongata in the rat: the nucleus ambiguus. *J Comp Neurol* **262**, 546–562 (1987).

27.Berthoud, H. R., Carlson, N. R. & Powley, T. L. Topography of efferent vagal innervation of the rat gastrointestinal tract. *Am J Physiol* **260**, R200-207 (1991).

28.Zsombok, A., Bhaskaran, M. D., Gao, H., Derbenev, A. V. & Smith, B. N. Functional plasticity of central TRPV1 receptors in brainstem dorsal vagal complex circuits of streptozotocin-treated hyperglycemic mice. *J Neurosci* **31**, 14024–14031 (2011).

29.Derbenev, A. V., Stuart, T. C. & Smith, B. N. Cannabinoids suppress synaptic input to neurones of the rat dorsal motor nucleus of the vagus nerve. *J Physiol* **559**, 923–938 (2004).

30.Coverdell, T. C., Abbott, S. B. G. & Campbell, J. N. Molecular cell types as functional units of the efferent vagus nerve. *Seminars in Cell & Developmental Biology* **156**, 210–218 (2024).

31.Tao, J. *et al.* Highly selective brain-to-gut communication via genetically defined vagus neurons. *Neuron* **109**, 2106-2115.e4 (2021).

32.Hornung, E. *et al.* Neuromodulatory co-expression in cardiac vagal motor neurons of the dorsal motor nucleus of the vagus. *iScience* **27**, 110549 (2024).

33.Coverdell, T. C., Abraham-Fan, R.-J., Wu, C., Abbott, S. B. G. & Campbell, J. N. Genetic encoding of an esophageal motor circuit. *Cell Rep* **39**, 110962 (2022).

34.Su, Y. *et al.* Brainstem Dbh+ neurons control allergen-induced airway hyperreactivity. *Nature* **631**, 601–609 (2024).

35.Veerakumar, A., Yung, A. R., Liu, Y. & Krasnow, M. A. Molecularly defined circuits for cardiovascular and cardiopulmonary control. *Nature* **606**, 739–746 (2022).

36.Hibberd, T. J., Zagorodnyuk, V. P., Spencer, N. J. & Brookes, S. J. H. Identification and mechanosensitivity of viscerofugal neurons. *Neuroscience* **225**, 118–129 (2012).

37.DePuy, S. D. *et al.* Glutamatergic neurotransmission between the C1 neurons and the parasympathetic preganglionic neurons of the dorsal motor nucleus of the vagus. *J Neurosci* **33**, 1486–1497 (2013).

38.Kressel, A. M. *et al.* Identification of a brainstem locus that inhibits tumor necrosis factor. *Proc Natl Acad Sci U S A* **117**, 29803–29810 (2020).

39.Muller, P. A. *et al.* Microbiota-modulated CART+ enteric neurons autonomously regulate blood glucose. *Science* **370**, 314–321 (2020).

40.Zhang, T., Perkins, M. H., Chang, H., Han, W. & de Araujo, I. E. An inter-organ neural circuit for appetite suppression. *Cell* **185**, 2478-2494.e28 (2022).

41.Sammons, M. *et al.* Brain-body physiology: Local, reflex, and central communication. *Cell* **187**, 5877–5890 (2024).

42.Bullmore, E. & Sporns, O. Complex brain networks: graph theoretical analysis of structural and functional systems. *Nat Rev Neurosci* **10**, 186–198 (2009).

43.Turrigiano, G. Homeostatic synaptic plasticity: local and global mechanisms for stabilizing neuronal function. *Cold Spring Harb Perspect Biol* **4**, a005736 (2012).

44.Bargmann, C. I. & Marder, E. From the connectome to brain function. *Nat Methods* **10**, 483–490 (2013).

45.LeCun, Y., Bengio, Y. & Hinton, G. Deep learning. *Nature* **521**, 436–444 (2015).

46.Luo, L. Architectures of neuronal circuits. *Science* **373**, eabg7285 (2021).

47.Zsombok, A., Desmoulins, L. D. & Derbenev, A. V. Sympathetic circuits regulating hepatic glucose metabolism: where we stand. *Physiol Rev* **104**, 85–101 (2024).

48.Kummer, W., Fischer, A., Kurkowski, R. & Heym, C. The sensory and sympathetic innervation of guinea-pig lung and trachea as studied by retrograde neuronal tracing and double-labelling immunohistochemistry. *Neuroscience* **49**, 715–737 (1992).

49.Huesing, C. *et al.* Sympathetic innervation of inguinal white adipose tissue in the mouse. *J Comp Neurol* **529**, 1465–1485 (2021).

50.Tomney, P. A., Hopkins, D. A. & Armour, J. A. Axonal branching of canine sympathetic postganglionic cardiopulmonary neurons. A retrograde fluorescent labeling study. *Brain Res Bull* **14**, 443–452 (1985).

51.Seals, D. R. & Victor, R. G. Regulation of muscle sympathetic nerve activity during exercise in humans. *Exerc Sport Sci Rev* **19**, 313–349 (1991).

52.DiBona, G. F. Neural control of the kidney: functionally specific renal sympathetic nerve fibers. *Am J Physiol Regul Integr Comp Physiol* **279**, R1517-1524 (2000).

53.Morrison, S. F. Differential control of sympathetic outflow. *American Journal of Physiology-Regulatory, Integrative and Comparative Physiology* **281**, R683–R698 (2001).

54.Muller, P. A. *et al.* Microbiota modulate sympathetic neurons via a gut-brain circuit. *Nature* **583**, 441–446 (2020).

55.Barrett, M. S., Hegarty, D. M., Habecker, B. A. & Aicher, S. A. Distinct morphology of cardiac- and brown adipose tissue-projecting neurons in the stellate ganglia of mice. *Physiol Rep* **10**, e15334 (2022).

56.Zhu, Y. *et al.* Sympathetic neuropeptide Y protects from obesity by sustaining thermogenic fat. *Nature* **634**, 243–250 (2024).

57.Asmus, S. E., Parsons, S. & Landis, S. C. Developmental changes in the transmitter properties of sympathetic neurons that innervate the periosteum. *J Neurosci* **20**, 1495–1504 (2000).

58.Scott-Solomon, E., Boehm, E. & Kuruvilla, R. The sympathetic nervous system in development and disease. *Nat Rev Neurosci* **22**, 685–702 (2021).

59.Carmeliet, P. & Tessier-Lavigne, M. Common mechanisms of nerve and blood vessel wiring. *Nature* **436**, 193–200 (2005).

60.Gallarda, B. W. *et al.* Segregation of axial motor and sensory pathways via heterotypic trans-axonal signaling. *Science* **320**, 233–236 (2008).

61.Enomoto, H., Heuckeroth, R. O., Golden, J. P., Johnson, E. M. & Milbrandt, J. Development of cranial parasympathetic ganglia requires sequential actions of GDNF and neurturin. *Development* **127**, 4877–4889 (2000).

62.Ekman, P., Levenson, R. W. & Friesen, W. V. Autonomic nervous system activity distinguishes among emotions. *Science* **221**, 1208–1210 (1983).

63.Ju, S. H., Yun, H., Oh, Y., Choi, Y. & Sohn, J.-W. Melanocortin-4 receptors activate sympathetic preganglionic neurons and elevate blood pressure via TRPV1. *Cell Rep* **41**, 111579 (2022).

64.Steffens, A. B., Van der Gugten, J., Godeke, J., Luiten, P. G. & Strubbe, J. H. Meal-induced increases in parasympathetic and sympathetic activity elicit simultaneous rises in plasma insulin and free fatty acids. *Physiol Behav* **37**, 119–122 (1986).

65.Panneton, W. M., Anch, A. M., Panneton, W. M. & Gan, Q. Parasympathetic preganglionic cardiac motoneurons labeled after voluntary diving. *Front Physiol* **5**, 8 (2014).

66.Chen, H. *et al.* Postprandial parasympathetic signals promote lung type 2 immunity. *Neuron* S0896-6273(24)00919-X (2025) doi:10.1016/j.neuron.2024.12.020.

67.Gonsalvez, D. G., Kerman, I. A., McAllen, R. M. & Anderson, C. R. Chemical Coding for Cardiovascular Sympathetic Preganglionic Neurons in Rats. *J Neurosci* **30**, 11781–11791 (2010).

68.Wang, M., Wang, Q. & Whim, M. D. Fasting induces a form of autonomic synaptic plasticity that prevents hypoglycemia. *Proc Natl Acad Sci U S A* **113**, E3029–E3038 (2016).

69.Jiang, H., Ding, X., Cao, Y., Wang, H. & Zeng, W. Dense Intra-adipose Sympathetic Arborizations Are Essential for Cold-Induced Beiging of Mouse White Adipose Tissue. *Cell Metab* **26**, 686-692.e3 (2017).

70.Murano, I., Barbatelli, G., Giordano, A. & Cinti, S. Noradrenergic parenchymal nerve fiber branching after cold acclimatisation correlates with brown adipocyte density in mouse adipose organ. *J Anat* **214**, 171–178 (2009).

71.Landry, M., Holmberg, K., Zhang, X. & Hökfelt, T. Effect of axotomy on expression of NPY, galanin, and NPY Y1 and Y2 receptors in dorsal root ganglia and the superior cervical ganglion studied with double-labeling in situ hybridization and immunohistochemistry. *Exp Neurol* **162**, 361–384 (2000).

72.Tyrrell, S. & Landis, S. C. The appearance of NPY and VIP in sympathetic neuroblasts and subsequent alterations in their expression. *J Neurosci* **14**, 4529–4547 (1994).

73.Wojtkiewicz, J. *et al.* Immunohistochemical characterization of superior cervical ganglion neurons supplying porcine parotid salivary gland. *Neurosci Lett* **500**, 57–62 (2011).

74.Kobori, N., Moore, A. N., Redell, J. B. & Dash, P. K. Caudal DMN neurons innervate the spleen and release CART peptide to regulate neuroimmune function. *J Neuroinflammation* **20**, 158 (2023).

75.Hökfelt, T. *et al.* Coexistence of peptides with classical neurotransmitters. *Experientia* **43**, 768–780 (1987).

76.Sann, H. & Pierau, F. K. Efferent functions of C-fiber nociceptors. *Z Rheumatol* **57 Suppl 2**, 8–13 (1998).

77.Andersson, K.-E. & Arner, A. Urinary bladder contraction and relaxation: physiology and pathophysiology. *Physiol Rev* **84**, 935–986 (2004).

78.Ernsberger, U., Deller, T. & Rohrer, H. The sympathies of the body: functional organization and neuronal differentiation in the peripheral sympathetic nervous system. *Cell Tissue Res* **386**, 455–475 (2021).

79.Strosberg, A. D. Structure, function, and regulation of adrenergic receptors. *Protein Sci* **2**, 1198–1209 (1993).

80.Carlson, A. B. & Kraus, G. P. Physiology, Cholinergic Receptors. in *StatPearls* (StatPearls Publishing, Treasure Island (FL), 2025).

81.Uhlén, M. *et al.* Proteomics. Tissue-based map of the human proteome. *Science* **347**, 1260419 (2015).

82.Karlsson, M. *et al.* A single-cell type transcriptomics map of human tissues. *Sci Adv* **7**, eabh2169 (2021).

83.Barrett, M. S. *et al.* Ischemia-reperfusion myocardial infarction induces remodeling of left cardiac-projecting stellate ganglia neurons. *Am J Physiol Heart Circ Physiol* **326**, H166–H179 (2024).

84.McEwen, B. S. Physiology and neurobiology of stress and adaptation: central role of the brain. *Physiol Rev* **87**, 873–904 (2007).

85.de La Cruz, L., Bui, D., Moreno, C. M. & Vivas, O. Sympathetic motor neuron dysfunction is a missing link in age-associated sympathetic overactivity. *Elife* **12**, RP91663 (2024).

86.Pongratz, G. & Straub, R. H. The sympathetic nervous response in inflammation. *Arthritis Res Ther* **16**, 504 (2014).

87.Udit, S., Blake, K. & Chiu, I. M. Somatosensory and autonomic neuronal regulation of the immune response. *Nat Rev Neurosci* **23**, 157–171 (2022).

88.Chan, K. L., Poller, W. C., Swirski, F. K. & Russo, S. J. Central regulation of stress-evoked peripheral immune responses. *Nat Rev Neurosci* **24**, 591–604 (2023).

89.Berthoud, H.-R. & Neuhuber, W. L. Vagal mechanisms as neuromodulatory targets for the treatment of metabolic disease. *Ann N Y Acad Sci* **1454**, 42–55 (2019).

90.Martinez-Sanchez, N. *et al.* The sympathetic nervous system in the 21st century: Neuroimmune interactions in metabolic homeostasis and obesity. *Neuron* **110**, 3597–3626 (2022).

91.Klein Wolterink, R. G. J., Wu, G. S., Chiu, I. M. & Veiga-Fernandes, H. Neuroimmune Interactions in Peripheral Organs. *Annu Rev Neurosci* **45**, 339–360 (2022).

92.Ren, W., Hua, M., Cao, F. & Zeng, W. The Sympathetic-Immune Milieu in Metabolic Health and Diseases: Insights from Pancreas, Liver, Intestine, and Adipose Tissues. *Adv Sci (Weinh)* **11**, e2306128 (2024).

93.Zhang, B. & Chen, T. Local and systemic mechanisms that control the hair follicle stem cell niche. *Nat Rev Mol Cell Biol* **25**, 87–100 (2024).

94.Hodes, G. E., Kana, V., Menard, C., Merad, M. & Russo, S. J. Neuroimmune mechanisms of depression. *Nat Neurosci* **18**, 1386–1393 (2015).

95.Hanoun, M., Maryanovich, M., Arnal-Estapé, A. & Frenette, P. S. Neural regulation of hematopoiesis, inflammation, and cancer. *Neuron* **86**, 360–373 (2015).

96.Payne, S. C., Furness, J. B. & Stebbing, M. J. Bioelectric neuromodulation for gastrointestinal disorders: effectiveness and mechanisms. *Nat Rev Gastroenterol Hepatol* **16**, 89–105 (2019).

97.Mather, M. Autonomic dysfunction in neurodegenerative disease. *Nat. Rev. Neurosci.* **26**, 276–292 (2025).

98.Martelli, D., Yao, S. T., McKinley, M. J. & McAllen, R. M. Reflex control of inflammation by sympathetic nerves, not the vagus. *J Physiol* **592**, 1677–1686 (2014).

99.Ding, X. *et al.* Panicle-Shaped Sympathetic Architecture in the Spleen Parenchyma Modulates Antibacterial Innate Immunity. *Cell Rep* **27**, 3799-3807.e3 (2019).

100.Katayama, Y. *et al.* Signals from the sympathetic nervous system regulate hematopoietic stem cell egress from bone marrow. *Cell* **124**, 407–421 (2006).

101.Morrison, S. J. & Scadden, D. T. The bone marrow niche for haematopoietic stem cells. *Nature* **505**, 327–334 (2014).

102.Globig, A.-M. *et al.* The β1-adrenergic receptor links sympathetic nerves to T cell exhaustion. *Nature* **622**, 383–392 (2023).

103.Yaniv, D., Mattson, B., Talbot, S., Gleber-Netto, F. O. & Amit, M. Targeting the peripheral neural-tumour microenvironment for cancer therapy. *Nat Rev Drug Discov* **23**, 780–796 (2024).

104.Jin, H., Li, M., Jeong, E., Castro-Martinez, F. & Zuker, C. S. A body-brain circuit that regulates body inflammatory responses. *Nature* **630**, 695–703 (2024).

105.Pirzgalska, R. M. *et al.* Sympathetic neuron-associated macrophages contribute to obesity by importing and metabolizing norepinephrine. *Nat Med* **23**, 1309–1318 (2017).

106.Wolf, Y. *et al.* Brown-adipose-tissue macrophages control tissue innervation and homeostatic energy expenditure. *Nat Immunol* **18**, 665–674 (2017).

107.Cardoso, F. *et al.* Neuro-mesenchymal units control ILC2 and obesity via a brain-adipose circuit. *Nature* **597**, 410–414 (2021).

108.Zhang, B. *et al.* Hyperactivation of sympathetic nerves drives depletion of melanocyte stem cells. *Nature* **577**, 676–681 (2020).

109.Zhou, Y. *et al.* A brain-to-liver signal mediates the inhibition of liver regeneration under chronic stress in mice. *Nat Commun* **15**, 10361 (2024).

110.Shivkumar, K. *et al.* Clinical neurocardiology defining the value of neuroscience-based cardiovascular therapeutics. *J Physiol* **594**, 3911–3954 (2016).

111.Ajijola, O. A. *et al.* Bilateral cardiac sympathetic denervation for the management of electrical storm. *J Am Coll Cardiol* **59**, 91–92 (2012).

112.Al-Khatib, S. M. *et al.* 2017 AHA/ACC/HRS guideline for management of patients with ventricular arrhythmias and the prevention of sudden cardiac death: Executive summary: A Report of the American College of Cardiology/American Heart Association Task Force on Clinical Practice Guidelines and the Heart Rhythm Society. *Heart Rhythm* **15**, e190–e252 (2018).

113.Ben-Menachem, E. Vagus-nerve stimulation for the treatment of epilepsy. *Lancet Neurol* **1**, 477–482 (2002).

114.Mauskop, A. Vagus nerve stimulation relieves chronic refractory migraine and cluster headaches. *Cephalalgia* **25**, 82–86 (2005).

115.Turk, D. C. *et al.* Core outcome domains for chronic pain clinical trials: IMMPACT recommendations. *Pain* **106**, 337–345 (2003).

116.Premchand, R. K. *et al.* Autonomic regulation therapy via left or right cervical vagus nerve stimulation in patients with chronic heart failure: results of the ANTHEM-HF trial. *J Card Fail* **20**, 808–816 (2014).

117.Hadaya, J. *et al.* Vagal Nerve Stimulation Reduces Ventricular Arrhythmias and Mitigates Adverse Neural Cardiac Remodeling Post-Myocardial Infarction. *JACC Basic Transl Sci* **8**, 1100–1118 (2023).

EPILOGUE

In this thesis, I examine neural mechanisms that underlie physiological adjustments across the body, with particular emphasis on defining what autonomic neurons modulate. A key next step for the field is to determine how autonomic control is implemented within real-time physiological contexts. Scientific progress and technological innovation have always advanced hand in hand, as exemplified by research on the central nervous system. In the emerging field of brain-body axis, many unanswered questions require the development of new technologies. In particular, *in vivo* recording from peripheral autonomic neurons and real-time monitoring of organ physiology are in dire need.

The cellular and circuit architecture of autonomic systems introduces additional complexity. Individual ganglia contain multiple neuron populations with distinct molecular identities and connectivity patterns. Organs receive convergent inputs from diverse neural sources. The ultimate physiological outcome depends on how signals are integrated within peripheral networks. Understanding these interactions represents an important future direction, extending focused circuit dissection toward the study of dynamic neural network function in the periphery, analogous to advances achieved in central neural systems.

In closing, I would like to summarize several conceptual principles that are showcased by the work presented in this thesis.

Principle 1: Internal states are detected through specialized sensory channels.

Monitoring the internal environment requires neural access to variables that are distributed across the body and evolve over time. The nervous system achieves this through dedicated sensory interfaces, including central structures that directly sample circulating signals and peripheral afferent pathways that detect organ-specific conditions. These parallel channels allow specificity in discriminating internal deviations.

Principle 2: Autonomic pathways exhibit modular organization.

Communication from the brain to peripheral organs is mediated by anatomically and molecularly distinct autonomic circuits that can be independently engaged. Such organization enables selective adjustments of physiological processes across organs.

Principle 3: Physiological regulation emerges from dynamic integration of sensory and autonomic networks.

Effective control arises from continuous integration of sensory and descending signals. The brain-body communication is a dynamic process that stabilizes physiological variables while allowing adaptive flexibility.

Principle 4: Cellular- and circuit-level specificity provides new translational targets.

Linking defined neural populations to organ functions enables mechanistic interpretation of how dysregulation leads to pathological conditions. By moving from broad system descriptions to cell-type-resolved mechanisms, it becomes feasible to identify how perturbations in specific pathways alter bodily function and to develop more targeted approaches for intervention.